Department of Computing

Variational Image Segmentation with Constraints

Huizhu Pan

This thesis is presented for the Degree of
Master of Philosophy
of
Curtin University

February 2020

Declaration

I hereby declare that, to the best of my knowledge and belief this thesis contains no material previously published by any other person except where due acknowledgment has been made.

This thesis contains no material which has been accepted for the award of any other degree or diploma in any university.

I have obtained permission from the copyright owners to use any third-party copyright material reproduced in the thesis, or to use any of my own published work in which the copyright is held by another party.

Signature: _____

Date: _____

Abstract

Image segmentation is the task of partitioning images into meaningful sub-regions. It is a fundamental problem in image processing and integral part of higher-level computer vision problems such as object detection and recognition, target tracking, 3D reconstruction, etc. Variational models have been widely applied to the segmentation problem due to their effectiveness, versatility, and solid foundation in mathematics. In a variational model, the problem is framed as an energy functional whose minimization yields the solution. Many variational models using different image features have been designed, such as the edge-based snakes model, the geodesic active contour model, the region-based Mumford-Shah model, and the Chan-Vese model, etc. Though variational models have seen much success in solving segmentation problems based on the extracted image features, the image features alone do not always suffice, such as in the case of object adhesion, occlusion, missing information in the image, etc. In these cases, prior knowledge is necessary to assist with segmentation. The works of this thesis focus on novel variational level set models with prior constraints and the efficient design of their numerical solutions.

When crucial information is missing from the image, it is necessary to introduce prior knowledge. Landmarks are useful tools that can guide the segmentation contour towards given locations. They can be obtained through manual placement or automatic detection, dependant on the applications. Aside from serving as guidance, they can also facilitate the inpainting of illusory contours. The first work in this thesis proposes a new variational image segmentation model where the contour crosses some pre-defined landmarks. It builds on the Chan-Vese model by adding a new landmarks-based constraint term. The resulting optimization problem can be efficiently solved through the split-Bregman method. Experimental results show that the Chan-Vese model with landmarks (CVL) can not only increase the robustness but also improve the accuracy of segmentation.

On the other hand, it is relatively difficult to create large sections of the contour with the CVL since the model favors shorter contours. The second work proposes the

Chan-Vese model with landmark constraints and elastica (CVLE) that specializes in the interpolation of longer contours with fewer landmarks. The new model is solved with the split-Bregman method, and experimental results show that the CVLE works well for generating illusory contours in large regions with landmarks while maintaining the segmentation details.

In applications such as cell image segmentation, the subjects often appear similar and adhere to each other. Therefore, they are difficult to separate with either edge-based or region-based variational models and should require additional constraints. One useful constraint is topology preservation, where if topology of the subject is known a priori, it remains invariant throughout segmentation. The self-repelling snakes (SR) model achieves this by making the segmentation contours repel to prevent merging and splitting. The original solution is based on additive operator splitting which has a high memory requirement. The third work of this thesis proposes an alternate solution to the SR model with the split-Bregman method and a differently smoothed label function that increases the stability of contour evolution. Applications of the new algorithm to cell image segmentation and MRI imagery segmentation demonstrate its effectiveness.

In summary, this thesis contains three new works relating to variational level set models for image segmentation with constraints. The first is the design of the Chan-Vese model with landmarks along with its solution via the split-Bregman method. Next, the Chan-Vese model with elastica and landmarks is proposed for inpainting long illusory contours, and its solution is devised via the split-Bregman method as well. Finally, a memory-efficient solution with a stable label function formulation is proposed for the self-repelling snakes model which preserves topology.

Acknowledgments

These past two years have been a memorable and life-changing journey for me. I will forever be indebted to my supervisors, Prof. Wan-quan Liu and Prof. Ling Li, for their patient guidance and unending support. I also wish to thank my father, Prof. Zhenkuan Pan, who introduced me to this field of research and offered much invaluable advice. Special thanks also goes to Prof. Guanglu Zhou at Curtin University for his insights in mathematics and help with my publications, Dr. C. Le Guyader at the Université de Rouen for sharing her knowledge and source code, and my colleagues at Curtin University and at Qingdao University for all their help and encouragements. I am very fortunate to be working alongside intellectual and motivated people in an office filled with joy and laughter.

Finally, these days would not have been the same without my dearest Brad.

Contents

1 Introduction **16**

1.1 Image segmentation 16

1.2 Variational models in image segmentation 20

1.3 Current challenges 23

1.3.1 Landmark priors 24

1.3.2 Topological priors 25

1.4 Research objectives 26

1.5 Structure of thesis and summary of contributions 26

2 Variational Image Segmentation Models **29**

2.1 Variational methods 29

2.2 Gradient descent equations 30

2.3 The level set method 31

2.4 Variational models 34

2.4.1 Edge-based models 34

2.4.2 Region-based models 37

2.5 The numerical methods 38

2.5.1 Discretization 38

2.5.2 The split-Bregman algorithm 41

2.6 Summary 44

3 The Extended Chan-Vese Model with Landmark Constraints **45**

3.1 The Chan-Vese model 46

3.2 The split-Bregman algorithm for the Chan-Vese model 48
3.3 The Chan-Vese model with landmark constraints 51
3.4 The split-Bregman algorithm for the Chan-Vese model with landmark constraints 53
3.5 Experimental results 56
3.6 Summary 62

4 The Extended Chan-Vese Model with Landmark Constraints and Elastica 63
4.1 The Chan-Vese model with elastica 64
4.2 The Chan-Vese model with landmark constraints and elastica 66
4.3 The split-Bregman algorithm for the Chan-Vese model with landmark constraints and elastica 66
4.4 Experimental results 73
4.5 Summary 78

5 The Self-repelling Snakes Model for Topology Preservation 81
5.1 The self-repelling snakes model 83
5.2 The split-Bregman algorithm for the self-repelling snakes model . . . 87
5.3 Experimental results 92
5.4 Summary 97

6 Conclusions and Future Works 98
6.1 Conclusions 98
6.2 Future works 101

List of Figures

1-1 Classical methods for image segmentation. (a) the original image, (b) image segmented with the Canny filter [1], (c) Gaussian-blurred image ($\sigma = 3.2$) segmented with the Canny filter, (d) image segmented with Otsu's thresholding method [2], (e) the previous result post-processed with morphological operations, (f) separation of the foreground instances with the watershed method [3]. 18

1-2 Variational image segmentation based on (a) the piecewise constant assumption, (b) edges and topology preservation, (c) gradient vector flow, (d) color and texture, (e) shape priors, (f) optical flow. Results (a)(c)(d)(e)(f) are taken from [4, 5, 6, 7] 21

1-3 Two circles segmented by the repulsive snakes model [8] and the GAC model [9], (a) initialization of the contour in red, (b) the contour with preserved topology, (d) the contour with altered topology. 25

2-1 The function $\phi(x)$ over a 2D image domain for the two phase segmentation problem. $\phi(x) > 0$ denotes the object, $\phi(x) < 0$ denotes the background, and $\phi(x) = 0$ marks the segmentation contour in red. The top-down view shows how the contour changes topology (splits) as it evolves. 32

3-1 Synthetic image of scissors. (a-c) and (d-f) use two different initial contours. (c, f) each uses one landmark while (b, e) do not use landmarks. The second initial contour led to under-segmentation shown in (e), which was fixed by a landmark as shown in (f). In both experiments, $\alpha_1 = 1$, $\alpha_2 = 1$, $\gamma = 1$, $\varepsilon = 3$, $\theta = 20$, $t = .1$, $Tol = 10^{-6}$. In (c, f), $\mu = 5$. 57

3-2 Synthetic image of scissors, close-up. (a-d) show the evolution of the segmentation contour in the first 25 iterations, in chronological order. 58

3-3 An image of a wrench with synthetic salt and pepper noise. (a-c) show segmentation without landmarks, (d-f) show segmentation via CVL with four landmarks, and (c, f) are close-ups of the critical region. In both rows, $\alpha_1 = 1$, $\alpha_2 = 1$, $\gamma = 500$, $\varepsilon = 3$, $\theta = 500$, $t = .1$, $Tol = 10^{-6}$. In the second row, $\mu = 20$. 58

3-4 A star shape. (a) is the original image with initial contour and landmarks, (b) is the segmentation result without landmarks, and (c) is the result using CVL. (d, e) are close-ups of (b, c) respectively. In (a-e), $\alpha_1 = 1$, $\alpha_2 = 1$, $\gamma = 1$, $\varepsilon = 3$, $\theta = 20$, $t = .1$, $Tol = 10^{-6}$. In (c, e), $\mu = 300$. 60

3-5 An ultrasound image. (b) is the segmentation result without landmarks, and (c) is the result using CVL and three landmarks. In (b,c), $\alpha_1 = 1$, $\alpha_2 = 1$, $\gamma = 500$, $\varepsilon = 3$, $\theta = 500$, $t = .1$, $Tol = 10^{-6}$. In (c), $\mu = 500$. 60

3-6 A clipped triangle. (b) is the segmentation result without using landmarks, (c) is the result using CVL and one landmark, and (d) is the result using CVL with multiple landmarks and more relaxed constraints. In (b-d), $\alpha_1 = 1$, $\alpha_2 = 1$, $\gamma = 1$, $\varepsilon = 3$, $t = .1$. In (b), $\theta = 20$, $\mu = 0$, $\zeta = 10^{-6}$. In (c), $\theta = 5 * 10^5$, $\mu = 5 * 10^5$, $\zeta = 10^{-8}$. In (d), $\theta = 4 * 10^3$, $\mu = 4 * 10^3$, $Tol = 10^{-6}$. 61

4-1 Results of four different methods of repair broken letters 'CV'. (a) is the original image, (b) is the initial contour, (c-f) are the segmentation results obtained cia the CV, CVL, CVE, and CVLE models respectively. The parameters are $\gamma_1 = 5, \gamma_2 = 5, \gamma_3 = 5, \gamma_4 = 5, \alpha_1 = 0.5, \alpha_2 = 0.5$. . 74

4-2 Repair of a broken rectangle. (a) is the original image, (b) is the initial contour and piror landmark, (c) is the result obtained from the CVL model, (d) is the result obtained from the CVLE model. The parameters are $\gamma_1 = 1, \gamma_2 = 3, \gamma_3 = 5, \gamma_4 = 10, \alpha_1 = 1.1, \alpha_2 = 0.9$ for the CVLE model. 75

4-3 Broken circle repair experiment. (a) is the original image, (b) is the initial contour and prior landmarks, (c) is the result obtained from the CVL model, (d) is the result obtained from the CVLE model. The parameters for the CVLE model are $\gamma_1 = 7, \gamma_2 = 20, \gamma_3 = 5, \gamma_4 = 2, \alpha_1 = 1.1, \alpha_2 = 1.2$. 76

4-4 Different number of landmarks affect the inpainted contour. (a-d) are the initial setups for 3, 9, 11, 15 landmarks respectively, (e-h) are the segmentation results via the CVLE for 3, 9, 11, 15 landmarks respectively. 77

4-5 The significance of the location of landmarks. (a-c) are the initial setups where landmarks are missing from the bottom, top, and middle of the missing corner of the rectangle respectively. (d-f) are the segmentation results for (a-c) respectively via the CVLE. (g) is the segmentation result using the full set of landmarks. 79

4-6 Brain MRI image segmentation experiment, image taken from [10]. (a) is the original image, (b) is the initial contour, (c) is the segmentation result via the CV model, (d) is the segmentation result via the CVLE model. 80

4-7 Noisy brain MRI image segmentation experiments, image taken from [8]. (a) is the original image, (b) is the initial contour, (c) is the segmentation result via the CV model, (d) is the segmentation result via the CVLE model. 80

5-1 Segmentation of two circles with the split-Bregman algorithm, image taken from [8]. (a) is the initial contour, (b-f) show the evolution of the contour. $\alpha = 4.5$, $\gamma = 5$, $\beta = 0.25$, $\mu = 8$, $l = 1$, $d = 4$, $window = 5 \times 5$, $S = 5$, $\varepsilon = 1$, $t = .05$, $Tol = 10^{-6}$. 93

5-2 Segmentation of synthetic hand with the split-Bregman algorithm, image taken from [8]. (a) is the initial contour, (b-f) show the evolution of the contour. $\alpha = 5$, $\gamma = 15$, $\beta = 0.5$, $\mu = 5$, $l = 1$, $d = 4$, $window = 7 \times 7$, $S = 5$, $\varepsilon = 1$, $t = .05$, $Tol = 10^{-6}$. 94

5-3 Segmentation of a brain, image taken from [8]. (a) is the original image, (b-c) uses the new Heaviside function with $\alpha = 10$, $\gamma = 15$, $\beta = 2$, $\mu = 5$, $l = 1$, $d = 4$, $window = 7 \times 7$, $S = 5$, $\varepsilon = 1$, $t = .1$, $Tol = 10^{-6}$. (d-e) uses the original Heaviside function with the same parameters. 95

5-4 Segmentation of cells (image taken from [10]). (a) is the initial contour, (b-c) show the process of contour evolution. $\alpha = 4$, $\gamma = 4$, $\beta = 0.2$, $\mu = 5$, $l = 1$, $d = 4$, $window = 7 \times 7$, $S = 5$ $\varepsilon = 1$, $t = .05$, $Tol = 10^{-6}$. 96

5-5 Segmentation of two orbs in 3D. The cyan surface is the zero level set and the black orbs are the objects. (a) is the initial contour, (b) is the final contour. $\alpha = 4$, $\gamma = 5$, $\beta = 0.2$, $\mu = 3$, $l = 1$, $d = 4$, $window = 5 \times 5$, $S = 5$ $\varepsilon = 1$, $t = .05$, $Tol = 10^{-6}$. 96

List of Symbols

Ω:	The domain of the image.
Ω_i:	The domain of image region i.
$\partial\Omega$:	The boundary of domain Ω.
C:	The curve.
$d(x, C)$:	The Euclidean distance from point x to curve C.
$T(x)$:	The unit tangent vector.
$N(x)$:	The unit normal vector.
κ:	The curvature.
$E(u)$:	The energy of the variational functional.
$\phi(x)$:	The level set function.
$\nabla\phi(x)$:	The discrete gradient of $\phi(x)$.
$\Delta\phi(x)$:	The Laplacian of $\phi(x)$.
$\nabla \cdot \vec{w}$:	The divergence of $\vec{w}$.
$H(\phi)$:	The Heaviside function of ϕ.
$H_\varepsilon(\phi)$:	The mollified Heaviside function of ϕ.
$\delta(\phi)$:	The Dirac function of ϕ.
$\delta_\varepsilon(\phi)$:	The mollified Dirac function of ϕ.
$\delta_R(\vec{m})$:	The characteristics function on the convex set R.
$g(x)$:	The edge detector function.
Tol:	The tolerance value for stopping optimization.

Publications

The following works contribute to the author's Master Degree thesis, ordered chronologically:

- **Pan, H.**, Liu, W., Li, L., and Zhou, G. (2019). A novel level set approach for image segmentation with landmark constraints. *Optik*, 182, 257-268.
- **Pan, H.**, Song, J., Liu, W., Li, L., Zhou, G., Tan, L., and Chen, S. (2020). Using the split Bregman algorithm to solve the self-repelling snake model. *http://arxiv.org/abs/2003.12693*
- Song, J., **Pan, H.**, Liu, W., Xu, Z., and Pan, Z. (2019). The Chan-Vese model with elastica and landmark constraints for image segmentation. *http://arxiv.org/abs/1905.11192*.

Attribution Statement

Chapters 3 to 5 of this thesis are based, solely or partly, on works that have been published with joint-authorship. We hereby make an authorship attribution statement to clarify the contribution of the author Huizhu Pan.

Chapter 3 is based on the publication:

- **Pan, H.**, Liu, W., Li, L., and Zhou, G. (2019). A novel level set approach for image segmentation with landmark constraints. *Optik*, 182, 257-268.

  The design and implementation of the model and the numerical algorithm, experimental results, and the writing of the publication can be attributed to Huizhu Pan.

Chapter 4 is based on the publication:

- **Pan, H.**, Song, J., Liu, W., Li, L., Zhou, G., Tan, L., and Chen, S. (2019). Using the split Bregman algorithm to solve the self-repelling snake model. *http://arxiv.org/abs/2003.12693*.

  The design and implementation of the numerical algorithm, experimental results (all except the 3D experiment), and the writing of the publication can be attributed to Huizhu Pan.

Chapter 5 is based partly on the publication, with additional unpublished work:

- Song, J., **Pan, H.**, Liu, W., Xu, Z., and Pan, Z. (2019). The Chan-Vese model with elastica and landmark constraints for image segmentation. *http://arxiv.org/abs/1905.11192*.

  The design of the model and the writing of the publication can be attributed to Huizhu Pan. With permission from all co-authors, Chapter 5 only includes parts

of the publication that can be attributed to Huizhu Pan. The parts included will not be used for the purpose of any other thesis. Additional unpublished work is also included in Chapter 5 that are not contained within this publication, such as an alternative solution to the proposed model via the split-Bregman algorithm and related experiments.

Signatures of co-authors:

Chapter 1

Introduction

1.1 Image segmentation

Image segmentation, i.e. the task of partitioning an image into subsections based on certain defined criteria, is a classical problem in computer vision and image analysis. By extracting meaningful parts of the image, we can further process or access them to glean more information. It is the basis for a variety of higher-level problems such as object detection and recognition, target tracking, three-dimensional (3D) reconstruction, etc. Its practical applications are limitless. To name a few, segmentation methods are useful for cropping objects in a photo editing software, detecting road conditions with self-driving cars, and rebuilding models of organs from computed tomography (CT) scans. The problem has been extensively studied in the past few decades, and many solutions were proposed that stemmed from disciplines such as statistics, applied mathematics, computer science, physics, etc. Recently, certain data-driven, end-to-end deep neural networks have achieved major breakthroughs in the field of image segmentation coupled with recognition and detection. Despite the immense progress, image segmentation remains an area of active research. One reason is that it generates a great amount of practical value, and another is that the problem itself is highly variable and complicated to solve. It is an inverse ill-posed problem, meaning that a unique segmentation is not guaranteed for a given image. The images may be captured differently, contaminated by different kinds of noise,

or missing information due to poor capturing condition. Some objects are hard to pick out in an image even by the human eye. As of now, notable issues still exist in the mainstream algorithms with respect to accuracy, speed, robustness, the level of human intervention, and the amount of specialized data required.

The image segmentation problem can be formally defined as follows. Let Ω be the domain of the image and $f(x) : \Omega \subset \mathbb{R}^m \rightarrow \mathbb{R}^p$ be the image, where m is the dimensionality and p is the number of channels in the image. We want to divide Ω into n sub-regions, $\Omega_1, \Omega_2, \ldots, \Omega_n$, such that,

- $\bigcup_{i=1}^{n} \Omega_i = \Omega$
- $\Omega_i \bigcup_{i \neq j} \Omega_j = \phi$

where each Ω_i corresponds to a meaningful partition of $f(x)$. By this definition, the task is to identify homogeneous regions in an image. For example, a color image can be approximated as blocks of uniform colors, where each block is a sub-region. Sometimes we may also define a curve $C \subset \mathbb{R}^m$, where C is the boundary of the sub-regions. In this case, the problem becomes the mapping of the segmentation contours boundaries of the objects in the image. The above two definitions are adopted by region-based and edge-based image segmentation methods respectively, as illustrated in Fig. 1-1 (c) and (e).

In computer vision, the techniques for image segmentation range from simple to sophisticated, hand-engineered heuristics to high-level abstraction and model design. Approaches such as thresholding [2], edge-detection [1], region-growing [11], and watershed [3] are directly based on pixels, e.g. whether the pixels are similarly colored, adjacent to each other, display sharp changes in intensity, etc. We consider these algorithms simple and classical, because the information utilized is low-level.

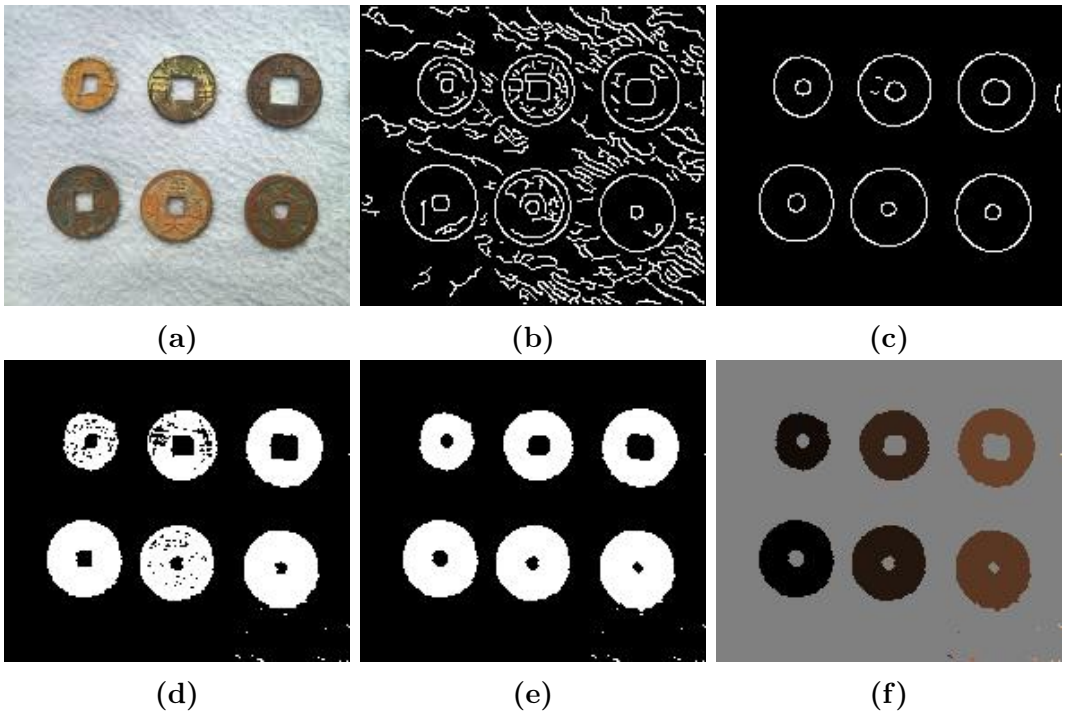

Fig. 1-1: Classical methods for image segmentation. (a) the original image, (b) image segmented with the Canny filter [1], (c) Gaussian-blurred image ($\sigma = 3.2$) segmented with the Canny filter, (d) image segmented with Otsu's thresholding method [2], (e) the previous result post-processed with morphological operations, (f) separation of the foreground instances with the watershed method [3].

One trait of classical approaches is that they tend to miss the "big picture", oftentimes leading to naive solutions. As shown in Fig. 1-1, the segmentation results in (b) and (d) leave much to be desired. Pre-processing and post-processing measure were introduced in (c) and (e) to improve accuracy. However, the additional steps also made the pipeline less robust and increased the number of parameters to tune. With more and more steps, the algorithm eventually becomes too convoluted and case-specific for real applications. To solve this dilemma, high-level models were designed that could organically combine the various parts of the algorithm while staying robust to the variabilities in the images.

There are many high-level models for the image segmentation problem. The more influential ones are based on neural networks [12], variational methods and partial differential equations (PDEs) [13, 14], graph combinatorial optimization [15], statistics and probability models such as Markov random fields [16], etc. These models

are versatile and able to incorporate many kinds of information and segmentation criteria. They transcend the simple combination of steps and aim to express the segmentation problem as a comprehensive model. Each model has its pros and cons, although generally speaking, the more information a model has access to (both from the image and pre-existing knowledge), and the more patterns it recognizes, the better the model tends to perform. Currently, artificial neural networks (ANNs) [12, 17] have taken center stage. The ANNs are combined networks of feature extraction filters, threshold switches, and other components whose parameters are tuned on a database of images. In other words, the segmentation criteria are "learned" from sample images rather than dictated by the human. This is a different line of thinking from the traditional one where models are designed from top to bottom. The ANNs often work well on the kinds of images they are trained on, making them ideal for engineering applications. Nonetheless, there are trade-offs. It takes much domain-specific data to tune a network for a task. If the network under-performs, changes are more difficult to implement. There is a general lack of understanding of machine learned parameters, and the collection of data and tweaking of hyperparameters is a long process. Overall, much uncertainty still remains, and a lot of research have been based mostly on experimentation. This thesis takes a mathematical approach and focuses on variational methods and PDE-based methods [18] instead, starting from the design of objective functionals to the derivation of solutions. It is the author's belief that both approaches hold merits and that concepts are often transferable between bodies of knowledge. A representative case in point is the variational autoencoder [19], a successful integration of variational Bayes in deep neural networks and the basis for some state-of-the-art image segmentation algorithms. More parallels and joint models are being investigated, such as in [20, 21].

Having said that, variational models are powerful and versatile in their own right. Similar to purely PDE-based methods, variational models are essentially mathematical formulations designed to describe real-world problems. The basic idea is to formulate an energy functional that, upon being minimized, yields the solution in the form of a function. The difference between purely PDE-based methods and varia-

tional methods is that the former directly defines the PDE while the latter derives it (a Euler-Lagrange equation) from the steady-state solution of the energy functional. This step involves the calculus of variations, hence the name "variational". Compared to pure PDE models, variational models are more intuitive and are easier to incorporate other models, such as those based on statistics and information theory. The mathematical theories of variational methods are based on the calculus of variations, PDEs, numerical analysis, differential geometry, viscosity solutions theory, and etc. [22]. With an abundance of theoretical tools, the existence and uniqueness of the solutions to the models can be proven in the continuous space, while efficient algorithm implementations can be realized in the discrete space with numerical optimization methods. Indeed, the versatility of variational models stems from its powerful framework of energy functional minimization. The functional constitutes a combination of terms that each serves a specific purpose. By playing with the terms, different functionals can be constructed to describe an extensive range of problems. Besides image segmentation, the variational paradigm has also been successfully implemented in areas of image processing such as denoising, deblurring, inpainting, compression, enhancement, motion analysis, 3D reconstruction, and etc. [23]. For image segmentation in particular, variational models based on color, edge, texture, motion, statistical distribution, shape prior, etc. have been proposed. Fig. 1-2 shows a few examples of image segmentation using variational models.

1.2 Variational models in image segmentation

As mentioned above, variational models are a special type of PDE-based models where the PDEs are derived from energy functionals. PDEs have always played a vital role in the modeling of real-world physical phenomenon, such as in the Maxwell's equations of electromagnetism, the Schrödinger's equation of quantum-mechanics, etc. The history of PDEs in image processing dates back to the discovery the equivalence of the Gaussian filter to the solution of the heat equation [24, 25]. From this concept emerged PDE-based models for image deblurring and enhancement such as

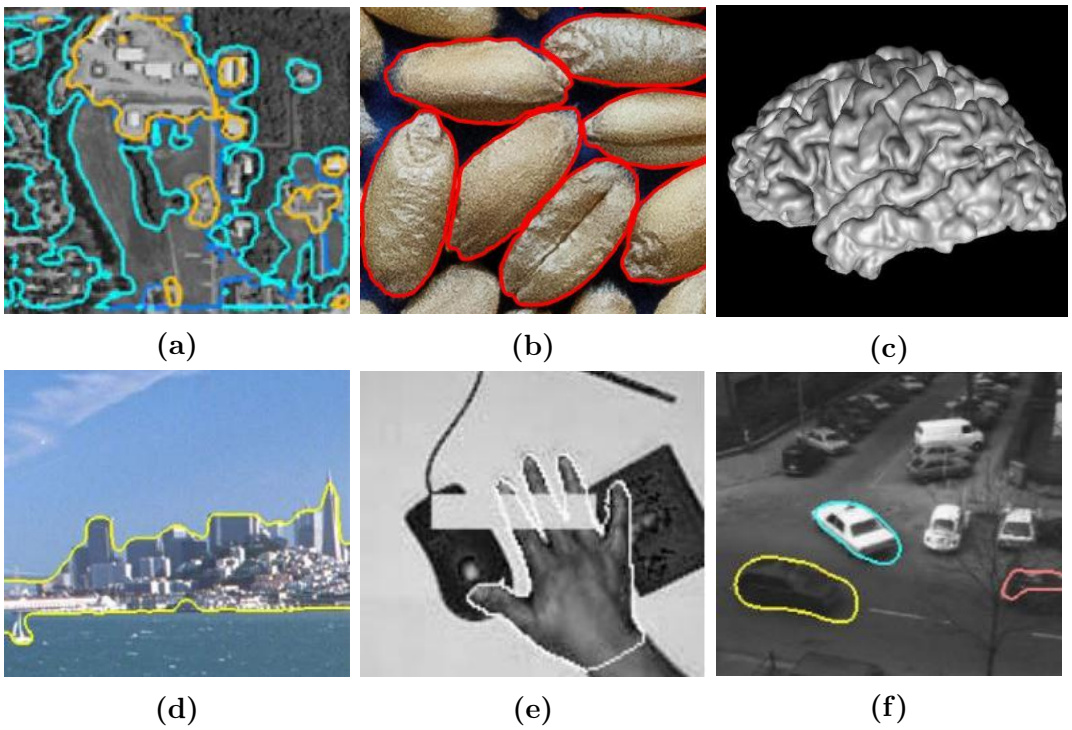

Fig. 1-2: Variational image segmentation based on (a) the piecewise constant assumption, (b) edges and topology preservation, (c) gradient vector flow, (d) color and texture, (e) shape priors, (f) optical flow. Results (a)(c)(d)(e)(f) are taken from [4, 5, 6, 7]

.

the Perona-Malik model [26]. Two variational models for image segmentation stood out at that time, the active contours model [13] and the Mumford-Shah model [27]. They paved the way for edge-based and region-based image segmentation models within the variational paradigm.

In 1988, Kass, Witkin and Terzopoulos proposed the active contours model (ACM, or snakes) [13]. In this variational model, curves delineating the segmentation contour gradually move towards the object edges, giving the appearance of "snakes". The curves were initially parametric functions, later on superseded by implicit representations. There were several problems with regards to the original ACM: the curves could be trapped by weak edges and noise, and then find it hard to move into recessed areas, and cannot change topology. The ensuing models worked to improve the ACM. To overcome potential weak edges and noise, Chohen et al. [28] proposed the addition of a balloon force that pushes the curves out of local minima. The gra-

dient vector flow velocity field proposed by Xu et al. [29, 30] moves the curves into recessed areas. Finally, implicit curve representations were adopted to resolve the issue of inflexible topology. Caselles et al. [31] and Malladi et al. [32] independently introduced the level set function [33] into the ACM in 1993 and 1995. In [31, 32], the level set (instead of the parametric curve) evolves through time and the contour is denoted by the zero level set. The nice mathematical properties of the level set function [33] enabled the implementation of some fast optimization methods and the variatioal level set framework enjoyed increasing popularity. In 1997, Caselles et al. [9] proposed the geodesic active contours (GAC) model, a much simplified but equally effective formulation of the ACM. The GAC model removes the higher-order terms and adopts the concept of geodesic distance in the Riemannian space. Many edge-based models designed thereafter are extensions of the GAC model.

The most representative region-based variational image segmentation model is the Mumford-Shah model [27] proposed in 1989. It aims to approximately recreate the image as piecewise smooth patches, where each patch is a sub-region of segmentation. The original model has one main problem, which is that the energy functional consists of both the recreated image and the contour; the dimensions of the two variables are mismatched. To solve the model in practice, approximations models are used based on Γ-convergence [34] and the level set method [14, 35]. In particular, the Chan-Vese (CV) model [14] using the level set approach has been widely popular. It is a simplification of the Mumford-Shah model by removing the higher-order term, and the scope of the problem is narrowed down to two-phase segmentation. Since its proposal, the CV model has been extended to multi-phase [36], and integrated with texture [37], motion [38], noise [39], shape priors [40, 41], etc. Compared to the edge-based models, region-based models are not concerned with weak edges and less dependent on initialization. However, they are also less sensitive to local details which led to lower segmentation accuracy. Kimmel et al. [42] combined the CV model and the GAC model to consider both edges and regions. More details on classical variational image segmentation models are presented in Chapter 2.

The theories of variational methods are based on the calculus of variations, PDEs,

numerical analysis, differential geometry, viscosity solutions theory, and etc. [22]. With this comprehensive set of tools, the existence and uniqueness of the solutions to the models can be proven in the continuous space, and efficient algorithm implementations can be realized in the discrete space with numerical optimization methods. Relevant theories from the calculus of variations, PDEs, and numerical analysis are presented in Chapter 2, with a focus on the variational level sets.

1.3 Current challenges

Though the variational paradigm opens up many possibilities, it also comes along with challenges. The minimization of the variational energy functional results in a Euler-Lagrange equation, a nonlinear PDE. Very rarely can this be solved analytically, and we must look for the steady-state solution of a dynamic equation via gradient descent most of the time. The iterative approach slows the algorithm down and imposes constraints on the time step, since convergence is now another factor to be considered. Furthermore, the discretization scheme, singularities, and boundary conditions must all be considered in concert to ultimately arrive at the correct solution. These issues all need to be addressed with the proposal of each new variational model. Attempts are also made to improve existing models through model simplification or methods to raise computational efficiency.

Fast optimization methods are often used to simplify and speed up the numerical algorithms. For example, the total variation (TV) term [14] is present in many variational level set models and serves the function of smoothing contours. It cannot be solved directly, and the gradient descent equation obtained through variational methods includes a curvature term. Calculating the curvature term in each iteration is computationally expensive, so split variable optimization methods are utilized to circumvent the term. By introducing auxiliary variables, the minimization problem can be broken down into some smaller sub-problems, which can then be minimized alternatingly. The dual method [35], split-Bregman method [43], augmented lagrangian method (ALM) [44], and the alternating directional method of multipliers (ADMM)

[45] are commonly used for this purpose.

Aside from optimization methods, the design of new variational models also poses a challenge. With the recent surge in "big data", the development of image segmentation algorithms has seen a shift in direction towards more usage of data. The reason behind this trend is that a database of images contains a rich pool of prior knowledge. To draw an analogy, the human recognizes an object not only based on visual perception, but also on previously learned knowledge about that object. The way that variational models tap into prior knowledge is through prior constraints. A typical example is the use of prior shapes to segment similarly shaped objects in images [7, 40, 41]. Aside from shapes, priors can take on many other forms such as probability maps in segmentation [21], noise distributions in denoising [20], etc. They can also be conveniently obtained through deep learning methods [46]. The works in this thesis explore two kinds of prior constraints in variational level set models for image segmentation, namely landmarks and topology.

1.3.1 Landmark priors

Landmarks are key points in images that denote important image features. They can be used in a number of image processing tasks. For example, in image registration, i.e. the matching of objects or object features in different images, landmarks are used to track a moving object in a series of frames. In image segmentation, they are used to specify target objects, improve segmentation contours, and inpaint missing sections of contours caused by object obstruction or damages to the image. Landmarks can be assigned manually or detected automatically via feature point extraction algorithms such as the scale-invariant feature transform (SIFT) [47], the speeded up robust features (SURF) [48], etc. Recent works in landmark localization [49] use deep learning methods to generate more accurate landmarks, which makes it possible to remove the human from the loop and perform segmentation in an end-to-end manner. Therefore, the subject of landmarks in image segmentation is now more relevant than ever.

Under the variational level set framework, however, there is no known model that enforces landmark constraints where the segmentation contour passes through the

landmarks. The works of this thesis aim to construct two new variational level set models that use landmarks to improve the quality of segmentation.

1.3.2 Topological priors

The topology of a geometric shape is the set of mathematical qualities that are preserved under continuous deformations. For a more intuitive understanding, let us consider two circles in 2D space. Deformations such as expansion and compression preserve the circles' topology, while merging and splitting do not. The idea is often referenced in active contour models, as the evolving contours are effectively deforming shapes. 1-3 illustrates the concept of topology preservation in image segmentation via active contours.

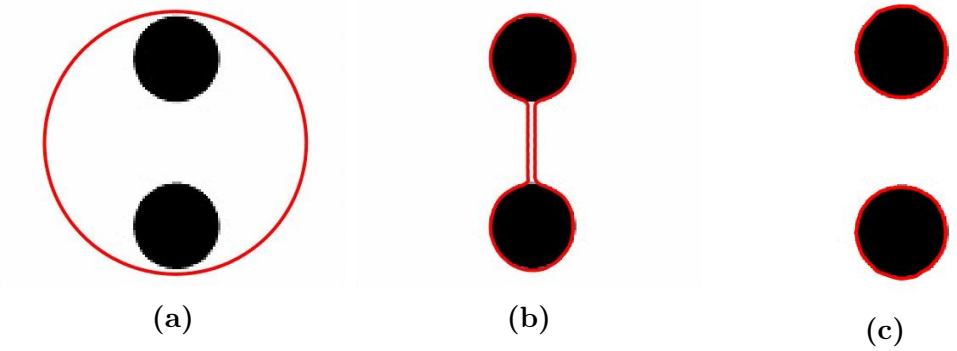

Fig. 1-3: Two circles segmented by the repulsive snakes model [8] and the GAC model [9], (a) initialization of the contour in red, (b) the contour with preserved topology, (d) the contour with altered topology.

.

Though a flexible contour topology is an important feature in active contour models, it also benefits to maintain the topology in certain situations. For instance, if the topology of the object is known in advance, we would like to preserve the initial topology in order to use the topological prior. One example application is the segmentation of cells in histopathology images, where cells are usually present in clusters and difficult to separate. Knowing the number of cells in advance (possibly through the detection of cell nuclei), we can use topology preservation to ensure the number of cells stays constant, thus preventing under-segmentation and over-segmentation.

This thesis aims to improve an existing topology preservation model, the self-repelling snakes (SR) model [8].

1.4 Research objectives

The objectives of research can be summarized as follows:

- To design a constraint term under the variational level set framework for landmarks-assisted image segmentation, where the contour passes through pre-defined landmark points.
- To experiment with the inclusion of constraints, i.e. landmark constraints, Euler's elastica, and topology preservation, in variational level set models and construct new models.
- To improve the numerical algorithm for SR model for image segmentation with topology preservation and increase the efficiency and robustness of the algorithm.
- To devise fast and memory efficient numerical algorithms for the variational models with constraints.

1.5 Structure of thesis and summary of contributions

The rest of the thesis concerns the theories behind variational level set models and the three novel works on variational image segmentation models with landmark and topology preservation constraints.

Chapter 2 reviews theories from the calculus of variations and PDEs, the level set formulation, and finite difference discretization schemes for approximating continuous derivatives. Some classical variational image segmentation models based on both edge and region features are also presented, with an emphasis on the level set

formulation for intrisic contour representation. To solve a variational model, we first derive its Euler-Lagrange equation representing the stationary state or energy minimum. Then, we derive its gradient flow and iteratively descend the functional to the energy minimum. The PDEs are discretized with the fitting numerical schemes. To simplify the optimization problem, we demonstrate the split-Bregman method for alternating direction minimization using the total variation model as an example.

Chapter 3 proposes a variational model to address the problem of region-based image segmentation assisted by pre-defined landmarks. Specifically, the segmentation contour is constrained to pass through the given landmark points. In the proposed Chan-Vese model with landmark constraints (CVL), the landmarks not only serve to guide the contour away from suboptimal segmentation results, but also to refine the contour in critical regions in order to increase the level of detail and accuracy n those regions. **The main contributions in this chapter are** the design of a new constraint term that embodies landmark information, the incorporation of the new constraint into the Chan-Vese model, the proof of convergence for the new model, and the proposal of a fast numerical solution for the new model based on the split-Bregman method and projection method. Experimental results on synthetic, noisy, and real-world CT images illustrate the effectiveness of the CVL model.

Chapter 4 proposes an extension to the CVL model that interpolates long illusory contours with the help of landmarks. This is useful for segmenting occluded or damaged objects, where the contour information is missing in the image and may be given by landmarks. Though the CVL model is effective otherwise, it is not suitable for connecting landmarks to the segmentation contour when they are too far away from the object boundary. One the other hand, the Euler's elastica has been used successfully in image and contour interpolation or inpainting. With the proposed Chan-Vese model with landmark constraints and elastica (CVLE), farther landmarks can now be connected and fewer landmarks are required, facilitating the creation of illusory contours. **The main contributions in this chapter are** the design of the new model incorporating the elastica term into the CVL, and the proposal of a fast numerical solution for the CVLE using the split-Bregman method with projection.

Experimental results on synthetic images with damages and real-world MRI images with noise demonstrate the inpainting capability of the CVLE.

Chapter 5 presents a new solution to the self-repelling snakes (SR) model. The SR model segments the image by edges and makes use of repulsion between the contours to preserve contour topology. The original solution based on additive operator splitting has a memory requirement the square of the image size. The new solution via the split-Bregman method with projection simplifies the optimization problem and reduces the memory requirement down to a linear dependency. The stability of the SR model is also enhanced through a different Heaviside function which restricts the repulsive force to narrow bands around the contour. **The main contributions in this chapter are** a proposed fast numerical solution for the SR model using the split-Bregman method with projection, and the replacement of the original Heaviside function. Experimental results on synthetic images and real-world medical images show that the new solution has comparable performance to the original one, while stability has improved noticeably.

Chapter 6 summarizes the contributions of the thesis. The impacts of the current works are discussed and potential directions of future research are speculated.

Chapter 2

Variational Image Segmentation Models

2.1 Variational methods

The core of variational models lies in the construction of energy functionals and the devising of their solutions. In a variational model, a functional is designed to describe a problem such that the minimization of the functional yields the solution to the problem as a function. Let a function be two-dimentional with continuous first order derivatives, $u(x) : \Omega \subset \mathbb{R}^2 \to \mathbb{R}$ where $x = (x_1, x_2) \in \Omega$, $dx = dx_1 dx_2$. Let the energy functional be dependent on up to the first order derivative of $u(x)$, such that

$$E(u) = \int_\Omega F(x, u(x), \nabla u(x)) dx. \tag{2.1}$$

Note that the energy functional is the integration of the functional F that describes the problem over the domain of the image. The minimum of the energy functional can be found when the first order variation of (2.1) reaches 0. In other words, the Gâteaux derivative $\frac{\partial E(u)}{\partial u} = 0$. The problem can be formally framed as follows: For all $\eta(x)$ and an infinitely small number ξ, the solution to the minimization problem satisfies

$$< \frac{\partial E(u)}{\partial u}, \eta >= \lim_{\xi \to 0} \frac{E(u+\xi\eta) - E(u)}{\xi} = \frac{\partial E(u+\xi\eta)}{\partial \xi}|_{\xi=0} = 0 \tag{2.2}$$

Plugging the standard energy functional (2.1) into (2.2), we can derive

$$\begin{aligned} < \frac{\partial E(u)}{\partial u}, \eta > &= \frac{\partial}{\partial \xi}|_{\xi=0} \int_\Omega F(x, u+\xi\eta, \nabla u + \xi\nabla\eta)dx \\ &= \int_\Omega \frac{\partial}{\partial \xi} F(x, u+\xi\eta, \nabla u + \xi\nabla\eta)dx \\ &= \int_\Omega (F_u \eta + F_{\nabla u} \cdot \nabla\eta)dx, \end{aligned} \tag{2.3}$$

where $F_u = \frac{\partial F}{\partial u}$ and $F_{\nabla u} = \frac{\partial F}{\partial(\nabla u)} = \begin{pmatrix} \frac{\partial F}{\partial u_{x1}} \\ \frac{\partial F}{\partial u_{x2}} \end{pmatrix}$. Applying the Green's formula to the second term in (2.3) yields

$$< \frac{\partial E(u)}{\partial u}, \eta >= \int_\Omega (F_u - \nabla \cdot (F_{\nabla u}))\eta dx + \int_{\partial\Omega} F_{\nabla u} \cdot \vec{n}\eta ds, \tag{2.4}$$

where $\vec{n}$ is the outward normal vector on the boundary $\partial\Omega$. For (2.4) to satisfy the stability condition (2.2), the integral must reach 0 both within the image and on the boundary. Therefore, we can derive the Euler-Lagrange function with the boundary condition as

$$\begin{cases} F_u - \nabla \cdot (F_{\nabla u}) = 0 & x \in \Omega \\ F_{\nabla u} \cdot \vec{n} = 0 & x \in \partial\Omega. \end{cases} \tag{2.5}$$

The derivation of Euler-Lagrange functions is a crucial first step to solving variational models.

2.2 Gradient descent equations

The Euler-Lagrange equations are nonlinear PDEs that typically cannot be solved analytically. In order to derive the minima $\hat{u}$ dynamically, we introduce a time factor, t, and evolve the function u in the direction of gradient descent, such that

$$\frac{\partial u}{\partial t} = -\frac{\partial E}{\partial u} \tag{2.6}$$

With respect to (2.1), the dynamic energy functional is

$$E(u(x,t)) = \int_{\Omega} F(x, u(x,t), \nabla u(x,t))dx \tag{2.7}$$

To minimize the energy functional, we update E such that $\frac{\partial E}{\partial t} \leq 0$. The gradient can be derived as below

$$\begin{aligned}
\frac{\partial E}{\partial t} &= \int_{\Omega} \left(F_u u_t + \frac{\partial F}{\partial \xi} (\nabla u)_t \right) dx \\
&= \int_{\Omega} \left(F_u u_t - \nabla \cdot F_{\nabla u} u_t \right) dx + \int_{\partial \Omega} \frac{\partial F}{\partial \vec{n}} u_t ds \\
&= \int_{\Omega} (F_u - \nabla \cdot F_{\nabla u}) u_t dx,
\end{aligned} \tag{2.8}$$

where $u_t = \frac{\partial u}{\partial t}$ and $(\nabla u)_t = \frac{\partial (\nabla u)}{\partial t}$. The first step uses the Green's theorem and the the next step applies the Neumann boundary condition where $\frac{\partial F}{\partial \vec{n}} = 0$ to eliminate the third r.h.s. term in (2.8).

Since the goal is to ensure that $\frac{\partial E}{\partial t} \leq 0$, we can set u_t as

$$\frac{\partial u}{\partial t} = -\left(F_u - \nabla \cdot F_{\nabla u} \right) \tag{2.9}$$

which is the gradient flow for gradient descent. $\hat{u}$ can be found when $\frac{\partial E}{\partial t} < Tol$ where Tol is a small tolerance value.

2.3 The level set method

In variational models for image segmentation, the solution $\hat{u}$ denotes the segmentation contour or the association of pixels to disjoint subsections. This can be represented explicitly or implicitly. For example, a 2D segmentation contour can be a parametric curve, $C = \{x \in \Omega | x = (x_1(q), x_2(q)), q \in [0,1]\}$. Implicit representations generally allow for more flexibility in curve evolution. One popular for-

mulation that embeds the contour in a higher dimension is the level set function [33, 31, 32], where $\phi(x) : \Omega \subset \mathbb{R}^n \rightarrow \mathbb{R}$ and the segmentation contour is defined as $C = \{x \in \Omega | \phi(x) = n, n \in \mathbb{Z}\}$, or the level line of $\phi(x)$ at n. For two phase segmentation, the level line at zero often denotes the contour, as shown in Fig. 2-1.

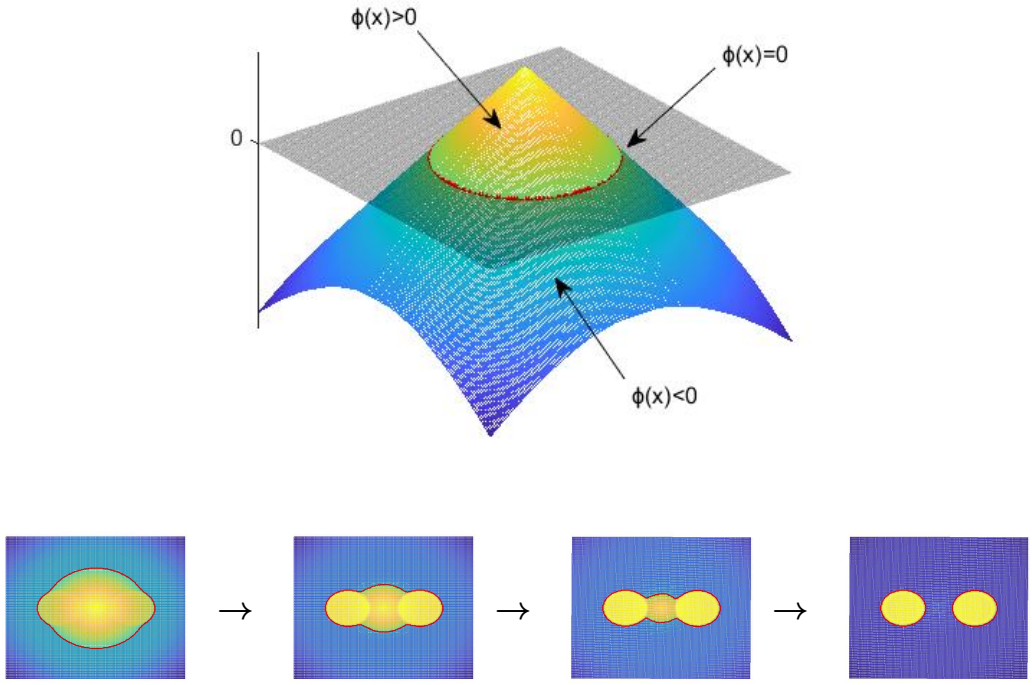

Fig. 2-1: The function $\phi(x)$ over a 2D image domain for the two phase segmentation problem. $\phi(x) > 0$ denotes the object, $\phi(x) < 0$ denotes the background, and $\phi(x) = 0$ marks the segmentation contour in red. The top-down view shows how the contour changes topology (splits) as it evolves.

.

$\phi(x)$ is often chosen to be a signed distance function, such that

$$\phi(x) = \begin{cases} d(x, C) & if\ x \in \Omega_1 \\ 0 & if\ x \in C \\ -d(x, C) & if\ x \in \Omega_2 \end{cases}, \tag{2.10}$$

where $d(x, C)$ is the Euclidean distance from a point to the segmentation contour C, and Ω_1 and Ω_2 are the two subdomains. The signed distance function has the

property

$$|\nabla\phi(x)| = 1. \tag{2.11}$$

Compared to the parametric curve, the level set function allows for free changes in the topology of the contour. Furthermore, many geometric quantities can be represented more intuitively. To describe the areas of the subsections and the length of the contour, we introduce a Heaviside function $H(\phi(x))$,

$$H(\phi(x)) = \begin{cases} 1 & if\ \phi(x) \geq 0 \\ 0 & otherwise. \end{cases} \tag{2.12}$$

It is easy to see that the area of Ω_1 is just $\int_\Omega H(\phi(x))dx$ and the area of Ω_2 is $\int_\Omega H(1-\phi(x))dx$. The length of C is $\int_\Omega |\nabla H(\phi(x))|dx$, as the value of H changes only upon the contour. The partial derivative of $H(\phi(x))$with respect to ϕ is the Dirac function

$$\delta(\phi(x)) = \frac{\partial H(\phi(x))}{\partial\phi(x)}. \tag{2.13}$$

On the other hand, to observe the other geometric quantities relating to the segmentation contour, we can express the contour through a curve coordinate, such that

$$\phi(x(s)) = 0, \tag{2.14}$$

and the derivative of the contour with respect to the curve coordinate is

$$\nabla\phi(x(s)) \cdot x_s = 0. \tag{2.15}$$

Thus, the unit tangent vector, unit normal vector and curvature on the contour can be defined as

$$T(x) = \frac{x_s}{|x_s|}, \tag{2.16}$$

$$N(x) = \frac{\nabla\phi(x)}{|\nabla\phi(x)|}, \tag{2.17}$$

$$\kappa = \nabla \cdot \left(\frac{\nabla\phi(x)}{|\nabla\phi(x)|} \right). \tag{2.18}$$

Introducing the time factor t, we can observe the time evolution of the contour. While it evolves, the contour satisfies the following condition

$$\phi(x(t), t) = 0, \tag{2.19}$$

the derivative of (2.19) with respective to t is

$$\frac{\partial\phi(x,t)}{\partial t} + \nabla\phi(x,t) \cdot \frac{\partial x(t)}{\partial t} = 0. \tag{2.20}$$

Substituting (2.17) into (2.20), we can derive the standard level set equation

$$\frac{\partial\phi(x,t)}{\partial t} + v_N|\nabla\phi(x)| = 0, \tag{2.21}$$

where $v_N = \frac{\partial x(t)}{\partial t} \cdot N(x)$ is the speed function of curve evolution. In fact, (2.21) is a typical dynamic Hamilton-Jacobi equation in physics.

2.4 Variational models

As mentioned earlier, variational models are constructed as the integral of a functional over the domain of an image. To gain more insight into the nature of the functionals, we present some classical variational models for image segmentation below.

2.4.1 Edge-based models

The pioneering work by Kass, Witkin and Terzopoulos [13] know as the active contour model (ACM), or the snakes model, is an energy functional minimization

problem over a closed elastic curve, shown as below,

$$\min_c E(C) = \alpha \int_0^1 |C_{pp}(p)|^2 \, dp + \beta \int_0^1 |C_p(p)|^2 \, dp + \gamma \int_0^1 g^2(C(p)) dp, \tag{2.22}$$

where $C(p)$ is a parametric curve with $p \in [0, 1]$. The first and second terms are the inner elastic energy of the curve, while the third term is the external energy based on an edge detector

$$g(C(p)) = \frac{1}{1 + v \left| \nabla \left(G_\sigma * f(C(p)) \right) \right|^2} \tag{2.23}$$

where α, β, γ are standard weighting parameters. Using standard variational methods [18], we can obtain its static Euler-Lagrange equation and the corresponding gradient descent equation for curve evolution as

$$\alpha C_{pppp} - \beta C_{pp} + \gamma g \nabla g = 0 \tag{2.24}$$

$$\frac{\partial C}{\partial t} + \alpha C_{pppp} - \beta C_{pp} + \gamma g \nabla g = 0. \tag{2.25}$$

The original model suffers from one major problem, that it is overly dependent on parameterization. Later on, Caselles, Kimmel and Sapiro [9] proposed the celebrated geodesic active contour (GAC) model which minimizes the geodesic length of the contour (a quantity independent of parameterization),

$$\min_c E(C) = \int_0^1 g(C(p)) \, |C_p| \, dp = \int_L g(C(s)) ds. \tag{2.26}$$

The corresponding curve evolution equation is

$$\frac{\partial C}{\partial t} = (\kappa g - (\nabla g \cdot N)) N. \tag{2.27}$$

The GAC model is often distracted by weak edges and noise interference. To overcome this problem, a balloon force was later added,

$$\frac{\partial C}{\partial t} = ((\alpha + \kappa)g - (\nabla g \cdot N))N. \tag{2.28}$$

The main drawback of models (2.25), (2.27) and (2.28) is that they cannot handle the problem of topology adaption due to the external parametrization of the curve. On the other hand, the level set method is a good choice for the dynamic evolution of curves and surfaces with adaptive topology. Substituting (2.28) into (2.20), we can obtain the dynamic evolution equation of the curve in the form of the level set equation (2.21) as

$$\frac{\partial \phi}{\partial t} = \nabla g \cdot \nabla \phi + \alpha g |\nabla \phi| + \kappa g |\nabla \phi| \tag{2.29}$$

The GAC model (2.26) can be rewritten under the variational level set framework as

$$\min_{\phi} E(\phi) = \int_{\Omega} g(x) |\nabla H(\phi(x))| dx = \int_{\Omega} g(x) |\nabla \phi(x)| \delta(\phi(x)) dx. \tag{2.30}$$

Its dynamic evolving equation can be obtained via variational method and the gradient descent strategy as below

$$\frac{\partial \phi}{\partial t} = \delta(\phi(x)) \nabla \cdot \left(g(x) \frac{\nabla \phi(x)}{|\nabla \phi(x)|} \right). \tag{2.31}$$

Replacing $\delta(\phi(x))$ with $|\nabla \phi(x)|$, the parabolic equation (2.31) can be transformed into the following hyperbolic equation, i. e., a Hamilton-Jacobi equation with second order derivatives,

$$\frac{\partial \phi}{\partial t} = |\nabla \phi(x)| \nabla \cdot \left(g(x) \frac{\nabla \phi(x)}{|\nabla \phi(x)|} \right). \tag{2.32}$$

The above is in fact the same as (2.29) with no balloon force.

2.4.2 Region-based models

Region-based variational models for image segmentation are typically more robust than edge-based models. They divide the images into different sub-regions as determined by region-based features, e.g. mean intensity, variance of intensity, colors, etc.. The first region-based variational image segmentation model was proposed by Mumford and Shah [27]. It approximates the image using piecewise smooth regions divided by boundaries with minimal length. The formulation is

$$\min_{u,C} E(u,C) = \alpha \int_{\Omega} (f-u)^2 dx + \beta \int_{\Omega/C} |\nabla u|^2 dx + \gamma \int_C ds. \tag{2.33}$$

The first term on the r.h.s. is a data term that controls the similarity between the original image f and the piecewise smooth (approximated) image u. The second term controls the smoothness of u, the third term controls the length of boundaries, and α, β, γ are three tuning parameters.

It is difficult to solve the Mumford-Shah model (2.33) directly since u and C are in two dimensional space and one dimensional space respectively. If curve C divides Ω into two sub-regions Ω_1 and Ω_2 such that $\Omega = \Omega_1 \cup \Omega_2$ and $\Omega_1 \cap \Omega_2 = \varnothing$, and we let

$$u(x) = \begin{cases} u_1(x) & x \in \Omega_1 \\ u_2(x) & x \in \Omega_2 \end{cases}, \tag{2.34}$$

(2.33) can be restated as

$$\begin{aligned} \min_{u_1,u_2,C} E(u_1,u_2,C) = \alpha &\left(\int_{\Omega_1} (f-u_1)^2 dx + \int_{\Omega_2} (f-u_2)^2 dx \right) \\ &+ \beta \left(\int_{\Omega_1} |\nabla u_1|^2 dx + \int_{\Omega_2} |\nabla u_2|^2 dx \right) + \gamma \int_C ds, \end{aligned} \tag{2.35}$$

Chan and Vese [14] simplified (2.35) by making the piecewise constant approximation rather than piecewise smooth,

$$\min_{u_1,u_2,C} E\left(u_1,u_2,C\right) = \alpha_1 \int_{\Omega_1} \left(f-u_1\right)^2 dx + \alpha_2 \int_{\Omega_2} \left(f-u_2\right)^2 dx + \gamma \int_C ds. \quad (2.36)$$

Finally, the well-known Chan-Vese model [14] was proposed under the variational level set framework as

$$\begin{aligned} \min_{u_u,u_2,\phi} E\left(u_1,u_2,\phi\right) = \alpha_1 &\int_\Omega \left(f-u_1\right)^2 H(\phi) dx \\ &+ \alpha_2 \int_\Omega \left(f-u_2\right)^2 \left(1-H(\phi)\right) dx + \gamma \int_\Omega |\nabla H(\phi)| dx. \end{aligned} \quad (2.37)$$

2.5 The numerical methods

Having established the energy functional, the function formulation, and the gradient flow of the function, the next step is to put the continuous functions into discrete space. Since the image is a discrete matrix (consisting of pixels at vector coordinate), the PDEs must be discretized with numerical methods. Next, we will look at some numerical methods for discretizing typical parabolic and hyperbolic equations.

2.5.1 Discretization

As seen in the previous sections, the PDEs in variational models may involve quantities relating to derivatives, such as the gradient $\nabla\phi = [\partial_{x_1}\phi, \partial_{x_2}]^\intercal$, divergence $\nabla\cdot\vec{w} = \partial_{x_1}w_1 + \partial_{x_1}w_2$, Laplacian $\Delta\phi(x) = \nabla\cdot(\nabla\phi(x))$, curvature $\kappa(x) = \nabla\cdot\left(\frac{\nabla\phi(x)}{|\nabla\phi(x)|}\right)$, and geodesic curvature $\kappa_g(x) = \nabla\cdot\left(g(x)\frac{\nabla\phi(x)}{|\nabla\phi(x)|}\right)$, etc. All of the above should be approximated to discretized forms corresponding to the images.

For an image of size $M\times N$ with indices $i = 0,1,2,\ldots,M-1$, $j = 0,1,2,\ldots,N-1$, we let the spacial step be one pixel, then, $x_{1i} = i$, $x_{2j} = j$, and $\phi_{i,j} = \phi\left(x_{1i}, x_{2j}\right)$. For the time-wise discretization, we let the time step be τ, then the time at step k is $t_k = k\tau, (k = 0,1,\ldots)$.

The gradient with regards to first order partial derivatives can be approximated with the first order forward finite difference, backward finite difference or central finite difference below

$$\nabla^{+}\phi_{i,j} = \begin{bmatrix} \partial^{+}_{x_i}\phi_{i,j} \\ \partial^{+}_{x_i}\phi_{i,j} \end{bmatrix} = \begin{bmatrix} \phi_{i+1,j} - \phi_{i,j} \\ \phi_{i,j+1} - \phi_{i,j} \end{bmatrix}, \tag{2.38}$$

$$\nabla^{-}\phi_{i,j} = \begin{bmatrix} \partial^{-}_{x}\phi_{i,j} \\ \partial^{-}_{x_i}\phi_{i,j} \end{bmatrix} = \begin{bmatrix} \phi_{i,j} - \phi_{i-1,j} \\ \phi_{i,j} - \phi_{i,j-1} \end{bmatrix}, \tag{2.39}$$

$$\nabla^{0}\phi_{i,j} = \begin{bmatrix} \partial^{0}_{x_1}\phi_{i,j} \\ \partial^{0}_{x_2}\phi_{i,j} \end{bmatrix} = \begin{bmatrix} \frac{1}{2}\left(\phi_{i+1,j} - \phi_{i-1,j}\right) \\ \frac{1}{2}\left(\phi_{i,j+1} - \phi_{i,j-1}\right) \end{bmatrix}. \tag{2.40}$$

Similarly, the divergence $\nabla \cdot \vec{w}$ may have three forms of discretization. For example, its backward finite difference is

$$\nabla \cdot \vec{w}_{i,j} = \partial^{-}_{x_1} w_{\mathrm{li},j} + \partial^{-}_{x_2} w_{2i,j} = w_{1i,j} - w_{1i-1,j} + w_{2i,j} - w_{2i,j-1}. \tag{2.41}$$

The Laplacian is a parabolic operator. It should be discretized via the forward and backward finite differences, or the central finite difference at half point as

$$\Delta\phi_{i,j} = \nabla^{-} \cdot \left(\nabla^{+}\phi_{i,j}\right) = \phi_{i+1,j} + \phi_{i-1,j} + \phi_{i,j+1} + \phi_{i,j-1} - 4\phi_{i,j}. \tag{2.42}$$

Curvature is a nonlinear parabolic operator,

$$\kappa_{i,j} = \nabla^{-} \cdot \left(\frac{\nabla^{+}\phi_{i,j}}{|\nabla^{+}\phi_{i,j}|}\right) = c_{1i,j}\phi_{i+1,j} + c_{2i,j}\phi_{i-1,j} + c_{3i,j}\phi_{i,j+1} + c_{4i,j}\phi_{i,j-1} + c_{i,j}\phi_{i,j}, \tag{2.43}$$

where,

$$c_{i,j} = c_{1i,j} + c_{2i,j} + c_{3i,j} + c_{4i,j}, \tag{2.44}$$

$$c_{1i,j} = \frac{1}{\sqrt{\left(\phi_{i+1,j} - \phi_{i,j}\right)^2 + \left(\phi_{i,j+1} - \phi_{i,j}\right)^2 + \varepsilon}}, \tag{2.45}$$

$$c_{2i,j} = \frac{1}{\sqrt{\left(\phi_{i,j} - \phi_{i-1,j}\right)^2 + \left(\phi_{i-1,j+1} - \phi_{i-1,j}\right)^2 + \varepsilon}}, \tag{2.46}$$

$$c_{3i,j} = \frac{1}{\sqrt{\left(\phi_{i+1,j} - \phi_{i,j}\right)^2 + \left(\phi_{i,j+1} - \phi_{i,j}\right)^2 + \varepsilon}}, \tag{2.47}$$

$$c_{4i,j} = \frac{1}{\sqrt{\left(\phi_{i+1,j-1} - \phi_{i,j-1}\right)^2 + \left(\phi_{i,j} - \phi_{i,j-1}\right)^2 + \varepsilon}}. \tag{2.48}$$

The geodesic curvature is usually discretized via the central finite difference at half point

$$\begin{aligned} k_{gi,j} &= \partial^0_{x_1}\left(a_{i+\frac{1}{2},j}\partial^0_{x_1}\phi_{i+\frac{1}{2},j}\right) + \partial^0_{x_2}\left(a_{i,j+\frac{1}{2}}\partial^0_{x_1}\phi_{i,j+\frac{1}{2}}\right) \\ &= c_{1i,j}\phi_{i+1,j} + c_{2i,j}\phi_{i-1,j} + c_{3i,j}\phi_{i,j+1} + c_{4i,j}\phi_{i,j-1} + c_{i,j}\phi_{i,j} \end{aligned} \tag{2.49}$$

where,

$$c_{i,j} = c_{1i,j} + c_{2i,j} + c_{3i,j} + c_{4i,j}, \tag{2.50}$$

$$c_{1i,j} = a_{i+\frac{1}{2},j} = \frac{1}{2}\left(a_{i+1,j} + a_{i,j}\right), c_{2i,j} = a_{i-1,j} = \frac{1}{2}\left(a_{i-1,j} + a_{i,j}\right), \tag{2.51}$$

$$c_{3i,j} = a_{i,j+\frac{1}{2}} = \frac{1}{2}\left(a_{i,j+1} + a_{i,j}\right), c_{4i,j} = a_{i,j-\frac{1}{2}} = \frac{1}{2}\left(a_{i,j-1} + a_{i,j}\right), \tag{2.52}$$

and $\kappa_g = \nabla \cdot \left(g\frac{\nabla\phi}{|\nabla\phi|}\right) = \nabla \cdot (a\nabla\phi)$, $a = \frac{g}{|\nabla\phi|}$.

For the Hamilton-Jacobi equations, for example (2.29), that include both hyperbolic and parabolic components, choosing the correct finite difference schemes is very important to numerical stability. Usually, the up-wind scheme is used on the hyper-

bolic parts and the central finite difference method is used on the parabolic parts. For example, the terms in (2.29) can be approximated as

$$\begin{aligned}\nabla g_{i,j} \cdot \nabla \phi_{i,j} = &\max\left(\partial_{x_1} g_{i,j}, 0\right) \partial_x^+ \phi_{i,j} + \min\left(\partial_{x_1} g_{i,j}, 0\right) \partial_{x_2}^- \phi_{i,j} \\ &+ \max\left(\partial_{x_1} g_{i,j}, 0\right) \partial_{x_2}^+ \phi_{i,j} + \min\left(\partial_{x_2} g_{i,j}, 0\right) \partial_{x_2}^- \phi_{i,j},\end{aligned} \tag{2.53}$$

$$\begin{aligned}\alpha_{i,j} \left|\nabla \phi_{i,j}\right| = &\min\left(\alpha_{i,j}, 0\right) \sqrt{\begin{array}{l}\max\left(\partial_{x_1}^- \phi_{i,j}, 0\right)^2 + \min\left(\left(\partial_{x_1}^+ \phi_{i,j}, 0\right)\right)^2 \\ + \max\left(\partial_{x_2}^- \phi_{i,j}, 0\right)^2 + \min\left(\left(\partial_{x_2}^+ \phi_{i,j}, 0\right)\right)^2\end{array}} \\ &+ \max\left(\alpha_{i,j}, 0\right) \sqrt{\begin{array}{l}\min\left(\partial_{x_1}^- \phi_{i,j}, 0\right)^2 + \max\left(\left(\partial_{x_1}^+ \phi_{i,j}, 0\right)\right)^2 \\ + \min\left(\partial_{x_2}^- \phi_{i,j}, 0\right)^2 + \max\left(\left(\partial_{x_2}^+ \phi_{i,j}, 0\right)\right)^2\end{array}}.\end{aligned} \tag{2.54}$$

Overall, the discretization of curvature, geodesic curvature, and hyperbolic terms are very complicated. One of the alternatives to avoid this process is to introduce splitting variables and transform the original problem into a series of simpler sub-problems of optimization. Next, we present the split-Bregman algorithm.

2.5.2 The split-Bregman algorithm

The split-Bregman algorithm was proposed by Goldstein and Osher [43] to solve the classic total variation (TV) model [50] for image restoration. The formulation for the TV model is

$$\min_u E(u) = \frac{1}{2} \int_\Omega (u - f)^2 dx + \gamma \int_\Omega |\nabla u| dx, \tag{2.55}$$

where, f is an observed image with noises, u is the restored clear image, and γ is a penalty parameter. Its Euler-Lagrange equation is

$$\begin{cases} u - f - \gamma \nabla \cdot \left(\frac{\nabla u}{|\nabla u|}\right) = 0 & x \in \Omega \\ \nabla u \cdot \vec{n} = 0 & x \in \partial\Omega \end{cases}, \tag{2.56}$$

which, as we can see, includes curvature. The discretization of the curvature is a

source of complications. To bypass the curvature term, we can introduce an auxiliary variable $\vec{w} = \nabla u$ to transform (2.55) into the following minimization problem with an added constraint

$$\begin{cases} \min E(u, \vec{w}) = \frac{1}{2}\int_\Omega (u-f)^2 dx + \gamma \int_\Omega |\vec{w}| dx \\ \text{s.t. } \vec{w} = \nabla u \end{cases}. \tag{2.57}$$

The split-Bregman algorithm for alternating optimization can then be derived as

$$\left(u^{k+1}, \vec{w}^{k+1}\right) = \arg\min_{u,\vec{w}} E\left(u, \vec{w}, \vec{b}^k\right) = \left\{ \begin{array}{l} \frac{1}{2}\int_\Omega (u-f)^2 dx + \gamma \int_\Omega |\vec{w}| dx \\ +\frac{\mu}{2}\int_\Omega \left|\vec{w} - \nabla u - \vec{b}^k\right|^2 dx \end{array} \right\}, \tag{2.58}$$

$$\vec{b}^{k+1} = \vec{b}^k - \left(\vec{w}^{k+1} - \nabla u^{k+1}\right), \tag{2.59}$$

In each iteration, the original problem is decomposed into two simpler sub-problems, i. e., for $k = 0, 1, 2, \ldots$, the first minimization problem on u is

$$u^{k+1} = \arg\min_u E\left(u, \vec{w}^k, \vec{b}^k\right) = \frac{1}{2}\int_\Omega (u-f)^2 dx + \frac{\mu}{2}\int_\Omega \left|\vec{w} - \nabla u - \vec{b}^k\right|^2 dx. \tag{2.60}$$

The Euler-Lagrange equation for u can be obtained via standard variational methods as

$$\begin{cases} u - f + \mu\nabla \cdot \left(\vec{w}^k - \nabla u - \vec{b}^k\right) & x \in \Omega \\ \left(\vec{w}^k - \nabla u - \vec{b}^k\right) \cdot \vec{n} = 0 & x \in \partial\Omega \end{cases} \tag{2.61}$$

Let $\bar{f}^k = f + \mu\nabla \cdot \left(\vec{b}^k - \vec{w}^k\right)$, it then becomes a simple Helmholtz equation as

$$u - \bar{f}^k - \mu\Delta u = 0, \tag{2.62}$$

which has a simple discrete form

$$u_{i,j} - \bar{f_{i,j}^k} - \mu \left(u_{i+1,j} + u_{i-1,j} + u_{i,j+1} + u_{i,j-1} - 4u_{i,j} \right) = 0. \tag{2.63}$$

Its Gauss-Seidel iterative algorithm is

$$u_{i,j}^{k+1,l+1} = \frac{\bar{f_{i,j}^k} + \mu \left(u_{i+1,j}^{k+1,l} + u_{i-1,j}^{k+1,l+1} + u_{i,j+1}^{k+1,l} + u_{i,j-1}^{k+1,l+1} \right)}{(1+4\mu)}, u_{i,j}^{k+1,0} = u_{i,j}^k, (l = 0, 1, 2, \dots), \tag{2.64}$$

On the other hand, the sub-problem on $\vec{w}$ is

$$\vec{w}^{k+1} = \arg\min_{\vec{w}} E\left(u^{k+1}, \vec{w}, \vec{b}^k\right) = \gamma \int_\Omega |\vec{w}| dx + \frac{\mu}{2} \int_\Omega \left| \vec{w} - \nabla u^{k+1} - \vec{b}^k \right|^2 dx. \tag{2.65}$$

Here, $\vec{w}$ has closed form solution as a generalized soft thresholding formula

$$\vec{w}^{k+1} = \max\left(\left| \nabla u^{k+1} - \vec{b}^k \right| - \frac{\gamma}{\mu}, 0 \right) \frac{\nabla u^{k+1} - \vec{b}^k}{\left| \nabla u^{k+1} - \vec{b}^k \right|}, 0 \frac{\overrightarrow{0}}{|\overrightarrow{0}|} = \overrightarrow{0}, \tag{2.66}$$

with the discrete formation

$$\vec{w}_{i,j}^{k+1} = \max\left(\left| \nabla^+ u_{i,j}^{k+1} - \vec{b}_{i,j}^k \right| - \frac{\gamma}{\mu}, 0 \right) \frac{\nabla^+ u_{i,j}^{k+1} - \vec{b}_{i,j}^k}{\left| \nabla^+ u_{i,j}^{k+1} - \vec{b}_{i,j}^k \right|}. \tag{2.67}$$

At the end of each iteration, $\vec{b}$ is updated as (2.59)

$$\vec{b}_{i,j}^{k+1} = \vec{b}_{i,j}^k - \left(\vec{w}_{i,j}^{k+1} - \nabla u_{i,j}^{k+1} \right). \tag{2.68}$$

The algorithm for the TV model is summarized in Algorithm 1.

Algorithm 1 The split-Bregman algorithm for the total variation model.

(1) Initialization
setup $u^0 = f, \vec{b}^0 = \overrightarrow{0}, \vec{w}^0 = \overrightarrow{0}, \mu, K, Tol$

(2) Iterations
for k=1 to K
calculate u^{k+1} with (2.64)
calculate $\vec{w}^{k+1}$ with (2.67)
calculate $\vec{b}^{k+1}$ with (2.68)
if $\frac{\left|E\left(u^{k+1}\right)-E\left(u^{k}\right)\right|}{E\left(u^{k}\right)} \leq Tol$, break
endfor

2.6 Summary

Under the variational paradigm, numerous segmentation criteria such as color, texture, shape priors, topology, etc. can be integrated into a model. Even for models purely based on edge and region features, many strategies have been investigated in hopes of speeding up convergence and increasing robustness. In this chapter, only some classical models and their implementations which are closed related to our work are presented.

For numerical optimization methods, we only focused on the split-Bregman algorithm. Other fast algorithms such as the dual method, graph cut methods, multi-grid methods, etc. can also be extended to the problems in the next chapters. However, the split-Bregman algorithm introduced above already provides a general framework for solving different optimization problems. This is sufficient for the works of this thesis.

In the next chapter, we will present an extended Chan-Vese model with novel landmark constraints and devise its numerical solution.

Chapter 3

The Extended Chan-Vese Model with Landmark Constraints

[i] Chapter 2 introduced some representative variational image segmentation models using edge and region features. Among them, the Chan-Vese model [14] stands out as a popular choice due to advantages such as multi-cue integration and adaptive topology. The original Chan-Vese model [14] was proposed as a reduced piecewise constant Mumford-Shah model [27] under the variational level set framework [52]. It is a generic model for two-phase image segmentation using regional image intensities. The model is most suitable for images with noise and weak boundaries, whereas edge-based models based on the geodesic active contours model [9] may be used for images with more complicated interiors and very distinct boundaries. The Chan-Vese model has been extended for a range of image segmentation problems, e.g. the segmentation of color [53], texture [54], noise [55], and motion [56] images. It also serves as the foundation for multi-phase image segmentation models [36].

Much research has been conducted on how to solve the Chan-Vese model efficiently. In order to preserve the signed distance property of the level set function, a computationally intensive re-initialization step is originally required during optimization. In 2005, Li et al. [57] proposed a modified Chan-Vese model without re-initialization

[i] Chapter 3 is a reprint of [51]. Permission has been obtained from Elsevier to include the contents into this thesis.

via the penalty function method. In 2014, Duan et al. [58] proposed some fast algorithms combining a projection scheme with variable splitting methods such as the dual method [59], split-Bregman method [43], and augmented Lagrangian method [44] to achieve higher computation efficiency and accuracy without re-initialization.

The work presented in this chapter extend the Chan-Vese model to the problem of image segmentation with landmarks. Landmarks are pre-defined points that indicate meaningful image features. Explicitly defined feature points have long been used in image analysis, for example, in landmark-based image registration [60]. Inspired by a series of landmarks-based image registration models [61, 62, 63, 64], we consider a new kind of segmentation problem with constraints that induce the contour to pass through some given landmark points. To the best of our knowledge, no variational models under the level set framework has been designed for this task.

In this chapter, we propose a new variational model for image segmentation based on the classical Chan-Vese model (CV) for the problem of segmentation with prior landmarks. The Chan-Vese model with landmarks (CVL) incorporates prior landmarks information as constraints in the optimization problem. We then investigate the solvability of the new model and devise a numerical algorithm based on the split-Bregman algorithm. Some segmentation experiments are conducted on gray value images in comparison with the original CV model to show the benefits of using landmarks.

3.1 The Chan-Vese model

Before presenting the CVL model, we first look at the original CV model and its solution. The CV model [14] and split-Bregman algorithm [43] serve as the foundation for the CVL model and its efficient implementation. In the simplest case, we consider the two-phase segmentation of a gray value image using the variational level set method. For an image $f(x) : \Omega \to R$, $x \in \Omega$, the CV model divides it into two regions Ω_1, Ω_2 with the respective constant image intensities u_1 and u_2. The image $f(x)$ can be approximated as two sections of uniform intensity

$$f(x) = u_1 H(\phi(x)) + u_2(1 - H(\phi(x))), \tag{3.1}$$

where $\phi(x)$ is the signed distance function in (2.10) (2.11) and $H(\phi(x))$ is the Heaviside function (2.12). For ease of computation, $H(\phi(x))$ and $\delta(\phi(x))$ are generally mollified by a small positive constant ε [14], such that

$$H_\varepsilon(\phi(x)) = \frac{1}{2}(1 + \frac{2}{\pi}\arctan(\frac{\phi(x)}{\varepsilon})) \tag{3.2}$$

$$\delta_\varepsilon(\phi) = \frac{\partial H_\varepsilon(\phi)}{\partial \phi} = \frac{1}{\pi}\frac{\varepsilon}{\phi^2 + \varepsilon^2} \tag{3.3}$$

Incorporating the regularization term, the Chan-Vese model for image segmentation can be formulated as the following optimization problem,

$$\begin{aligned} \min_{u_1,u_2,\phi} E(u_1, u_2, \phi) = \quad & \alpha_1 \int_\Omega (f - u_1)^2 H_\varepsilon(\phi) dx + \alpha_2 \int_\Omega (f - u_2)^2 (1 - H_\varepsilon(\phi)) dx \\ & + \gamma \int_\Omega |\nabla H_\varepsilon(\phi)| dx \\ s.t. |\nabla \phi| = 1 & \end{aligned} \tag{3.4}$$

where α_1, α_2 are penalty parameters for the data terms, and γ is a penalty parameter for the regularizer. Note that the last r.h.s. term regularizes the length of the boundary. By using the standard variational method and gradient descent [18], we can obtain the formulas for the estimation of u_1 and u_2 as

$$u_1 = \frac{\int_\Omega f(x) H_\varepsilon(\phi(x)) dx}{\int_\Omega H_\varepsilon(\phi(x)) dx}, \tag{3.5}$$

$$u_2 = \frac{\int_\Omega f(x)(1 - H_\varepsilon(\phi(x))) dx}{\int_\Omega (1 - H_\varepsilon(\phi(x))) dx}, \tag{3.6}$$

and the evolution equation of $\phi(x)$ via gradient descent can be derived as the following dynamic equation

$$\begin{cases} \frac{\partial \phi(x,t)}{\partial t} = (\nabla \cdot (\frac{\nabla \phi(x,t)}{|\nabla \phi(x,t)|}) - Q(x,u_1,u_2))\delta_\varepsilon(\phi(x,t)) & t > 0, x \in \Omega \\ \frac{\partial \phi(x,t)}{\partial \vec{n}} = 0 & t \geq 0, x \in \partial\Omega \\ \phi(x,0) = \phi^0(x) & t = 0, x \in \Omega \cup \partial\Omega \end{cases}, \tag{3.7}$$

where $Q(x,u_1,u_2) = \alpha_1(f(x)-u_1)^2 - \alpha_2(f(x)-u_2)^2$ for simplicity of representation.

In (3.7), we have not yet enforced the constraint $|\nabla\phi(x)| = 1$. Without the constraint, $\phi(x)$ cannot be preserved as a signed distance function. One approach is to solve the static Hamilton-Jacobi equation for the constraint via the upwind difference scheme [33], which is a complicated process. Instead, [14] proposed to solve the following dynamic PDEs built on (3.7),

$$\begin{cases} \frac{\partial \phi(x,t)}{\partial t} + \sin(\psi(x))(|\nabla\phi(x,t)| - 1) = 0 & t > 0, x \in \Omega \\ \frac{\partial \phi(x,t)}{\partial \vec{n}} = 0 & t \geq 0, x \in \partial\Omega \\ \phi(x,0) = \psi(x) & t = 0, x \in \Omega \cup \partial\Omega, \end{cases} \tag{3.8}$$

via the upwind difference scheme. Here, $\psi(x)$ denotes the $\phi(x)$ obtained from (3.7). The new dynamic equations now maintain the constraint in each iteration. However, the computation can still be simplified further. Solving (3.7) involves the discretization of curvature while solving (3.8) calls for specifically the upwind difference scheme. In [57], the constraint is represented as a penalty term in the energy functional instead. In this work, we choose to use the split-Bregman algorithm [43] with a simple projection scheme [65].

3.2 The split-Bregman algorithm for the Chan-Vese model

To address the computational problems arising out of the Chan-Vese model, Duan et al. [58] designed some fast algorithms based on alternating direction minimization

techniques. In these algorithms, a projection scheme is implemented per iteration in place of the complex computation of the Eikonal equation (2.11). The split-Bregman projection method for the Chan-Vese model as presented in [58] can be represented as,

$$\begin{cases} (u_1^{k+1}, u_2^{k+1}, \phi^{k+1}, \vec{w}^{k+1}) = \\ \quad \underset{u_1,u_2,\phi,\vec{w}:|\vec{w}|=1}{\arg\min} \left\{ \begin{aligned} E(u_1,u_2,\phi,\vec{w}) =& \alpha_1 \int_\Omega (f-u_1)^2 H_\varepsilon(\phi) dx \\ &+ \alpha_2 \int_\Omega (f-u_2)^2 (1-H_\varepsilon(\phi)) dx \\ &+ \gamma \int_\Omega |\vec{w}| \delta_\varepsilon(\phi) dx + \frac{\theta}{2} \int_\Omega |\vec{w} - \nabla\phi - \vec{b}^k|^2 dx \end{aligned} \right\} \\ \vec{b}^{k+1} = \vec{b}^k + \nabla\phi^{k+1} - \vec{w}^{k+1} \\ \vec{b}^0 = 0, \vec{w}^0 = \nabla\phi^0, \end{cases} \tag{3.9}$$

where, $\vec{w}$ is an auxiliary variable to approximate $\nabla\phi$ and $\vec{b}$ is the Bregman iterative parameter. In each iteration, the minimization problem can be decomposed into the following three sub-problems,

$$(u_1^{k+1}, u_2^{k+1}) = \underset{u_1,u_2}{\arg\min}\, E(u_1, u_2, \phi^k, \vec{w}^k), \tag{3.10}$$

$$\phi^{k+1} = \underset{\phi}{\arg\min}\, E(u_1^{k+1}, u_2^{k+1}, \phi, \vec{w}^k), \tag{3.11}$$

$$\vec{w}^{k+1} = \underset{\vec{w}:|\vec{w}|=1}{\arg\min}\, E(u_1^{k+1}, u_2^{k+1}, \phi^{k+1}, \vec{w}). \tag{3.12}$$

Using standard variational methods [18], their solutions can be obtained respectively as

$$u_1^{k+1} = \frac{\int_\Omega f H_\varepsilon(\phi^k(x)) dx}{\int_\Omega H_\varepsilon(\phi^k(x)) dx}\ , \tag{3.13}$$

$$u_2^{k+1} = \frac{\int_\Omega f(1 - H_\varepsilon(\phi^k(x))dx}{\int_\Omega (1 - H_\varepsilon(\phi^k(x))dx} \ , \tag{3.14}$$

$$\begin{cases} Q(u_2^{k+1}, u_2^{k+1})\delta_\varepsilon(\phi(x)) + \gamma|\vec{w}^k(x)|\frac{\partial \delta_\varepsilon(\phi(x))}{\partial \phi(x)} & x \in \Omega \\ -\theta(\Delta\phi(x) - \nabla \cdot \vec{w}^k(x) + \nabla \cdot \vec{b}^k(x)) = 0 & \\ (\vec{w}^k(x) - \nabla\phi(x) - \vec{b}^k(x)) \cdot \vec{n} = 0 & x \in \partial\Omega \\ \phi^{k+1,0}(x) = \phi^k(x) & x \in \Omega \cup \partial\Omega \ , \end{cases} \tag{3.15}$$

$$\begin{cases} \vec{w}^{k+1}(x) = \max(|\nabla\phi^{k+1}(x) + \vec{b}^k(x)| - \frac{\gamma}{\theta}\delta_\varepsilon(\phi^{k+1}(x)), 0)\frac{\nabla\phi^{k+1}(x) + \vec{b}^k(x)}{|\nabla\phi^{k+1}(x) + \vec{b}^k(x)|_\varepsilon} \\ \vec{w}^{k+1}(x) = \frac{\vec{w}^{k+1}(x)}{\max(1, |\vec{w}^{k+1}(x)|_\varepsilon)} \ , \end{cases} \tag{3.16}$$

where (3.15) is a typical Euler-Lagrange equation free of curvature calculations, and (3.16) is a generalized soft thresholding formula in analytical form. The projection step in (3.16) circumvents the costly re-initialization otherwise required for the constraint. With the help of auxiliary variables and the projection method, the computation of the Chan-Vese model is now much simplified. To solve (3.15), we derive its gradient descent equation and use the first-order finite difference scheme temporally and spatially to obtain the Gauss-Seidel iterative scheme for $\phi_{i,j}^{k+1}$, such that

$$\phi_{i,j}^{k+1,s+1} = \frac{\begin{pmatrix} \phi_{i,j}^{k+1,s} - tQ(u_1^{k+1}, u_2^{k+1})\delta_\varepsilon(\phi_{i,j}^{k+1,s}) \\ - t\gamma|\vec{w}_{i,j}^k|\dfrac{\partial\delta_\varepsilon(\phi_{i,j}^{k+1,s})}{\partial\phi} + t\theta(\nabla \cdot \vec{b}_{i,j}^k - \nabla \cdot \vec{w}_{i,j}^k) \\ + t\theta(\phi_{i-1,j}^{k+1,s+1} + \phi_{i,j-1}^{k+1,s+1} + \phi_{i+1,j}^{k+1,s} + \phi_{i,j+1}^{k+1,s}) \end{pmatrix}}{(1 + 4t\theta)}, \phi_{i,j}^{k+1,0} = \phi_{i,j}^k, \tag{3.17}$$

until $\frac{|E^{k+1,s+1} - E^{k+1,s}|}{E^{k+1,s}} \leq Tol$. Here, t is the time step, the spatial step is 1, Tol is the error tolerance, and $E^{k+1,s} = E(u_1^{k+1}, u_2^{k+1}, \phi^{k+1,s}, \vec{w}^k)$.

Given that (3.9) is a typical local minimization problem, it follows that the final

solution depends on the initialization conditions $\phi^0(x)$, the initial level set. By introducing landmark constraints as proposed below, we can guide the segmentation contour to more meaningful locations despite poor contour initialization.

3.3 The Chan-Vese model with landmark constraints

To ensure that the segmentation contour passes through the given landmarks, we introduce a new constraint term to the original CV model. Let the landmark points be $\boldsymbol{x_L} = \{x_1, x_2, \ldots, x_L\}$, we can define a mask function for the points as

$$\eta(x) = \begin{cases} 1 & if\ x \in \boldsymbol{x_L} \\ 0 & otherwise. \end{cases} \tag{3.18}$$

Since the segmentation contour is the zero level set, to guarantee the landmark points to be on the contour, we should enforce that

$$\phi(x) = 0,\ if\ x \in \boldsymbol{x_L}. \tag{3.19}$$

The problem then becomes

$$\begin{aligned} \min_{u_1,u_2,\phi} E(u_1, u_2, \phi) \quad & = \alpha_1 \int_\Omega (f - u_1)^2 H_\varepsilon(\phi) dx + \alpha_2 \int_\Omega (f - u_2)^2 (1 - H_\varepsilon(\phi)) dx \\ & + \gamma \int_\Omega |\nabla H_\varepsilon(\phi)| dx \\ s.t. \phi(x) = 0,\ if\ x \in \boldsymbol{x_L} & \\ |\nabla \phi| = 1 & \end{aligned} \tag{3.20}$$

To incorporate the landmark constraints, we can frame them as an additional penalty term regulated by the parameter $\mu > 0$. The problem becomes

$$\begin{aligned}\min_{u_1,u_2,\phi} E(u_1,u_2,\phi) = \quad & \alpha_1 \int_\Omega (f-u_1)^2 H_\varepsilon(\phi) dx + \alpha_2 \int_\Omega (f-u_2)^2 (1-H_\varepsilon(\phi)) dx \\ & + \gamma \int_\Omega |\nabla H_\varepsilon(\phi)| dx + \frac{\mu}{2} \int_\Omega \eta(x)\phi^2 dx \qquad , \\ s.t. & |\nabla \phi| = 1\end{aligned} \tag{3.21}$$

where $\eta(x)$ is defined in (3.18).

Here we briefly show that the new functional optimization problem (3.21) is equivalent to (3.20). For $\mu > 0$, we can suppose that $(u_1(\mu), u_2(\mu), \phi(\mu))$ is the unique solution to the problem (3.19). For (3.21) we can use the split-Bregman approach to obtain a sequence to approximate its solution, as detailed in the next section. By Theorem 17.1 in [66], every limit point (u_1^*, u_2^*, ϕ^*) of the obtained sequence $\{(u_1(\mu^k), u_2(\mu^k), \phi(\mu^k)), k = 0, 1, 2, \dots\}$ will be the solution of (3.20). Therefore, a solution of problem (3.20) can be obtained by solving (3.21) for a large positive number $\mu > 0$.

During iteration, the landmark constraints will cause the segmentation contour to shift towards the landmarks. Since $\phi(x)$ is maintained as a signed distance function, the value of $\phi(x)$ is the distance to the segmentation contour. Therefore, setting $\phi(x)$ to 0 for a landmark point entails that, relative to the landmark, $\phi(x) > 0$ for points closer to the contour and $\phi(x) < 0$ for points farther away. This eventually causes the landmarks to connect to the contour.

The convergence of the model can be shown by analyzing the evolution equation of $\phi(x,t)$ via gradient descent method,

$$\frac{\partial \phi(x,t)}{\partial t} = (\nabla \cdot (\frac{\nabla \phi(x,t)}{|\nabla \phi(x,t)|}) - Q(x,u_1,u_2))\delta_\varepsilon(\phi(x,t)) - \mu\eta(x)\phi(x,t). \tag{3.22}$$

At normal points where $\mu\eta(x)\phi(x,t) = 0$, the evolution equation is

$$\frac{\partial \phi(x,t)}{\partial t} = (\nabla \cdot (\frac{\nabla \phi(x,t)}{|\nabla \phi(x,t)|}) - Q(x,u_1,u_2))\delta_\varepsilon(\phi(x,t)), \tag{3.23}$$

which is the same as the equation for the original CV model. At the landmark points, $\mu\eta(x)\phi(x,t) \neq 0$, and the following equation holds

$$\frac{\partial\phi(x,t)}{\partial t} = \nabla \cdot (\frac{\nabla\phi(x,t)}{|\nabla\phi(x,t)|})\delta_\varepsilon(\phi(x,t)) - \mu\eta(x)\phi(x,t). \tag{3.24}$$

If $\phi(x,t) > 0$, the penalty term will cause $\phi(x,t)$ to decrease, and if $\phi(x,t) < 0$, the penalty term will cause $\phi(x,t)$ to increase. At points where $\eta(x) = 0$, a more simplified evolution equation applies such that

$$\frac{\partial\phi(x,t)}{\partial t} = \nabla \cdot (\frac{\nabla\phi(x,t)}{|\nabla\phi(x,t)|})\delta_\varepsilon(\phi(x,t)). \tag{3.25}$$

The above is a typical curve interpolation equation of an implicit level set function via curvature diffusion. Therefore, the additional constraint term does not affect the convergence of the model as compared to the original CV. Having proven that the new model (3.21) converges, we will now develop an algorithm to solve it iteratively.

3.4 The split-Bregman algorithm for the Chan-Vese model with landmark constraints

To use the split-Bregman algorithm for the CVL model, we introduce an auxiliary variable $\vec{w}(x) = \nabla\phi(x)$ and the Bregman iterative parameter $\vec{b}(x)$. (3.21) can be turned into the following alternating iterative minimization problem

$$\begin{cases} (u_1^{k+1}, u_2^{k+1}, \phi^{k+1}, \vec{w}^{k+1}) = \\ \quad \underset{u_1,u_2,\phi,w:|\vec{w}|=1}{\arg\min} \left\{ \begin{aligned} E(u_1,u_2,\phi,\vec{w}) =& \alpha_1 \int_\Omega (f-u_1)^2 H_\varepsilon(\phi) dx \\ &+ \alpha_2 \int_\Omega (f-u_2)^2 (1-H_\varepsilon(\phi)) dx \\ &+ \gamma \int_\Omega |\vec{w}| \delta_\varepsilon(\phi) dx + \frac{\mu}{2} \int_\Omega \eta(x) \phi^2 dx \\ &+ \frac{\theta}{2} \int_\Omega |\vec{w} - \nabla\phi - \vec{b}^k|^2 dx \end{aligned} \right\} \\ \vec{b}^{k+1} = \vec{b}^k + \nabla\phi^{k+1} - \vec{w}^{k+1} \\ \vec{b}^0 = 0, \vec{w}^0 = \nabla\phi^0 \end{cases} . \quad (3.26)$$

In each iteration, we will solve three smaller sub-problems,

$$(u_1^{k+1}, u_2^{k+1}) = \underset{u_1,u_2}{\arg\min}\, E(u_1, u_2, \phi^k, \vec{w}^k), \quad (3.27)$$

$$\phi^{k+1} = \underset{\phi}{\arg\min}\, E(u_1^{k+1}, u_2^{k+1}, \phi, \vec{w}^k), \quad (3.28)$$

$$\vec{w}^{k+1} = \underset{\vec{w}:|\vec{w}|=1}{\arg\min}\, E(u_1^{k+1}, u_2^{k+1}, \phi^{k+1}, \vec{w}). \quad (3.29)$$

The solutions to (3.27), (3.29) remain the same as (3.13), (3.14), and (3.16), but the evolution equation of $\phi(x,t)$ becomes

$$\begin{cases} \frac{\partial\phi}{\partial t} = -Q(u_2^{k+1}, u_2^{k+1})\delta_\varepsilon(\phi) - \gamma|\vec{w}^k(x)| \frac{\partial\delta_\varepsilon(\phi)}{\partial\phi} - \mu\eta(x)\phi & t > 0, x \in \Omega \\ +\theta(\Delta\phi - \nabla\cdot\vec{w}^k + \nabla\cdot\vec{b}^k) & \\ (\vec{w}^k - \nabla\phi - \vec{b}^k)\cdot\vec{n} = 0 & t \geq 0, x \in \partial\Omega \\ \phi^{k+1,0} = \phi^k & t = 0, x \in \Omega \cup \partial\Omega. \end{cases} \quad (3.30)$$

The new Gauss-Seidel iterative scheme for $\phi_{i,j}^{k+1}$ can be derived as

$$\phi_{i,j}^{k+1,s+1} = \frac{\begin{pmatrix} \phi_{i,j}^{k+1,s} - tQ(u_1^{k+1}, u_2^{k+1})\delta_\varepsilon(\phi_{i,j}^{k+1,s}) \\ - t\gamma|\vec{w}_{i,j}^{k}|\dfrac{\partial\delta_\varepsilon(\phi_{i,j}^{k+1,s})}{\partial\phi} + t\theta(\nabla\cdot\vec{b}_{i,j}^{k} - \nabla\cdot\vec{w}_{i,j}^{k}) \\ + t\theta(\phi_{i-1,j}^{k+1,s} + \phi_{i,j-1}^{k+1,s} + \phi_{i+1,j}^{k+1,s} + \phi_{i,j+1}^{k+1,s}) \end{pmatrix}}{(1 + t\mu\eta_{i,j} + 4t\theta)}, \phi_{i,j}^{k+1,0} = \phi_{i,j}^{k}, \quad (3.31)$$

until $\frac{|E^{k+1,s+1} - E^{k+1,s}|}{E^{k+1,s}} \leq Tol$. Here Tol is the error tolerance, t is the time step, the spatial step is 1, and $E^{k+1,s} = E(u_1^{k+1}, u_2^{k+1}, \phi^{k+1,s}, \vec{w}^k)$.

It is not hard to tell by comparing (3.17) and (3.31) that the complexity of solving the original CV model and the CVL model are the same. The split-Bregman algorithm for the CVL can be summarized as Algorithm 2.

Algorithm 2 The split-Bregman algorithm for the Chan-Vese model with landmark constraints.

(1) Initialization
setup penalty parameter $\alpha_1, \alpha_2, \theta, \mu$
setup iteration number K and tolerance Tol
setup timestep t
setup $\vec{b}^0 = \vec{0}$
read image f, initialize level set function ϕ^0
calculate $\vec{w}^0 = \nabla\phi^0$

(2) Iterations
for k=1 to K
calculate u_1^{k+1}, u_2^{k+1} by (3.13),(3.14)
calculate ϕ^{k+1} by (3.31)
calculate $\vec{w}^{k+1}$ by (3.16)
calculate $\vec{b}^{k+1}$ according to (3.26)
if $\frac{|E^{k+1} - E^{k+1}|}{E^{k+1}} \leq Tol$, break
endfor

Compared to the algorithm for the CV model, Algorithm 2 differs only in the iterative calculation of ϕ which has no impact on the convergence properties. The new penalty parameter μ balances the landmark constraints with the data terms to produce optimal results.

To summarize, we have proposed a new model based on the classical Chan-Vese

model that performs image segmentation based on the pre-existing landmarks and image data. The new model solves for contours passing through given points in a computationally efficient way without compromising the convergence of the algorithm. With explicit information guiding the evolution of contour, the segmentation result can now depend less on the choice of the initial contour. Furthermore, the contour is more accurate in the regions marked by landmarks. The experiments below illustrate these advantages.

3.5 Experimental results

To show the performance of the new model with landmark constraints, we present some segmentation experiments on gray value two-phase synthetic images, a synthetic noisy image, and a real-world ultrasound image. The results are compared with those obtained from the CV model to show the advantages of using landmarks. For the experiments below, all initial contours and landmarks are selected by hand, though they may also be generated automatically. The running environment is a PC (Intel (R) Core (TM) i7-7700 CPU @ 3.60GHz 3.60 GHz; memory: 16.0 GB; code running environment: Matlab R2017a).

In the following experiments, α_1 and α_2 are set to 1, and t is 0.1 throughout for easy tuning. In both the CV and the CVL model, γ and θ are increased for noisy images in order to subdue the data terms, subsequently reducing the effect of noise in the data terms. To emphasize the importance of the landmark constraints, both μ and θ are set higher to increase the weight of the landmark term while suppressing the data terms. Finally, the threshold value Tol is set so that convergence is reached after the contour becomes stable.

One advantage of using landmarks is the lowered dependence of the segmentation result on the choice of the initial level set and the penalty parameters. Since the CVL model is a local minimization scheme, different setups of the initial contour may converge to different energy minima. It is sometimes difficult to select the optimal initialization for the CV model without resorting to a trial and error approach based

on perceived results. However, with some given landmarks as guidance, bad initialization can now converge to better contours without excessive tuning. This effect is shown in Fig. 3-1 and 3-2. It is also worth noting that with some automated landmark detection methods, using the CVL can make the segmentation pipeline more automatic.

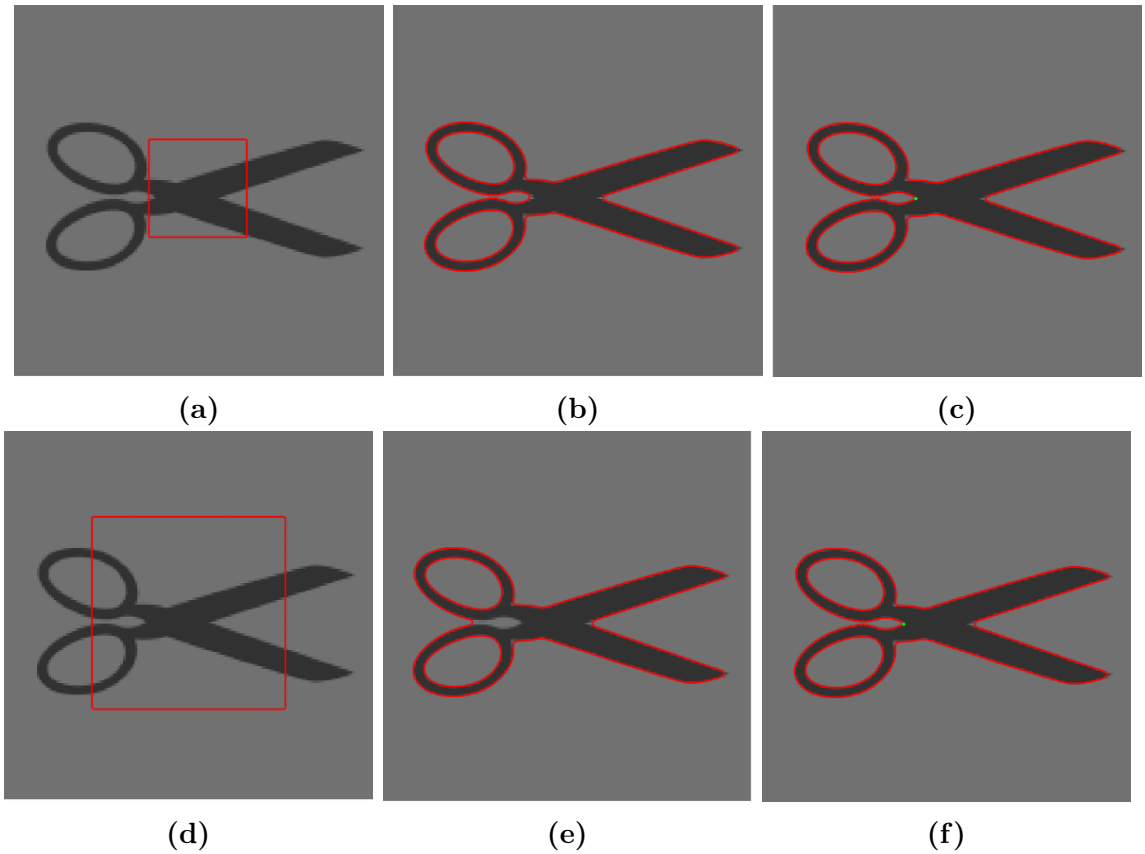

Fig. 3-1: Synthetic image of scissors. (a-c) and (d-f) use two different initial contours. (c, f) each uses one landmark while (b, e) do not use landmarks. The second initial contour led to under-segmentation shown in (e), which was fixed by a landmark as shown in (f). In both experiments, $\alpha_1 = 1$, $\alpha_2 = 1$, $\gamma = 1$, $\varepsilon = 3$, $\theta = 20$, $t = .1$, $Tol = 10^{-6}$. In (c, f), $\mu = 5$.

In Fig. 3-1, the second initial contour failed to evolve into the cusp region in the scissors using the CV model. The object was under-segmented as a result. However, using the same parameters in CVL along with one landmark corrected the error. This experiment shows that using landmarks via the CVL can mitigate inaccuracies caused by bad initial contour selection.

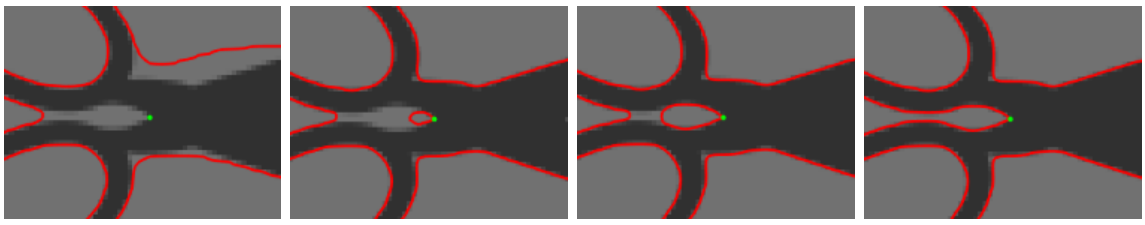

(a) (b) (c) (d)

Fig. 3-2: Synthetic image of scissors, close-up. (a-d) show the evolution of the segmentation contour in the first 25 iterations, in chronological order.

A closer look at the beginning of the contour evolution via the CVL in Fig. 3-2 shows a section of contour originating from the landmark, later merging with the main contour. This shows that the landmark constraint pushes the level set function out of an undesirable local energy minimum.

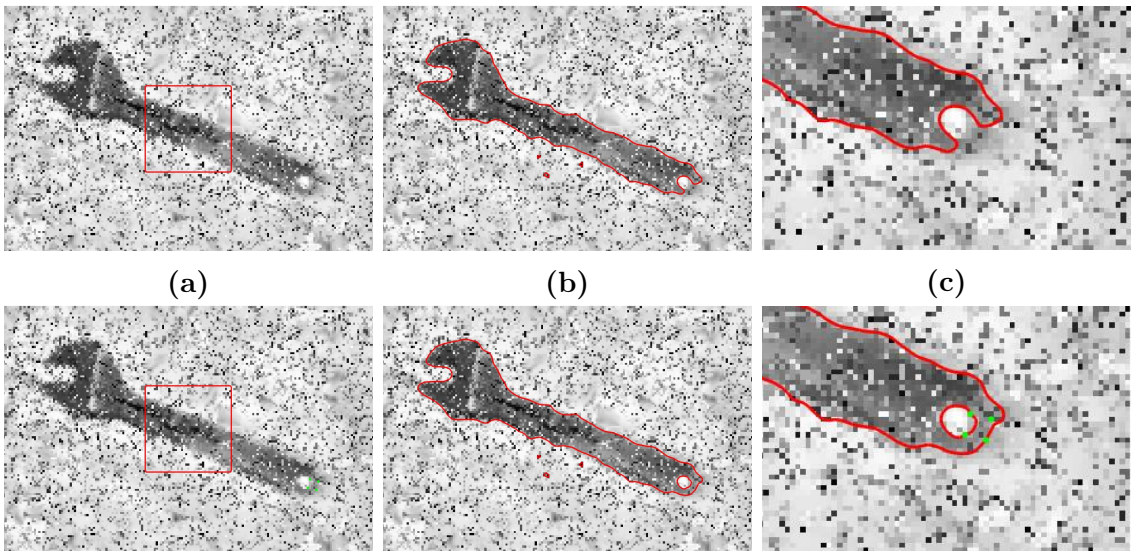

(a) (b) (c)

(d) (e) (f)

Fig. 3-3: An image of a wrench with synthetic salt and pepper noise. (a-c) show segmentation without landmarks, (d-f) show segmentation via CVL with four landmarks, and (c, f) are close-ups of the critical region. In both rows, $\alpha_1 = 1$, $\alpha_2 = 1$, $\gamma = 500$, $\varepsilon = 3$, $\theta = 500$, $t = .1$, $Tol = 10^{-6}$. In the second row, $\mu = 20$.

The same correctional effect can be seen in noisy images, as shown in Fig. 3-3. In Fig. 3-3 (c), the segmentation error was not due to initialization, but rather to the noise present. Though better results may be generated with further parameter tuning, the process may involve excessive human interference and sacrificing the robustness

of the algorithm. The CVL is able to correct contour in the critical region with four landmarks, as shown in Fig. 3-3 (d-f).

Placing landmarks over important image features also improves the segmentation accuracy around those points. For image features that are indistinct or poorly segmented, we can use landmarks to define and improve them. For instance, we can produce sharper corners in the contour by detecting the corner points and placing them as landmarks, as demonstrated in Fig. 3-4 and 3-5. Particularly with the CV model, the corners of the contour are often rounded due to the regularization term which minimizes the length of the contour. Instead of re-tuning the penalty parameters, we can use the landmark constraints to improve the contour description in specific regions. This is particularly useful for segmentation of critical regions that demand high accuracy, such as in medical imagery. Another example is establishing the eye corners in eye shape segmentation, which will likely improve the contours of the eyes significantly.

Although the CVL model can reduce the effect of initialization and increase segmentation accuracy, it is not without limitations. As shown in Fig. 3-6, the effect of one landmark is insufficient to inpaint large sections of illusory contours. The landmark point failed to connect to the contour due to the long distance between them. Upon increasing the weight of the landmark constraint, the landmark connected again, albeit at the expense of segmentation accuracy due to the data and regularization terms losing effect. In this case, it appears that forcefully connecting the landmark point through parameter manipulation is impractical. However, when we increased the number of landmark points in Fig. 3-6 (d), the landmarks connected more naturally again. The ideal solution is to introduce an extra elastica term into the CVL model. The work is presented in the next chapter.

The segmentation problem with landmarks becomes illusory contour inpainting when landmarks are placed too far from the object boundary. This can be detected during contour evolution when the values $\phi(x,t)$ for all points adjacent to a landmark remain above or below 0 for a long time, indicating that the contour failed to pass through the said landmark. When an isolated landmark is detected, we can either

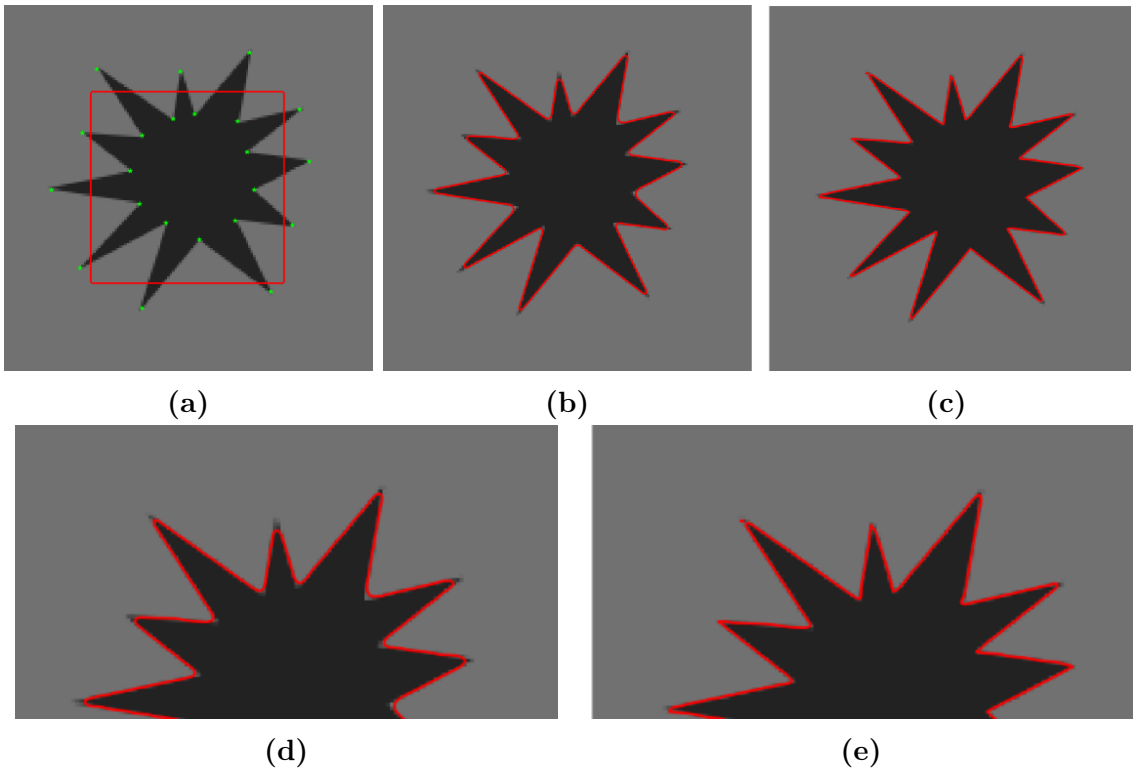

Fig. 3-4: A star shape. (a) is the original image with initial contour and landmarks, (b) is the segmentation result without landmarks, and (c) is the result using CVL. (d, e) are close-ups of (b, c) respectively. In (a-e), $\alpha_1 = 1$, $\alpha_2 = 1$, $\gamma = 1$, $\varepsilon = 3$, $\theta = 20$, $t = .1$, $Tol = 10^{-6}$. In (c, e), $\mu = 300$.

Fig. 3-5: An ultrasound image. (b) is the segmentation result without landmarks, and (c) is the result using CVL and three landmarks. In (b,c), $\alpha_1 = 1$, $\alpha_2 = 1$, $\gamma = 500$, $\varepsilon = 3$, $\theta = 500$, $t = .1$, $Tol = 10^{-6}$. In (c), $\mu = 500$.

abort the segmentation or remove the isolated point from the set of landmarks $\boldsymbol{x_L}$. Alternatively, we can use more landmark points in the critical regions. For example in [49], the landmarks detected initially are clusters rather than points. Methods

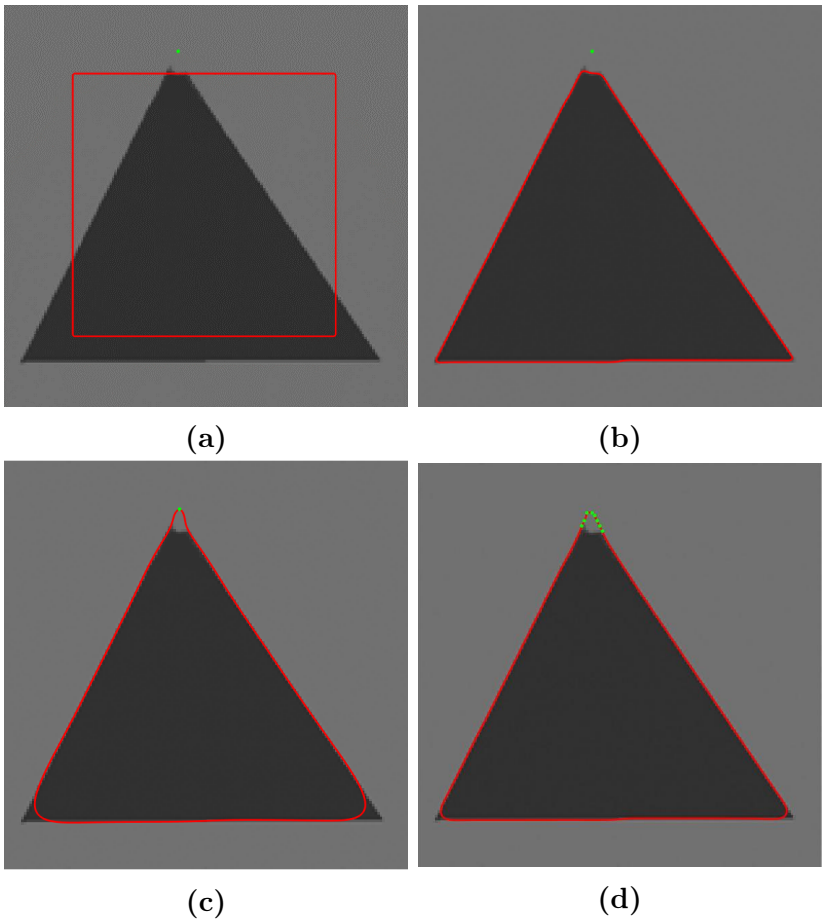

Fig. 3-6: A clipped triangle. (b) is the segmentation result without using landmarks, (c) is the result using CVL and one landmark, and (d) is the result using CVL with multiple landmarks and more relaxed constraints. In (b-d), $\alpha_1 = 1$, $\alpha_2 = 1$, $\gamma = 1$, $\varepsilon = 3$, $t = .1$. In (b), $\theta = 20$, $\mu = 0$, $\zeta = 10^{-6}$. In (c), $\theta = 5 * 10^5$, $\mu = 5 * 10^5$, $\zeta = 10^{-8}$. In (d), $\theta = 4 * 10^3$, $\mu = 4 * 10^3$, $Tol = 10^{-6}$.

that detect a larger number of landmark points can be used alongside of the CVL to provide the model with more guidance.

3.6 Summary

In this chapter, a modified Chan-Vese model that incorporates landmark information as constraints was introduced. The numerical solution for the new model with the split-Bregman method and the projection method was devised. The mathematical properties of the solution were analyzed and the convergence of the new model was proven. Experiments show that the CVL model can effectively use landmarks to counter bad initialization, refine segmentation contours, as well as define critical regions in more detail.

One shortcoming of the proposed model is that it cannot handle contour inpainting problems. This issue is addressed in the next chapter by incorporating the elastica term. Another point worth mentioning is that the Chan-Vese model is a relatively simple model designed for region-based two-phase image segmentation. In case of non-uniform object interiors or other complications, we may choose alternative variational models such as multi-phase models or contour-based models [13, 9] over the Chan-Vese model. For future works, the proposed landmark constraints can be incorporated into other models as well. Additionally, deep learning models can be used to automatically generate landmarks such as in [49].

Chapter 4

The Extended Chan-Vese Model with Landmark Constraints and Elastica

[i]In the previous chapter, the CVL model was proposed for landmark-guided image segmentation. The model can circumvent the effect of bad initialization as well as improve the segmentation accuracy in critical regions. However, since the CVL model contains the total variation of the Heaviside function, the length of the contour is regularized and formation of large sections of illusory contours is generally discouraged. As a results, landmark points may fail to connect to the segmentation contour when they are too far away. To address this issue, we propose the Chan-Vese model with landmark constraints and elastica.

The elastica regularizers proposed in the 1990s in depth segmentation [68] have proved successful in many image processing problems, such as the inpainting of larger broken images [69], restoration of images with smooth components [70, 71], and image segmentation with larger damaged areas or occlusions [72, 73, 74]. In [72], Zhu et al. propose a modified Chan-Vese model with elastica (CVE), combining the classic CV model and the elastica regularizer to interpolate segmentation curves. Since the curve interpolation relied purely on the penalty parameters, however, it was difficult for the

[i]Chapter 4 only contains the parts of [67] that the author contributed to, as well as novel works by the author that are currently unpublished. Permission has been obtained from all co-authors to include the section of work from [67] contained in this chapter. The same contents will not be used in any other thesis.

inpainted curve to pass through desired regions. This control can be achieved with guidance from landmarks. Here, we propose the Chan-Vese model with landmark constraints and elastica (CVLE). Different from [72] which uses a piecewise constant binary label function, the CVLE models the evolution of the contour which makes use of geometric quantities such as the gradient exactly. Therefore, it uses a Lipschitz smooth level set function defined as a signed distance function, same as the CVL. Again, to solve the new model, we use the split-Bregman method [43] to divide the original problem into simpler sub-problems and optimize them separately and alternatingly. The sub-problems can be solved with the Gauss-Seidel iterative scheme and generalized soft thresholding formula with projection method [58].

In this chapter, we first introduce the Euler's elastica and the Chan-Vese model with elastica. Next, we propose the Chan-Vese model with landmark constraints and elastica. The numerical algorithm is then devised using the split-Bregman method and a projection scheme. Finally, we show the performance of the CVLE model in contour inpainting problems and compare its performance with the CVL.

4.1 The Chan-Vese model with elastica

The Euler's elastica [75] is a functional proposed by Leohnard Euler in 1744 to model deflections in an elastic rod. The form of the functional is

$$E = \int_C (a + bk^2) ds, \tag{4.1}$$

where C is the length of the rod, ds is the differential element along the rod, and a, b are parameters.

In 1990s, [76] extended the classical Mumford-Shah model [27] to address the problems of depth image segmentation and illusory contour inpainting and proposed the Nitzberg, Mumford and Shiota (NMS) model,

$$\min_{C,u} E(C,u) = \alpha \int_\Omega (u-f)^2 dx + \beta \int_{\Omega/C} |\nabla u|^2 dx + \int_C (a + bk^2) ds. \tag{4.2}$$

The model is designed based on the continuation principle of Kanisza where the minimum curvature hypothetically leads to good curve interpolations. Drawing from the same idea, [69] combined the classical total variation model [50] with the Euler's elastica to inpaint images with large areas of damage, proposing the second order model below

$$\min_u E(u) = \int_{\Omega/D} (u-f)^2 dx + \int_D (a + b(\nabla \cdot (\frac{\nabla u}{|\nabla u|}))^2) dx, \tag{4.3}$$

where D is the damaged area.

Under the variational level set framework, [73, 74, 77] are some examples of inpainting or interpolation of illusory contours using the Euler's elastica. Notably, [72] proposed the Chan-Vese model with elastica (CVE) below

$$\begin{aligned} \min_{u_1,u_2,\phi} E(u_1,u_2,\phi) = \alpha_1 \int_\Omega (f-u_1)^2 H(\phi) dx + \alpha_2 \int_\Omega (f-u_2)^2 (1-H(\phi)) dx \\ + \int_\Omega (a + b(\nabla \cdot (\frac{\nabla H(\phi)}{|\nabla H(\phi)|}))^2 |\nabla H(\phi)| dx \end{aligned} \tag{4.4}$$

where ϕ is the signed distance function (2.10) and $H(\phi)$ is the Heaviside function (2.12). Since $H(\phi)$ is a binary function and $\nabla \cdot (\frac{\nabla \phi \delta(\phi)}{|\nabla \phi| \delta(\phi)}) = \nabla \cdot (\frac{\nabla \phi}{|\nabla \phi|}) = k$, [72] simplified (4.4) as

$$\begin{aligned} \min_{u_1,u_2,\phi} E(u_1,u_2,\phi) = \alpha_1 \int_\Omega (f-u_1)^2 \phi dx + \alpha_2 \int_\Omega (f-u_2)^2 (1-\phi) dx \\ + \int_\Omega (a + bk^2) |\nabla \phi| dx, \end{aligned} \tag{4.5}$$

with the additional constraint $\phi \in [0,1]$.

4.2 The Chan-Vese model with landmark constraints and elastica

Combining the CVL proposed in chapter 3 (3.21) and the CVE (4.4), we propose the CVLE,

$$\begin{aligned}\min_{u_1,u_2,\phi} E(u_1,u_2,\phi) = \quad & \alpha_1 \int_\Omega (f-u_1)^2 H_\varepsilon(\phi)dx + \alpha_2 \int_\Omega (f-u_2)^2(1-H_\varepsilon(\phi))dx \\ & + \frac{\mu}{2}\int_\Omega \eta(x)\phi^2 dx \\ & + \gamma \int_\Omega (a + b(\nabla\cdot(\frac{\nabla\phi}{|\nabla\phi|}))^2)|\nabla H_\varepsilon(\phi)|dx \\ s.t.\ |\nabla\phi| = 1 & \end{aligned}, \quad (4.6)$$

where η is the mask function (3.18). With the landmark constraints as guidance and the elastica term to facilitate contour interpolation, the CVLE can now tackle illusory contour inpainting problems. However, the curvature term still causes complications in the optimization. We will use the split-Bregman method to circumvent the calculation of curvature.

4.3 The split-Bregman algorithm for the Chan-Vese model with landmark constraints and elastica

To simplify the implementation of the CVLE model, we introduce auxiliary variables $\vec{p}, \vec{m}, \vec{n}, q$, where

$$\vec{p} = \nabla\phi, \quad (4.7)$$

$$\vec{m} = \frac{\vec{p}}{|\vec{p}|}, \quad (4.8)$$

$$q = \nabla\cdot\vec{n}. \quad (4.9)$$

Considering that $|\vec{m} \leq 1|$, (4.8) can be replaced by a more relaxed set of con-

straints, $|\vec{p}| - \vec{p} \cdot \vec{m} \geq 0$ and $|\vec{m} \leq 1|$ [27]. Since $\vec{p} = \nabla\phi$, the Eikonal equation $|\nabla\phi| = 1$ can be rewritten as $|\vec{p}| = 1$. Additionally, we can introduce a variable $\vec{n} = \vec{m}$ [27] for further splitting. Finally, the constraints (4.7), (4.8), (4.9) become

$$\vec{p} = \nabla\phi, \tag{4.10}$$

$$|\vec{p}| - \vec{p}\vec{m} = 0, |\vec{p}| = 1, \tag{4.11}$$

$$\vec{n} = \vec{m}, |\vec{m}| \leq 1, \tag{4.12}$$

$$q = \nabla \cdot \vec{n}. \tag{4.13}$$

Next, to design the split-Bregman algorithm for the problem, we introduce the Bregman iterators $b_1, \vec{b_2}, \vec{b_3}, b_4$ and the penalty parameters $\gamma_1, \gamma_2, \gamma_3, \gamma_4$ and reformulate (4.6) as the following

$$\begin{aligned} E\left(u_1, u_2, \phi, \vec{p}, \vec{n}, \vec{m}\right) = & \int_\Omega Q\left(x, u_1, u_2\right) H\left(\phi\right) dx \\ & + \gamma \int_\Omega \left(a + bq^2\right) |\vec{p}| \delta_\varepsilon\left(\phi\right) dx + \frac{\mu}{2} \int_\Omega \eta\phi^2 dx \\ & + \int_\Omega \lambda_1 \left(|\vec{p}| - \vec{p} \cdot \vec{m}\right) dx + \gamma_1 \int_\Omega \left(|\vec{p}| - \vec{p} \cdot \vec{m}\right) dx \\ & + \frac{\gamma_2}{2} \int_\Omega \left|\vec{p} - \nabla\phi - \vec{b}_2^k\right|^2 dx \\ & + \frac{\gamma_3}{2} \int_\Omega \left|\vec{n} - \vec{m} - \vec{b}_3^k\right|^2 dx \\ & + \frac{\gamma_4}{2} \int_\Omega \left(q - \nabla \cdot \vec{n} - b_4^k\right)^2 dx + \delta_R(\vec{m}) \end{aligned}, \tag{4.14}$$

where $Q(u_1, u_2) = \alpha_1(f(x) - u_1)^2 - \alpha_2(f(x) - u_2)^2$ for simplicity, $|\vec{p}| = 1$ and $\delta_{\mathcal{R}}(\vec{m})$ is the characteristic function on the convex set $\mathcal{R} = \{m \in L^2\left(\Omega\right) : |m| \leq 1\text{a.e. in } \Omega\}$, given by

$$\delta_{\mathcal{R}}(\vec{m}) = \begin{cases} 0 & \text{if } \vec{m} \in \mathcal{R} \\ +\infty & \text{otherwise} \end{cases}. \tag{4.15}$$

The Bregman iterators are updated per iteration $k = 0, 1, 2...K$ as

$$\begin{cases} \lambda_1^{(k+1)} = \lambda_1^k + \gamma_1 \left(\left| \vec{p}^{k+1} \right| - \vec{p}^{k+1} \cdot \vec{m}^{k+1} \right) \\ \vec{b}_2^{k+1} = \vec{b}_2^k + \nabla \phi^{k+1} - \vec{p}^{k+1} \\ \vec{b}_3^{k+1} = \vec{b}_3^k + \vec{m}^{k+1} - \vec{n}^{k+1} \\ b_4^{k+1} = b_4^k + \nabla \cdot \vec{n}^{k+1} - q^{k+1} \end{cases} . \tag{4.16}$$

The original minimization problem can be split into the following sub-problems,

$$u_1^{k+1} = \arg\min_{u_1} E\left(u_1, u_2^k,\ \phi^k,\ \vec{p}^k,\ \vec{n}^k,\ \vec{m}^k,\ q^k\right), \tag{4.17}$$

$$u_2^{k+1} = \arg\min_{u_2} E\left(u_1^{k+1},\ u_2, \phi^k,\ \vec{p}^k,\ \vec{n}^k,\ \vec{m}^k, q^k\right), \tag{4.18}$$

$$\phi^{k+1} = \arg\min_{\phi} E\left(u_1^{k+1},\ u_2^{k+1},\ \phi,\ \vec{p}^k,\ \vec{n}^k,\ \vec{m}^k,\ q^k\right), \tag{4.19}$$

$$\vec{p}^{k+1} = \arg\min_{\vec{p}} E\left(u_1^{k+1},\ u_2^{k+1},\ \phi^{k+1},\ \vec{p},\ \vec{n}^k,\ \vec{m}^k,\ q^k\right), \tag{4.20}$$

$$\vec{n}^{k+1} = \arg\min_{\vec{n}} E\left(u_1^{k+1},\ u_2^{k+1},\ \phi^{k+1},\ \vec{p}^{k+1},\ \vec{n},\ \vec{m}^k,\ q^k\right), \tag{4.21}$$

$$\vec{m}^{k+1} = \arg\min_{\vec{m}} E\left(u_1^{k+1},\ u_2^{k+1},\ \phi^{k+1},\ \vec{p}^{k+1},\ \vec{n}^{k+1},\ \vec{m},\ q^k\right), \tag{4.22}$$

$$q^{k+1} = \arg\min_{q} E\left(u_1^{k+1},\ u_2^{k+1},\ \phi^{k+1},\ \vec{p}^{k+1},\ \vec{n}^{k+1},\ \vec{m}^{k+1},\ q\right). \tag{4.23}$$

The solutions to the sub-problems are presented below. Using standard variational methods, we solve (4.17) and (4.18) respectively as

$$u_1^{k+1} = \frac{\int_\Omega f(x) H\left(\phi^k(x)\right) dx}{\int_\Omega H\left(\phi^k(x)\right) dx}, \tag{4.24}$$

$$u_2^{k+1} = \frac{\int_\Omega f(x) \left(1 - H\left(\phi^k(x)\right)\right) dx}{\int_\Omega \left(1 - H\left(\phi^k(x)\right)\right) dx}. \tag{4.25}$$

For the sub-problem of ϕ in (4.19), the Euler-Lagrange equations is

$$\begin{cases} F^{k+1} + \mu\eta\phi^{k+1} - \gamma_2 \Delta\phi^{k+1} = 0 \quad x \in \Omega \\ \left(\nabla\phi + \vec{b}_2^k - \vec{p}^k\right) \cdot \vec{N} = 0 \end{cases} . \tag{4.26}$$

where $F^{k+1} = Q^{k+1}\delta_\varepsilon\left(\phi^k\right) + \gamma(a + b(q^k)^2)\left|\vec{p}^k\right|\delta'_\varepsilon\left(\phi^k\right) + \gamma_2\nabla\cdot\vec{p}^k - \gamma_2\nabla\cdot\vec{b}_2^k = 0.$

To solve (4.20), we can derive $\vec{p}^{k+1}$ via a generalized soft thresholding formula and projection formula,

$$\begin{cases} \vec{A}^{k+1} = \nabla\phi^{k+1} + \vec{b}_2^k + \dfrac{\left(\lambda_1^k + \gamma_1\right)\vec{m}^k}{\gamma_2} \\ B^{k+1} = \gamma\left(a + b\left(q^k\right)^2\right)\delta_\varepsilon\left(\phi^k\right) \\ \tilde{\vec{p}}^{k+1} = \max\left(\left|\vec{A}^{k+1}\right| - \dfrac{\lambda_1^k + \gamma_1 + B^{k+1}}{\gamma_2}, 0\right)\dfrac{\vec{A}^{k+1}}{\left|\vec{A}^{k+1}\right| + 10^{-6}} \\ \vec{p}^{k+1} = \dfrac{\tilde{\vec{p}}^{k+1}}{\left|\tilde{\vec{p}}^{k+1}\right|},\ \dfrac{\vec{0}}{\left|\vec{0}\right|} = \vec{0} \end{cases} . \tag{4.27}$$

For (4.21), the Euler-Lagrange equations on $\vec{n}$ is

$$\gamma_3\vec{n} - \gamma_4\nabla(\nabla\cdot\vec{n}) = \gamma_3\left(\vec{m}^k + \vec{b}_3\right) + \gamma_4\nabla\left(b_4^k - q^k\right) \tag{4.28}$$

$\vec{m}$ in (4.22) can be obtained as an exact solution. Considering the constraint in (4.12), the formula can be derived as

$$\begin{cases} \tilde{\vec{m}}^{k+1} = \vec{n}^{k+1} - \vec{b}_3^k + \dfrac{\left(\lambda_1^k + \gamma_1\right)\vec{p}^{k+1}}{\gamma_3} \\ \vec{m}^{k+1} = \dfrac{\tilde{\vec{m}}^{k+1}}{\max\left(1, |\tilde{\vec{m}}^{k+1}|\right)} \end{cases} . \tag{4.29}$$

Lastly, q in (4.23) also has an analytical solution

$$2bq^{k+1}\left|\vec{p^{k+1}}\right|\delta_\varepsilon\left(\phi^{k+1}\right) + \gamma_4\left(q^{k+1} - \nabla\cdot\vec{n}^{k+1} - b_4^k\right) = 0. \tag{4.30}$$

Having formulated the split-Breman algorithm for alternating direction optimization, we will now solve each sub-problem numerically. We can discretize the image domain pixel by pixel with the rows and column numbers as indices. The gradients can be represented approximately by forward, backward and central finite differences

$$\nabla^+\phi_{i,j} = \begin{bmatrix} \partial^+_{x_1}\phi_{i,j} \\ \partial^+_{x_2}\phi_{i,j} \end{bmatrix},\ \nabla^-\phi_{i,j} = \begin{bmatrix} \partial^-_{x_1}\phi_{i,j} \\ \partial^-_{x_2}\phi_{i,j} \end{bmatrix},\ \nabla^o\phi_{i,j} = \begin{bmatrix} \partial^o_{x_1}\phi_{i,j} \\ \partial^o_{x_2}\phi_{i,j} \end{bmatrix}, \tag{4.31}$$

where

$$\begin{cases} \partial^+_{x_1}\phi_{i,j} = \phi_{i+1,j} - \phi_{i,j} \\ \partial^-_{x_1}\phi_{i,j} = \phi_{i,j} - \phi_{i-1,j} \end{cases}, \begin{cases} \partial^+_{x_2}\phi_{i,j} = \phi_{i,j+1} - \phi_{i,j} \\ \partial^-_{x_2}\phi_{i,j} = \phi_{i,j} - \phi_{i,j-1} \end{cases}, \begin{cases} \partial^o_{x_1}\phi_{i,j} = \dfrac{1}{2}\left(\phi_{i+1,j} - \phi_{i-1,j}\right) \\ \partial^o_{x_2}\phi_{i,j} = \dfrac{1}{2}\left(\phi_{i,j+1} - \phi_{i,j-1}\right) \end{cases}. \tag{4.32}$$

The discretized Laplacian of ϕ can be stated as

$$\Delta\phi_{i,j} = \nabla^- \cdot \left(\nabla^+\phi_{i,j}\right) = \phi_{i-1,j} + \phi_{i,j-1} + \phi_{i+1,j} + \phi_{i,j+1} - 4\phi_{i,j}, \tag{4.33}$$

where the other variables can be approximated in similar ways.

(4.17) and (4.18) can be calculated directly as

$$u_1^{k+1} = \frac{\sum_{i=1}^{M}\sum_{j=1}^{N} f_{i,j} H_\varepsilon\left(\phi^k_{i,j}\right)}{\sum_{i=1}^{M}\sum_{j=1}^{N} H_\varepsilon\left(\phi^k_{i,j}\right)}, \tag{4.34}$$

$$u_2^{k+1} = \frac{\sum_{i=1}^{M}\sum_{j=1}^{N} f_{i,j}\left(1 - H_\varepsilon\left(\phi^k_{i,j}\right)\right)}{\sum_{i=1}^{M}\sum_{j=1}^{N}\left(1 - H_\varepsilon\left(\phi^k_{i,j}\right)\right)}, \tag{4.35}$$

where M and N are the numbers of rows and columns of the image f.

Next, to discretize the formula of ϕ obtained in (4.26), we introduce the following intermediate variables

$$\begin{cases} F^{k+1} = Q^{k+1}\delta_\varepsilon\left(\phi^k\right) + \left(a + b\left(q^k\right)^2\right)\left|\vec{p}^{\,k}\right|\delta'_\varepsilon\left(\phi^k\right) + \gamma_2\nabla\cdot\vec{p}^{\,k} - \gamma_2\nabla\cdot\vec{b}_2^{\,k} & x \in \Omega \\ \vec{G}^{k+1} = \vec{p}^{\,k} - \vec{b}_2^{\,k} \end{cases}, \tag{4.36}$$

and write the original Eular-Lagrange equations in the more concise form below

$$\begin{cases} F^{k+1} + \mu\eta\phi^{k+1} - \gamma_2\Delta\phi^{k+1} = 0 & x \in \Omega \\ \nabla\phi^{k+1} \cdot \vec{N} = \vec{G}^{k+1} \cdot \vec{N} & x \in \partial\Omega \end{cases}. \tag{4.37}$$

Based on (4.33) and (4.26), we can easily design the Gauss-Seidel iterative scheme of ϕ as

$$\left(\mu\eta + 4\gamma_2\right)\phi_{i,j}^{k+1,l+1} = \gamma_2\left(\phi_{i-1,j}^{k+1,l+1} + \phi_{i,j-1}^{k+1,l+1} + \phi_{i+1,j}^{k+1,l} + \phi_{i,j+1}^{k+1,l}\right) - F_{i,j}^{k+1}. \tag{4.38}$$

Alternatively, ϕ can be solved by Fast Fourier transform (FFT)[78]. The discretized solution of $\vec{p}$ as obtained from (4.27) is

$$\begin{cases} \vec{A}_{i,j}^{k+1} = \nabla^+\phi_{i,j}^{k+1} + \dfrac{\left(\lambda_1^k + \gamma_1\right)\vec{m}_{i,j}^k}{\gamma_2} + \vec{b_{2i,j}}^k \\ B^{k+1} = \left(a + b\left(q_{i,j}^k\right)^2\right)\delta_\varepsilon'\left(\phi_{i,j}^{k+1}\right) \\ \vec{\tilde{p}}_{i,j}^{k+1} = \max\left(\left|\vec{A}_{i,j}^{k+1}\right| - \dfrac{\lambda_{1i,j}^k + \gamma_1 + B_{i,j}^{k+1}}{\gamma_2}, 0\right)\dfrac{\vec{A}_{i,j}^{k+1}}{\left|\vec{A}_{i,j}^{k+1}\right| + 10^{-6}} \\ \vec{p}_{i,j}^{k+1} = \dfrac{\vec{\tilde{p}}_{i,j}^{k+1}}{\left|\vec{\tilde{p}}_{i,j}^{k+1}\right|},\ \dfrac{\vec{0}}{\left|\vec{0}\right|} = \vec{0} \end{cases}. \tag{4.39}$$

Since the form of $\vec{n}$ in (4.28) is similar to that of ϕ, the solution of $\vec{n}$ can also be written similarly. Again, to simplify the equation, we introduce

$$\begin{cases} \vec{H}_{i,j}^{k+1} = -\gamma_3\left(\vec{m}_{ij}^k + \vec{b}_{3i,j}^k\right) - \gamma_4\nabla\left(b_{4ij}^k - q_{ij}^k\right) & x \in \Omega \\ G_{i,j}^k = q_{i,j}^k - b_{4i,j}^k & x \in \partial\Omega \end{cases}, \tag{4.40}$$

and (4.28) becomes

$$\begin{cases} \vec{H}^{k+1} + \gamma_3\vec{n}^{k+1} - \gamma_4\nabla\left(\nabla\cdot\vec{n}^{k+1}\right) = 0 & x \in \Omega \\ \nabla\cdot\vec{n}^{k+1}\vec{N} = G^k\vec{N} & x \in \partial\Omega \end{cases}. \tag{4.41}$$

Introducing the discretized form of $\vec{n}$, its Gauss-Seidel iterative scheme can be easily designed as

$$\begin{cases} (\gamma_3+2\gamma_4)\, n_{1i.j}^{k+1,l+1} = \gamma_4\left(n_{1i-1,j}^{k+1,l+1}+n_{1i+1,j}^{k+1,l}+n_{2i+1,j}^{k+1,l}-n_{2i+1,j-1}^{k+1,l}-n_{2i,j}^{k+1,l}+n_{2i,j-1}^{k+1,l}\right)-H_{1i,j}^{k+1} \\ (\gamma_3+2\gamma_4)\, n_{2i,j}^{k+1,l+1} = \gamma_4\left(n_{1i,j+1}^{k+1,l}-n_{1i-1,j+1}^{k+1,l}-n_{1i,j}^{k+1,l+1}+n_{1i-1,j}^{k+1,l+1}+n_{2i,j-1}^{k+1,l+1}+n_{2i,j+1}^{k+1,l}\right)-H_{2i,j}^{k+1} \\ \vec{n}_{ij}^{k+1,0} = \vec{n}_{i,j}^{k} \end{cases}. \tag{4.42}$$

Here $\vec{n}$ can be solved with FFT as well. For $\vec{m}$ in (4.29), its discretized analytical solution with projection formula is

$$\begin{cases} \vec{\bar{m}}_{i,j}^{k+1} = \vec{n}_{i,j}^{k+1}+\dfrac{\left(\lambda_{1i,j}^{k}+\gamma_1\right)\vec{p}_{i,j}^{k+1}}{\gamma_3}-\vec{b}_{3i,j}^{k} \\ \vec{m}_{i,j}^{k+1} = \dfrac{\vec{\bar{m}}_{i,j}^{k+1}}{\max\left(1,\left|\vec{\bar{m}}_{i,j}^{k+1}\right|\right)} \end{cases}. \tag{4.43}$$

The q obtained in (4.30) can also be drawn into a simple analytical solution

$$\left(\gamma_4+2b\gamma\left|\vec{p}_{i,j}^{k+1}\right|\delta_\varepsilon\left(\phi_{i,j}^{k+1}\right)\right)q_{i,j} = \gamma_4\nabla\cdot\vec{n}_{i,j}^{k+1}+\gamma_4 b_{4ij}^{k}. \tag{4.44}$$

After one complete iteration, the Bregman iterators are updated as (4.16). The following error tolerances should also be checked to determine convergence, i. e.,

$$T_s^{k+1}\le \mathrm{Tol},\ (s=1,2,3,4),\ \Phi^{k+1}\le \mathrm{Tol},\ \Sigma^{k+1}\le \mathrm{Tol}, \tag{4.45}$$

where $\mathrm{Tol}=0.01$. $T_s^{k+1},\ \Phi^{k+1},\ \Sigma^{k+1}$ are defined as

$$\left\{T_1^{k+1},\ T_2^{k+1},\ T_3^{k+1},\ T_4^{k+1}\right\} = \left\{\frac{\left\|\lambda_1^{k+1}-\lambda_1^{k}\right\|_{L_1}}{\left\|\lambda_1^{k}\right\|_{L_1}},\ \frac{\left\|\vec{b}_2^{k+1}-\vec{b}_2^{k}\right\|_{L_1}}{\left\|\vec{b}_2^{k}\right\|_{L_1}},\ \frac{\left\|\vec{b}_3^{k+1}-\vec{b}_3^{k}\right\|_{L_1}}{\left\|\vec{b}_3^{k}\right\|_{L_1}},\ \frac{\left\|b_4^{k+1}-b_4^{k}\right\|_{L_1}}{\left\|b_4^{k}\right\|_{L_1}}\right\}, \tag{4.46}$$

$$\Phi^{k+1} = \frac{\left\|\phi^{k+1}-\phi^{k}\right\|_{L_1}}{\left\|\phi^{k}\right\|_{L_1}},\ \Sigma^{k+1} = \frac{\left\|E^{k+1}-E^{k}\right\|}{\left\|E^{k}\right\|}. \tag{4.47}$$

The complete algorithm is summarized in Algorithm 3.

Algorithm 3 The split-Bregman algorithm for the CVLE model

(1) Initialization: Set $\alpha_1,\ \alpha_2,\ \mu,\ a,\ b$.

(2) **while** *any stopping criterion is not satisfied* **do**

Calculate $\mathrm{u}_1^{k+1},\ \mathrm{u}_2^{k+1}$ from (4.24) and (4.25)

Calculate ϕ^{k+1} from (4.26)

Calculate $\vec{p}^{k+1}$ from (4.27)

Calculate $\vec{n}^{k+1}$ from (4.28)

Calculate $\vec{m}^{k+1}$ from (4.29)

Calculate q^{k+1} from (4.30)

Calculate $\lambda_1^{k+1}, \vec{b}_2^{k+1}, \vec{b}_3^{k+1}, b_4^{k+1}$ from (4.16)

end while

4.4 Experimental results

The following experiments compare the performance of the CV, the CVL, the CVE, and the CVLE models in contour inpainting. The performance of the models are tested against short and long sections of missing contours, different numbers of landmarks, as well as real-world images and noisy images. The running environment is PC (Intel (R) Core (TM) i7-7700 CPU @ 3.60GHz 3.60 GHz; memory: 16.0 GB; code running environment: Matlab R2017a).

Since the CVE, the CVL, and the CVLE model all work for contour inpainting to different extents, we designed experiments to compare them. The image of the letters 'CV' contains some damaged regions. The original broken image is shown in Fig. 4-1 (a), and the initialization of the zero level set for all of the models is shown in Fig. 4-1 (b). Segmentation results obtained from the CV, CVL, CVE, and CVLE models are shown in Fig. 4-1 (c-f) respectively. Some landmarks are placed in the middle of the missing sections of the contour. Results show that the CVE and CVLE can both inpaint small sections of the contour, though the parameters for the CVE are very hard to tune. The CVL mostly failed due to the lack of landmarks.

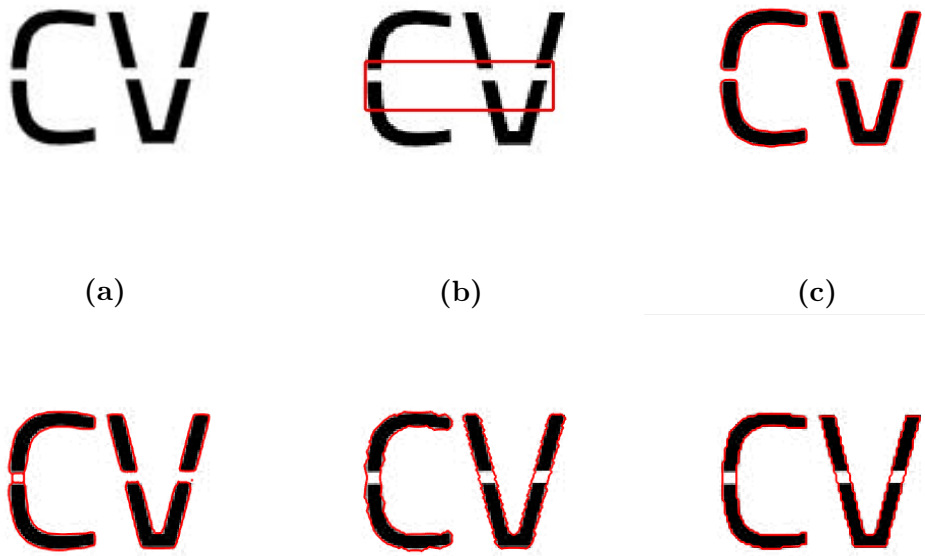

(a) **(b)** **(c)**

(d) **(e)** **(f)**

Fig. 4-1: Results of four different methods of repair broken letters 'CV'. (a) is the original image, (b) is the initial contour, (c-f) are the segmentation results obtained cia the CV, CVL, CVE, and CVLE models respectively. The parameters are $\gamma_1 = 5, \gamma_2 = 5, \gamma_3 = 5, \gamma_4 = 5, \alpha_1 = 0.5, \alpha_2 = 0.5$.

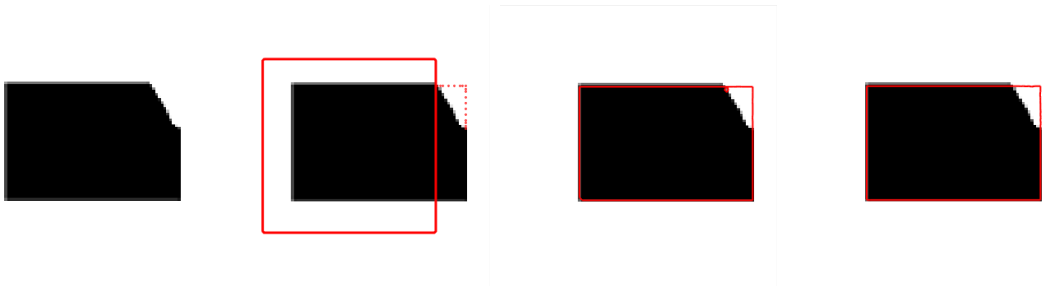

(a) **(b)** **(c)** **(d)**

Fig. 4-2: Repair of a broken rectangle. (a) is the original image, (b) is the initial contour and piror landmark, (c) is the result obtained from the CVL model, (d) is the result obtained from the CVLE model. The parameters are $\gamma_1 = 1, \gamma_2 = 3, \gamma_3 = 5, \gamma_4 = 10, \alpha_1 = 1.1, \alpha_2 = 0.9$ for the CVLE model.

To compare the performance of the CVL and CVLE in recovering large missing contours, we next segmented a rectangle with a clipped corner in Fig. 4-2. Fig. 4-2 (a) shows a triangle with a missing corner, Fig. 4-2 (b) shows the initial contour and landmark points, Fig. 4-2 (c), (d) are segmentation results via the CVL and CVLE model respectively. For similar inpainting effects, the CVL required 26 landmark points whereas the CVLE only required 20.

Fig. 4-3 presents another comparison between the CVE and the CVLE. Fig. 4-3 (a) shows the original broken image, (b) presents the initial zero level set and landmark points, and (c), (d) give the segmentation results via CVE and CVLE model respectively. The same conclusion as in [72] can be drawn, i. e., it is difficult to control the shape of the inpainted contours via the CVE, while the CVLE successfully recreated the circle under the influence of the landmark constraints.

In the next set of experiments, we study the effect of the number of landmark points and their positions on the segmentation contour. Setting different amounts of landmark points lead to different segmentation results. The more landmarks we set within a reasonable limit, the more the contour will be defined by landmarks. However, setting more landmarks beyond the necessary amount will not increase segmentation accuracy further, as shown in Fig. 4-4 (g), (h). In Fig. 4-4 (e-h), the number of landmark points are 3, 9, 11, 15, respectively. As we can see, the inpainted contour became more accurate with more landmarks. However, setting more than 15

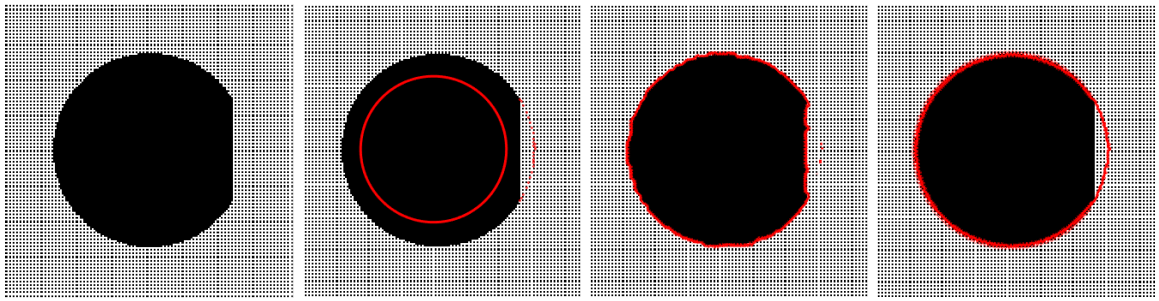

(a) **(b)** **(c)** **(d)**

Fig. 4-3: Broken circle repair experiment. (a) is the original image, (b) is the initial contour and prior landmarks, (c) is the result obtained from the CVL model, (d) is the result obtained from the CVLE model. The parameters for the CVLE model are $\gamma_1 = 7, \gamma_2 = 20, \gamma_3 = 5, \gamma_4 = 2, \alpha_1 = 1.1, \alpha_2 = 1.2$.

landmarks has no additional effects on the contour.

The placement of landmark points is also essential, especially when the total number of landmarks is small. Using Fig. 4-4 (d) as an example of a well-segmented image, we take away some landmarks from different locations in Fig. 4-5. In Fig. 4-5 (a), (b) and (c), we remove landmarks from the bottom, top, and middle of the missing corner of the rectangle respectively. As a result, the recovered contour in Fig. 4-5 (f) has distortions around the middle, the sharpness of the tip is not well maintained in (e), but the result in (d) does not change significantly. Therefore, we observe that it is more effective to place landmarks at the vertices or corners of an object. It is typically the case that the better the landmarks are positioned, the fewer landmarks we need.

One real-world application of the CVLE model is segmentation of medical images. MRI images are often challenging due to the presence of detailed features and noise. Fig. 4-6 (a) and Fig. 4-7 (a) are two examples of the original images from a brain CT, Fig. 4-6 (b) and Fig. 4-7 (b) are the initial contours, Fig. 4-6 (c) and Fig. 4-7 (c) are the results obtained via the CV model, and Fig. 4-6 (d) and Fig. 4-7 (d) are the results from CVLE. The CV model fails to segment the brain images due to its simplicity, whereas the CVLE model produced good results under the same initial level set function. This experiment demonstrates that the CVLE retains details better in the segmentation of MRI images.

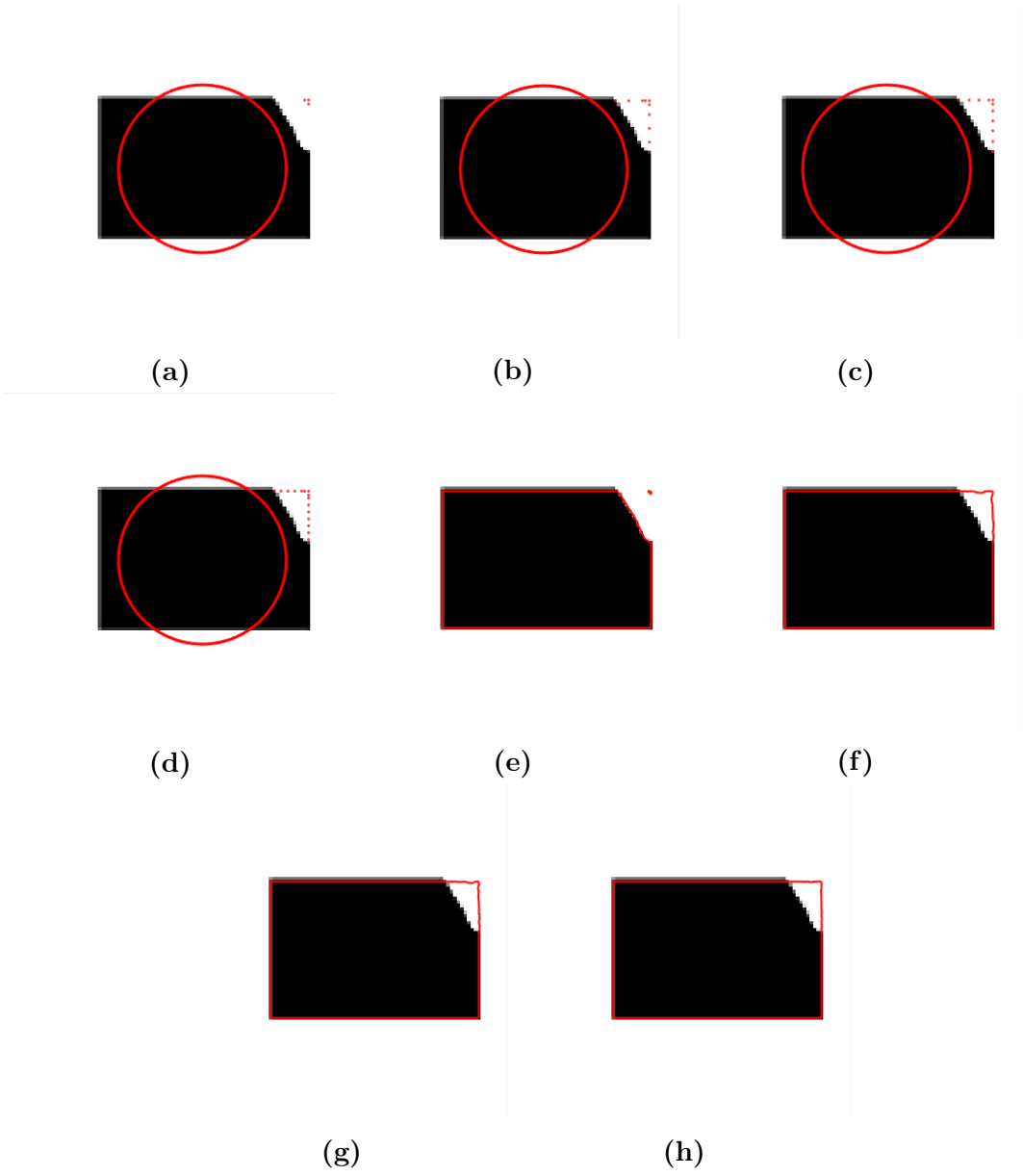

Fig. 4-4: Different number of landmarks affect the inpainted contour. (a-d) are the initial setups for 3, 9, 11, 15 landmarks respectively, (e-h) are the segmentation results via the CVLE for 3, 9, 11, 15 landmarks respectively.

4.5 Summary

In this chapter, we presented the Chan-Vese model with landmark constraints and elastica (CVLE). The CVLE combines the Euler's elastica and the Chan-Vese model with landmark constraints (CVL) to inpaint large sections of illusory contours. We then solved the CVLE model using the split-Bregman method and a projection scheme.

Experiments show that the CVLE works well for guided contour inpainting as well as sharpening of local details. The placement and quantity of landmarks both affect the inpainting results. The more representative the landmarks are of the image features, and the more landmarks are used within necessity, the more accurate and better defined the interpolated contour typically will be. For future directions, we can integrate automatic landmarks detection methods as well as incorporate the landmark constraints and elastica term into other variational models.

In the next chapter, we will propose a new algorithm for solving the self-repelling snakes model, a geodesic active contour-based model with the topology preservation constraint.

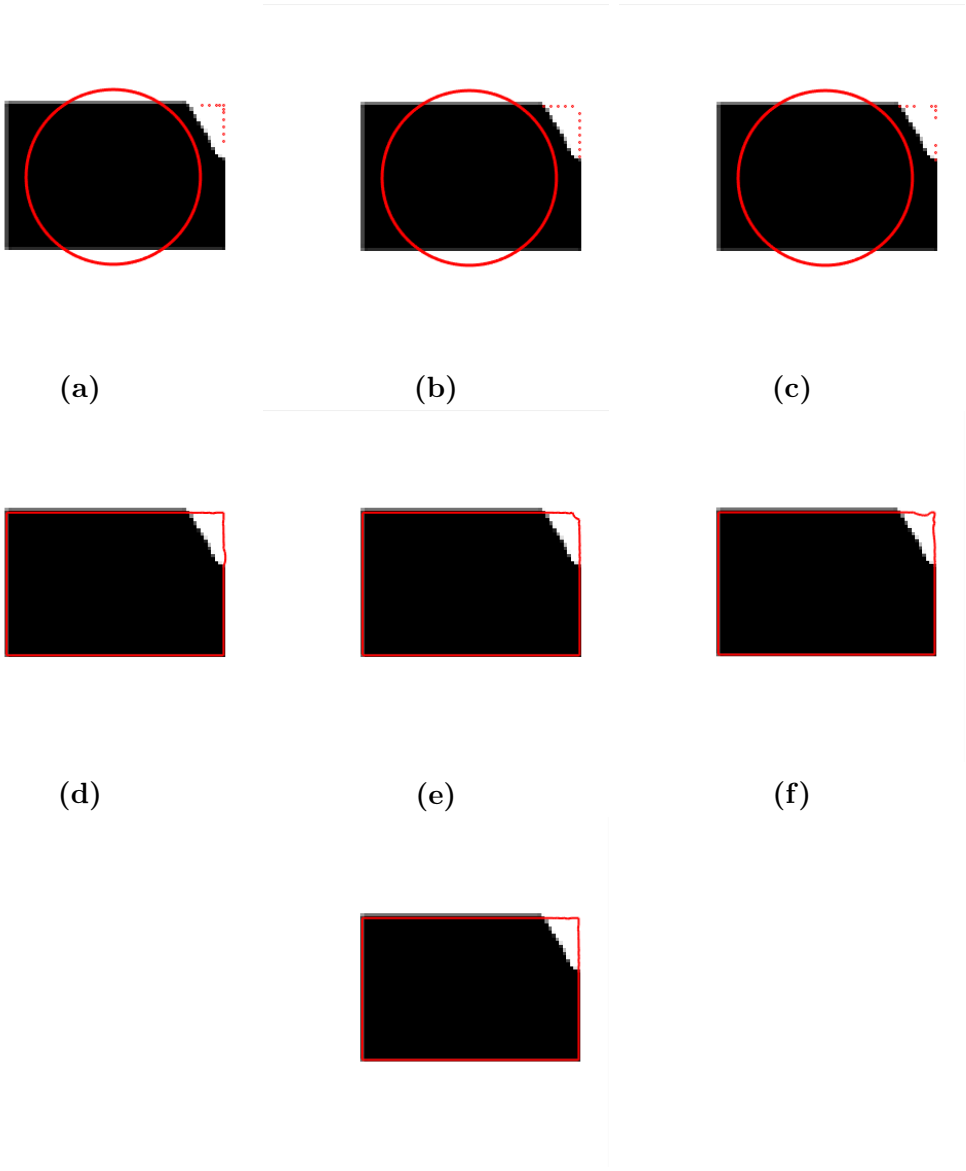

Fig. 4-5: The significance of the location of landmarks. (a-c) are the initial setups where landmarks are missing from the bottom, top, and middle of the missing corner of the rectangle respectively. (d-f) are the segmentation results for (a-c) respectively via the CVLE. (g) is the segmentation result using the full set of landmarks.

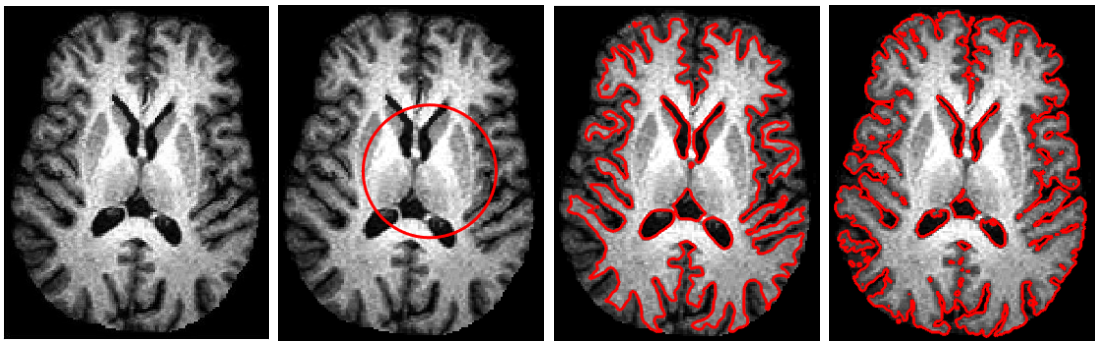

(a) **(b)** **(c)** **(d)**

Fig. 4-6: Brain MRI image segmentation experiment, image taken from [10]. (a) is the original image, (b) is the initial contour, (c) is the segmentation result via the CV model, (d) is the segmentation result via the CVLE model.

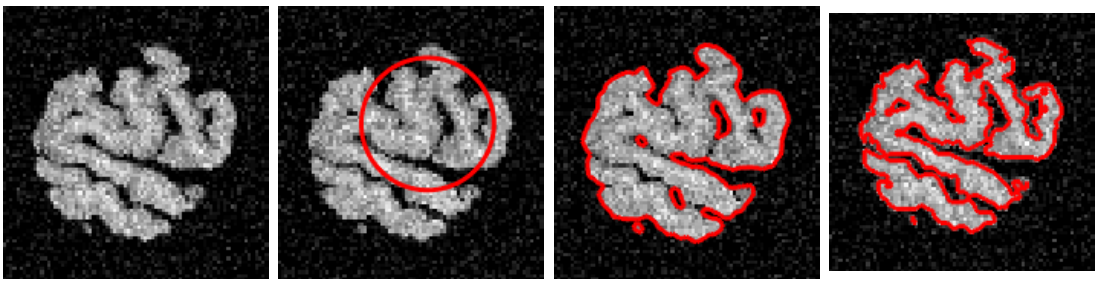

(a) **(b)** **(c)** **(d)**

Fig. 4-7: Noisy brain MRI image segmentation experiments, image taken from [8]. (a) is the original image, (b) is the initial contour, (c) is the segmentation result via the CV model, (d) is the segmentation result via the CVLE model.

Chapter 5

The Self-repelling Snakes Model for Topology Preservation

In the previous two chapters, we designed variational models with landmark constraints. In this chapter, we will design a new solution for a variational model with the topology preservation constraint.

Topology preservation in image segmentation is an external constraint to discourage changes in the topology of the segmentation contour. It typically applies to problems where the object topology is known a priori. The concept of topology preservation, or prevention of changes in the contour topology, can be intuitively linked to contour evolution. Many variational models are designed to prevent the contour from self-intersecting, i.e. merging or splitting, via a constraint term. For example, Han et al. [79] proposed a simple-point detection scheme in an implicit level set framework in 2003. Cecil et al. [80] monitored the changes in the Jacobian of the level set. In 2005, Alexandrov et al. [81] recast the topology preservation problem to a shape optimization problem of the level sets, where narrow bands around the segmentation contours are discouraged from overlapping. Sundaramoorthi and Yezzi [82] proposed an approach based on knot energy minimization, to the same effect. Rochery et al. [83] used a similar idea while introducing a non-local regularization term, which was applied in the tracking of long thin objects in remote sensing images. Building on the previous ideas, the self-repelling snakes (SR) model was proposed by

Le Guyader et al. in 2008 [8]. The SR uses an implicit level set representation for the curve and adds a non-local repulsion term to the classic geodesic active contour model (GAC) [9]. In the follow-up work [84], the short time existence/uniqueness and Lipschitz regularity property of the SR model were studied. Later, [85] successfully extended the SR model to non-local topology-preserving segmentation-guided registration. Attempts have also been made [86] to combine the SR with the region-based Chan-Vese model [14], though a direct combination proved unsuccessful.

The SR model has intuitive and straightforward geometric interpretations, but its non-local term leads to complications in the numerical implementation. To the best of our knowledge, the SR model has always been solved through the additive operator splitting (AOS) [87] strategy. The derivation of gradient descent equations is complicated and requires the upwind difference discretization scheme. Furthermore, though the AOS is stable, the memory requirement grows quadratically with the size of the image. In this work, we propose an alternative solution using the split-Bregman method that aims towards a more concise algorithm and less memory usage. We introduce an intermediate variable to split the original problem into two sub-problems, which turns a second-order optimization problem into two first-order ones. Solving the new sub-problems no longer requires taking complex differentials of the geodesic curvature term. We also replace the re-initialization of the signed distance function with a simple projection scheme. As a result, the optimization of the level set function is simplified. In addition, to address some problems arising from the split-Bregman solution, we replace the Heaviside representation of the level set in [8] with one that performed better in our algorithm.

In this chapter, we first review and provide some intuition to the original SR model. Then, we design the split-Bregman algorithm for the SR model and derive the Euler-Lagrange equations or gradient descent equations for the sub-problems. Next, we present the discretization schemes for the sub-problems which are solved by alternating iterative optimization. Finally, experimental results are provided and comparisons are made between the two solutions.

5.1 The self-repelling snakes model

The original SR model as proposed in [8] is an edge-based segmentation model based on the GAC [9]. It adopts the variational level set formulation [52], where the segmentation contour is implicitly represented as the zero level line of a signed distance function [33]. An energy functional is minimized until convergence is reached and the segmentation contour is obtained. The energy functional comprises three terms, two of which are taken from the GAC model and contribute to edge detection and the balloon force respectively, while the last one accounts for the self-repulsion of contour as it approaches itself.

The definition of the SR model is as follows. Let $f(x) : \Omega \to R$ be a scalar value image, $x \in \Omega$, and Ω is the domain of the image. The standard edge detect function $g(x) \in [\,0, 1\,]$ is given by

$$g(x) = \frac{1}{1 + \rho|\nabla(G_\sigma * f)|^s}, \tag{5.1}$$

where $s = 1$ or 2, ρ is a scaling parameter, and G_σ denotes a Gaussian convolution of the image with a standard deviation of σ. The object boundary C is represented by the zero set of a level set function ϕ,

$$C = \{x \in \Omega | \phi(x) = 0\}. \tag{5.2}$$

The level set function ϕ is defined as a signed distance function, as in (2.10). As a signed distance function, ϕ satisfies the constraint condition (2.11), i.e. the Eikonal equation. To represent the image area and contour, we make use of the Heaviside function $H(\phi)$ and Dirac functions $\delta(\phi)$. Since the original Heaviside function is discontinuous and therefore indifferentiable, we adopt the smoothed versions of the function [52] below,

$$H_\varepsilon(\phi) = \begin{cases} \frac{1}{2}\left(1 + \frac{\phi}{\varepsilon} + \frac{1}{\pi}\sin\left(\frac{\pi\phi}{\varepsilon}\right)\right) & |\phi| \leq \varepsilon \\ 1 & \phi > \varepsilon \\ 0 & \phi < -\varepsilon \end{cases}, \tag{5.3}$$

$$\delta_\varepsilon(\phi) = \begin{cases} \frac{1}{2\varepsilon}\left(1 + \cos\left(\frac{\pi\phi}{\varepsilon}\right)\right) & |\phi| \leq \varepsilon \\ 0 & |\phi| > \varepsilon \end{cases}. \tag{5.4}$$

This scheme is different from the ones used in the original model in [8]. In particular, ε does not affect the entire image domain, which improves stability of edge-based models. The effect is more apparent in our split-Bregman algorithm, as we will discuss further in section 5.2.

Given the above, the energy functional $E(\phi)$ of the SR model can be written as

$$E(\phi) = \gamma E_g(\phi) + \alpha E_a(\phi) + \beta E_r(\phi), \tag{5.5}$$

where γ, α, β are penalty parameters that balance three terms.

$$E_g(\phi) = \int_\Omega g(x)|\nabla H_\varepsilon(\phi(x))|dx = \int_\Omega g(x)|\nabla\phi(x)|\delta_\varepsilon(\phi(x))dx. \tag{5.6}$$

$E_g(\phi)$ is the geodesic length of the contour. The total variation of the Heaviside function, or the total length of the contour, is weighted by the edge detector in (5.1).

$$E_a(\phi) = \int_\Omega g(x)(1 - H_\varepsilon(\phi(x)))dx. \tag{5.7}$$

$E_a(\phi)$ is the closed area of the contour also weighted by the edge detector. It contributes to a balloon force that pushes the segmentation contour over weak edges [28].

$$E_r(\phi) = -\int_\Omega\int_\Omega e^{\frac{|x-y|^2}{d^2}}(\nabla\phi(x)\cdot\nabla\phi(y))h_\varepsilon(\phi(x))h_\varepsilon(\phi(y))dxdy. \tag{5.8}$$

$E_r(\phi)$ describes the self-repulsion of the contour [8]. $e^{-\frac{|x-y|^2}{d^2}}$ measures the distance

of the two points x and y, e.g. the further away the points the smaller the repulsion. In (5.8), $h_\varepsilon(\phi(x))$ and $h_\varepsilon(\phi(y))$ denote the narrow bands around the points x and y, where,

$$h_\varepsilon(\phi(x)) = H_\varepsilon(\phi(x) + l)(1 - H_\varepsilon(\phi(x) - l)), \tag{5.9}$$

$$h_\varepsilon(\phi(y)) = H_\varepsilon(\phi(y) + l)(1 - H_\varepsilon(\phi(y) - l)). \tag{5.10}$$

When the points x and y are further than distance l from the contour, $h_\varepsilon(\phi(x))h_\varepsilon(\phi(y)) \to 0$. This signifies that the points outside the narrow bands are largely unaffected by repulsion. For $-\nabla\phi(x) \cdot \nabla\phi(y)$, if the outwards unit normal vectors to the level lines passing through x and y have opposite directions, i.e., the contours passing x and y are merging or splitting, then the functional approaches the maximum value. Thus, the minimization of $E_r(\phi)$ prevents the self-intersection of the contour.

Given the energy functional (5.5) and the Eikonal equation (2.11) , the variational formulation for SR is

$$\begin{aligned} &\min_\phi E(\phi) = \gamma E_g(\phi) + \alpha E_a(\phi) + \beta E_r(\phi) \\ &\text{s.t. } |\nabla\phi| = 1 \end{aligned}, \tag{5.11}$$

and the evolution equation of $\phi(x)$ derived from $E_g(\phi)$ and $E_a(\phi)$ is

$$\frac{\partial\phi(x,t)}{\partial t} = \delta_\varepsilon(\phi(x,t))(\gamma\nabla \cdot (g(x)\frac{\nabla\phi(x,t)}{|\nabla\phi(x,t)|}) + \alpha g(x)), \tag{5.12}$$

where

$$\nabla \cdot (g(x)\frac{\nabla\phi(x,t)}{|\nabla\phi(x,t)|}) = \nabla g(x) \cdot \frac{\nabla\phi(x,t)}{|\nabla\phi(x,t)|} + g(x)\nabla \cdot \frac{\nabla\phi(x,t)}{|\nabla\phi(x,t)|}. \tag{5.13}$$

(5.13) is the geodesic curvature that shifts the contour towards the edges detected by $g(x)$. In the image areas with near-uniform intensity, $\nabla g(x) \to 0$, $g(x) = 1$. Since $\nabla \cdot (g(x)\frac{\nabla\phi(x,t)}{|\nabla\phi(x,t)|}) \to 0$ in those areas, the geodesic curvature term has little effect and the balloon force $\alpha g(x)$ dominates.

Lastly, the evolution equation derived from the repulsion term is

$$\frac{\partial \phi(x,t)}{\partial t} = \frac{4\beta}{d^2} h_\varepsilon(\phi(x,t)) \int_\Omega e^{-\frac{|x-y|^2}{d^2}} ((x-y)\cdot \nabla\phi(y,t)) h_\varepsilon(\phi(y,t)) dy, \tag{5.14}$$

To summarize, by applying variational methods to the three energy terms and substituting $\delta_\varepsilon(\phi(x))$ with $|\nabla\phi(x)|$, the following evolution equations can be derived

$$\begin{cases} \frac{\partial \phi(x,t)}{\partial t} = |\nabla\phi|(\gamma \nabla\cdot(g(x)\frac{\nabla\phi(x,t)}{|\nabla\phi(x,t)|}) + \alpha g(x)) \\ +\frac{4\beta}{d^2} h_\varepsilon(\phi(x,t)) \int_\Omega e^{-\frac{|x-y|^2}{d^2}} ((x-y)\cdot\nabla\phi(y,t)) h_\varepsilon(\phi(y,t)) dy & x\in\Omega, t>0 \\ \phi(x,0) = \phi_0(x) & x\in\Omega\cup\partial\Omega, t=0\cdot \\ \frac{\partial\phi}{\partial\vec{n}} = 0 & x\in\partial\Omega, t\geq 0 \\ |\nabla\phi| = 1 \end{cases} \tag{5.15}$$

With regards to the constraint $|\nabla\phi| = 1$, the dynamic re-initialization scheme below is adopted in [8],

$$\begin{cases} \frac{\partial\psi(x,t)}{\partial t} + \sin(\phi(x))(|\nabla\psi(x,t)| - 1) = 0 \\ \psi(x,0) = \phi(x) \end{cases}. \tag{5.16}$$

The above is a typical Hamilton-Jacobi equation that can be discretized and solved through an up-wind difference scheme [33]. To solve (5.15), the original solution adopts the AOS strategy [87]. The first term on the r.h.s. of (5.15) is discretized with the half-point difference scheme and the harmonic averaging approximation. The next two terms adopt the up-wind scheme. Two semi-implicit schemes are constructed by concatenating the rows and columns of the image respectively,

$$\begin{aligned} \left(1 - 2tA_{x_1}\left(\phi^k\right)\right) v^{k+1} &= \phi^k + t\left(T^2\left(\phi^k\right) + T^3\left(\phi^k\right)\right), \\ \left(1 - 2tA_{x_2}\left(\phi^k\right)\right) w^{k+1} &= \phi^k + t\left(T^2\left(\phi^k\right) + T^3\left(\phi^k\right)\right), \end{aligned} \tag{5.17}$$

where A_{x_1}, A_{x_2} are the two concatenation matrices, v and w are intermediate variables, and T^2, T^3 are the up-wind discretizations of the second and third term of the r.h.s. of (5.15), the formulations of which are omitted here for brevity. For each $A_l\,(l \in (x_1, x_2))$,

$$A_{lij}\left(\phi^k\right) = \begin{cases} \frac{2\gamma\left|\nabla^o \phi_i^k\right|}{\left(\frac{\left|\nabla^o \phi_i^k\right|}{g_i} + \frac{\left|\nabla^o \phi_j^k\right|}{g_j}\right)} & j \in N_l(i) \\ -\sum\limits_{m \in N_l(i)} \frac{2\gamma\left|\nabla^o \phi_i^k\right|}{\left(\frac{\left|\nabla^o \phi_i^k\right|}{g_i} + \frac{\left|\nabla^o \phi_m^k\right|}{g_m}\right)} & j = i \\ 0 & else \end{cases}, \tag{5.18}$$

where i, j are two points in the image, $N_l(i)$ is the set of the nearest neighbors of i in the matrix A_l, $\left|\nabla^o \phi_i^k\right| = \sqrt{\left(\frac{\phi_{i+1,j} - \phi_{i-1,j}}{2}\right)^2 + \left(\frac{\phi_{i,j+1} - \phi_{i,j+1}}{2}\right)^2}$, and A_l is a diagonally dominant tridiagonal matrix. Finally, ϕ^{k+1} can be calculated as

$$\phi^{k+1} = \frac{1}{2}\left(v^{k+1} + w^{k+1}\right). \tag{5.19}$$

Since i and j span the entire image, if $\Omega \in R^{m \times n}$, then $A_l \in R^{(m \times n) \times (m \times n)}$. Consequently, the variable A greatly increases the memory requirement for the AOS solution. In the last step, (5.17) is solved via the Thomas algorithm which involves LR decomposition, forward substitution, and backward substitution, with the convergence rate of $O(N)$. In the following section, we will propose another solution to the SR with the split-Bregman method that aims to be faster by replacing the re-initialization step, more memory efficient by using compact intermediate variables, and more concise by bypassing the complex discretization schemes.

5.2 The split-Bregman algorithm for the self-repelling snakes model

The split-Bregman method is a fast alternating directional method often used in solving L^1-regularized constrained optimization problems [43]. To design the split-

Bregman algorithm for (5.5), we first introduce a splitting variable $\vec{w} = \nabla\phi$ and the Bregman iterator $\vec{b}$. We can re-formulate the energy minimization problem as

$$
\begin{aligned}
&(\phi^{k+1}, \vec{w}^{k+1}) = \arg\min_{\phi,\vec{w}} E(\phi, \vec{w}) \\
&= \left\{ \begin{array}{l} \gamma \int_\Omega g(x)|\vec{w}(x)|\delta_\varepsilon(\phi(x))dx + \alpha \int_\Omega g(x)(1 - H_\varepsilon(\phi(x)))dx \\ -\beta \int_\Omega \int_\Omega e^{-\frac{|x-y|^2}{d^2}} (\vec{w}(x) \cdot \vec{w}(y)) h_\varepsilon(\phi(x)) h_\varepsilon(\phi(y)) dxdy \\ +\frac{\mu}{2} \int_\Omega |\vec{w}(x) - \nabla\phi(x) - \vec{b}^k(x)|^2 dx \end{array} \right\}, \\
&s.t.\ |\vec{w}(x)| = 1
\end{aligned}
\tag{5.20}
$$

$$
\vec{b}^{k+1}(x) = \vec{b}^k(x) + \nabla\phi^{k+1}(x) - \vec{w}^{k+1}(x), \tag{5.21}
$$

where $\vec{b}^0 = \vec{0}$, $\vec{w}^0 = \vec{0}$, and μ is a penalty parameter. The original problem can then be solved as two sub-problems in alternating order for loops $k = 1, 2, ..., K$. The sub-problems are,

$$
\phi^{k+1} = \arg\min_{\phi} E_1(\phi) = E(\phi, \vec{w}^k), \tag{5.22}
$$

$$
\begin{aligned}
&\vec{w}^{k+1} = \arg\min_{\vec{w}} E_2(\vec{w}) = E(\phi^{k+1}, \vec{w}) \\
&s.t.\ |\vec{w}| = 1
\end{aligned}
\quad . \tag{5.23}
$$

To solve the sub-problem (5.22), we can derive the following evolution equation of ϕ via standard variational methods [18],

$$
\frac{\partial\phi(x,t)}{\partial t} = \left\{ \begin{array}{l} -\gamma g(x)|\vec{w}^k(x)|\delta'_\varepsilon(\phi(x,t)) + \alpha g(x)\delta_\varepsilon(\phi(x,t)) + \mu\Delta\phi(x,t) \\ +2\beta h'_\varepsilon(\phi(x,t))\vec{w}^k(x) \cdot \int_\Omega e^{-\frac{|x-y|^2}{d^2}} \vec{w}^k(y) h_\varepsilon(\phi(y,t)) dy \\ +\mu(\nabla \cdot \vec{b}^k(x) - \nabla \cdot \vec{w}^k(x)) \end{array} \right\}, \tag{5.24}
$$

The initial condition and boundary condition are as below,

$$\begin{cases} \phi^{k+1}(x) = \phi^k(x) & x \in \Omega \cup \partial\Omega \\ \nabla\phi(x,t) \cdot \vec{n} = (\vec{w}^k(x) - \vec{b}^k(x)) \cdot \vec{n} & x \in \partial\Omega, t \in [0,T] \end{cases}, \tag{5.25}$$

where

$$h'_\varepsilon(\phi(x)) = \delta_\varepsilon(\phi(x)+l)(1 - H_\varepsilon(\phi(x)-l)) - H_\varepsilon(\phi(x)+l)\delta_\varepsilon(\phi(x)-l). \tag{5.26}$$

$$\delta'_\varepsilon(\phi) = \begin{cases} -\frac{\pi}{2\varepsilon^2}\sin\left(\frac{\pi\phi}{\varepsilon}\right) & |\phi| \le \varepsilon \\ 0 & |\phi| > \varepsilon \end{cases}, \tag{5.27}$$

With the Heaviside function originally adopted in [8], the newly introduced component $\delta'_\varepsilon(\phi)$ in the split-Bregman algorithm may be excessively smoothed. Furthermore, as the SR is an edge-based model and the repelling force is local, smoothing $H(\phi)$ over the entire image causes the repelling force to propagate across the image, resulting in unnecessary instability. With the new choice of Heaviside function, the smoothing effect is restricted only to a narrow band of width 2ε surrounding the contour which in practice can stabilize the evolution of the contour.

For the sub-problem (5.23), if $|\vec{w}(x)| \neq 0$, we can obtain the corresponding Euler-Lagrange equation of $\vec{w}(x)$ as,

$$\left.\begin{array}{l} \gamma g(x)\delta_\varepsilon(\phi^{k+1}(x))\frac{\vec{w}(x)}{|\vec{w}(x)|} - 2\beta h_\varepsilon(\phi^{k+1}(x)) \int_\Omega e^{-\frac{|x-y|^2}{d^2}} \vec{w}(y) h_\varepsilon(\phi^{k+1}(y,t))dy \\ +\mu(\vec{w}(x) - \nabla\phi^{k+1}(x) - \vec{b}^k(x)) = 0 \end{array}\right\}.$$

$$s.t.\ |\vec{w}(x)| = 1 \tag{5.28}$$

However, since the second term in (5.28) contains the integral of $\vec{w}(y)$, it is difficult to construct the iterative scheme for $\vec{w}^k$. An approximation formula with projection is designed in the next section to address this issue.

For the next step in solving (5.24) and (5.28), we devise the discretization of

the continuous derivatives. Let the spatial step be 1 and time step be t, and the discrete coordinates for the pixel (i,j) be $x_{i,j} = (x_{1i}, x_{2j})$ where $i = 0,1,2,...,M+1$, $j = 0,1,2,...,N+1$, we get $\phi_{i,j} = \phi(x_{1i}, x_{2j})$. Let the other variables take similar forms. With the first order finite difference approximation, we can obtain the discrete gradient, Laplacian, and divergences respectively as,

$$\begin{aligned} \nabla\phi_{i,j} &= \begin{bmatrix} \phi_{i+1,j} - \phi_{i,j} \\ \phi_{i,j+1} - \phi_{i,j} \end{bmatrix}, \\ \Delta\phi_{i,j} &= \phi_{i-1,j} + \phi_{i,j-1} + \phi_{i+1,j} + \phi_{i,j+1} - 4\phi_{i,j}. \end{aligned} \tag{5.29}$$

$$\begin{aligned} \nabla\vec{w}_{i,j} &= (\vec{w}_{1i,j} - \vec{w}_{1i-1,j}) + (\vec{w}_{2i,j} - \vec{w}_{2i,j-1}), \\ \nabla\vec{b}_{i,j} &= (\vec{b}_{1i,j} - \vec{b}_{1i-1,j}) + (\vec{b}_{2i,j} - \vec{b}_{2i,j-1}), \end{aligned} \tag{5.30}$$

The first order time derivative of $\phi_{i,j}$ can be approximated as $\frac{\partial\phi_{i,j}}{\partial t} = \frac{\phi_{i,j}^{k+1} - \phi_{i,j}^{k}}{t}$. Therefore, from (5.24), a semi-implicit iterative scheme can be designed for $\phi_{i,j}^{k+1,s+1}$ where $s = 0,1,2,...,S$, such that,

$$\begin{aligned} &\phi_{i,j}^{k+1,0} = \phi_{i,j}^{k}, \\ &\frac{\phi_{i,j}^{k+1,s+1} - \phi_{i,j}^{k+1,s}}{t} = \left\{ \begin{array}{l} -2\gamma g_{i,j}|\vec{w}_{i,j}^{k}|\delta_{\varepsilon}'(\phi_{i,j}^{k+1,s}) + \alpha g_{i,j}\delta_{\varepsilon}(\phi_{i,j}^{k+1,s}) \\ +\mu(\phi_{i-1,j}^{k+1,s+1} + \phi_{i,j-1}^{k+1,s+1} + \phi_{i+1,j}^{k+1,s} + \phi_{i,j+1}^{k+1,s} - 4\phi_{i,j}^{k+1,s+1}) \\ +2\beta h_{\varepsilon}'(\phi_{i,j}^{k+1,s})\vec{w}_{i,j}^{k} \cdot \vec{v}_{i,j}^{k} + \mu(\nabla \cdot \vec{b}_{i,j}^{k} - \nabla \cdot \vec{w}_{i,j}^{k}) \end{array} \right\}, \end{aligned} \tag{5.31}$$

until $\frac{\left\|\phi^{k+1,s+1} - \phi^{k+1,s}\right\|}{\left\|\phi^{k+1,s}\right\| + 10^{-6}} \leq Tol.$

$$\vec{v}_{i,j}^{k,s} = \left(\sum_{p=-d}^{d} \sum_{q=-d}^{d} e^{-\frac{\left(p^2+q^2\right)}{d^2}} \vec{w}_{i+p,j+q}^{k} h_{\varepsilon}\left(\phi_{i+p,j+q}^{k+1,s}\right) \right) \tag{5.32}$$

which is the discrete approximation of $\vec{v}^{k}(x) = \int_{\Omega} e^{-\frac{|x-y|^2}{d^2}} \vec{w}^{k}(y) h_{\varepsilon}(\phi(y,t))dy$. y denotes a point taken from a small window of size $2d \times 2d$ around point x. The repulsion from points further away is negligible, therefore we only check within a small window. Note that the initial and boundary conditions in (5.25) still hold.

Next, we will solve (5.28) iteratively. By temporarily fixing $\vec{w}^{k+1,r}(y)$, we can design a concise approximate generalized soft thresholding formula. For abbreviation, let

$$\vec{v}^{k+1,r}(x) = \int_{\Omega} e^{-\frac{|x-y|^2}{d^2}} \vec{w}^{k+1,r}(y) h_{\varepsilon}\left(\phi^{k+1}(y)\right) dy, \tag{5.33}$$

and $\vec{w}^{k+1,0}(y) = \vec{w}^{k}(y)$. For $r = 0, 1, 2, \ldots, R$, since $|\vec{w}_{i,j}^{k+1,r}| = 1$, the iterative formula for $\vec{w}^{k+1}$ from (5.23) can be written as,

$$\tilde{\vec{w}}_{i,j}^{k+1,r+1} \approx \frac{\mu \nabla \phi_{i,j}^{k+1} + \mu \vec{b}_{i,j}^{k} + 2\beta h_{\varepsilon}\left(\phi_{i,j}^{k+1}\right) \vec{v}_{i,j}^{k+1,r}}{\gamma g_{i,j} \delta_{\varepsilon}(\phi_{i,j}^{k+1}) + \mu}, \tag{5.34}$$

$$\vec{w}_{i,j}^{k+1,r+1} = \frac{\tilde{\vec{w}}_{i,j}^{k+1,r+1}}{\left|\tilde{\vec{w}}_{i,j}^{k+1,r+1}\right|}. \tag{5.35}$$

In practice, a single iteration is often enough to compute 5.34. Alternatively, we can directly use the soft thresholding formula to derive $\vec{w}^{k+1}$. For abbreviation, let

$$\vec{B}^{k+1} = \nabla \phi^{k+1}(x) + \vec{b}^{k} + \frac{2\beta}{\mu} h_{\varepsilon}\left(\phi^{k+1}(x)\right) \int_{\Omega} e^{-\frac{|x-y|^2}{d^2}} \vec{w}^{k+1}(y) h_{\varepsilon}\left(\phi^{k+1}(y)\right) dy. \tag{5.36}$$

The formula for $\vec{w}_{i,j}^{k+1}$ is

$$\vec{w}_{i,j}^{k+1} \approx \max(|\vec{B}_{i,j}^{k+1}| - \frac{\gamma}{\mu} g_{i,j} \delta_{\varepsilon}(\phi_{i,j}^{k+1}), 0) \frac{\vec{B}_{i,j}^{k+1}}{|\vec{B}_{i,j}^{k+1}|}, 0 \frac{\vec{0}}{|\vec{0}|} = \vec{0}. \tag{5.37}$$

The same projection scheme as (5.35) is used afterwards. After $\phi_{i,j}^{k+1}, \vec{w}_{i,j}^{k+1}$ have been obtained, we can derive $\vec{b}_{i,j}^{k+1}$ directly from (5.21).

In summary, the split-Bregman algorithm proposed in this section has four main advantages. 1) The memory requirement is reduced. For an image of size $m \times n$, the parameter A in the AOS solution is size $2 \times (m \times n) \times (m \times n)$. However, in the split-Bregman algorithm, the sizes of both $\vec{w}$ and $\vec{b}$ are $2 \times (m \times n)$ only. As the image size increases, the memory usage in the original algorithm increases quadratically while the one in the new algorithm increases linearly. This is an important point when

dealing with large images. 2) The numerical solution can be simplified. In (5.15), the convolution term containing $\nabla\phi$ is hyperbolic, which requires the upwind difference scheme. By substituting $\nabla\phi$ with the auxiliary variable $\vec{w}$ we can remove the need for complex discretization schemes. 3) The use of a simple projection scheme in place of the initialization step improves algorithm efficiency. 4) Contour evolution is stabilized by confining the smoothing of the Heaviside function to the narrow-bands around the contours.

The proposed algorithm is summarized in Algorithm 4.

Algorithm 4 The split-Bregman algorithm for the self-repelling snakes model

(1) Initialize

Calculate $g(x)$ using (5.1)

Initialize $\phi^0(x)$ as signed distance function and set $\vec{w}^0 = \overrightarrow{0}, \vec{b}^0 = \overrightarrow{0}$

Set penalty parameters

Set tolerance errors, time step and iterative steps

(2) Iterations

For k=0,1,2,...,K

For s=0,1,2,...,S

Calculate $\phi^{k+1,s+1}$ from (5.31)

End for s when (5.22) converges

Calculate $\vec{w}^{k+1}$ from (5.37)

Calculate $\vec{b}^{k+1}$ from (5.21)

End for k when (5.11) converges

5.3 Experimental results

The experiments below demonstrate that the split-Bregman solution of the SR model can successfully prevents contour splitting (which causes over-segmentation) and contour merging (which causes under-segmentation). The qualitative performance is comparable to the original solution of SR. Two practical applications are

shown as well as an extended case in 3D. All experiments are performed on the PC (Intel(R) Core (TM) i7-7700 CPU @ 3.60GHz 3.60 GHz; 16.0 GB memory). The segmentation program is written in Matlab and runs in Matlab environment R2018b.

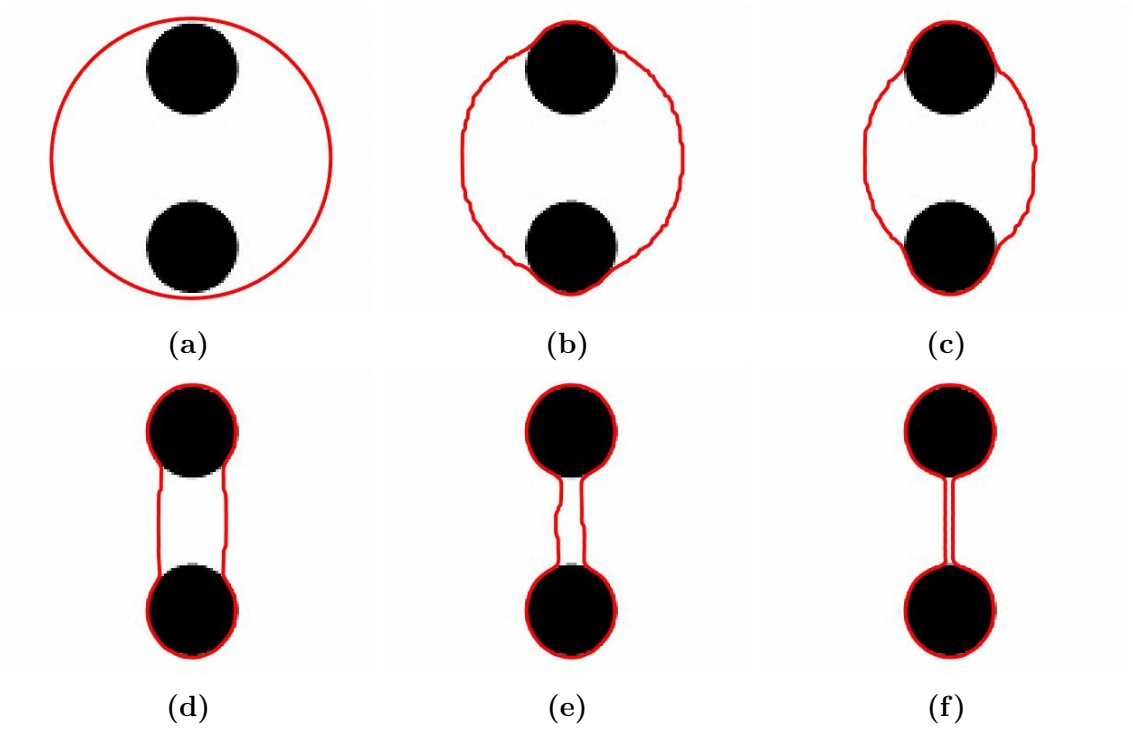

Fig. 5-1: Segmentation of two circles with the split-Bregman algorithm, image taken from [8]. (a) is the initial contour, (b-f) show the evolution of the contour. $\alpha = 4.5$, $\gamma = 5$, $\beta = 0.25$, $\mu = 8$, $l = 1$, $d = 4$, $window = 5 \times 5$, $S = 5$, $\varepsilon = 1$, $t = .05$, $Tol = 10^{-6}$.

In Figure 5-1, contour splitting is successfully prevented and the topology is preserved. The parameter α controls the outwards or inwards driving force, γ dictates the geodesic length, β weighs the repelling force, and μ weighs the constraint. A large β causes the contour to become unstable, as the repulsive force is a highly local term. However, increasing β and decreasing the window size narrows the gap between the contours. Typically, the window size is 5×5 or 7×7 as according to [8]. The time step t is chosen according to the convergence condition $t \leq \frac{1}{4\mu}$ based on the Courant-Friedrichs-Lewy condition [88]. Increasing ε improves the smoothness of the contour but lowers the effectiveness of topology preservation, as it smooths out the repulsive force.

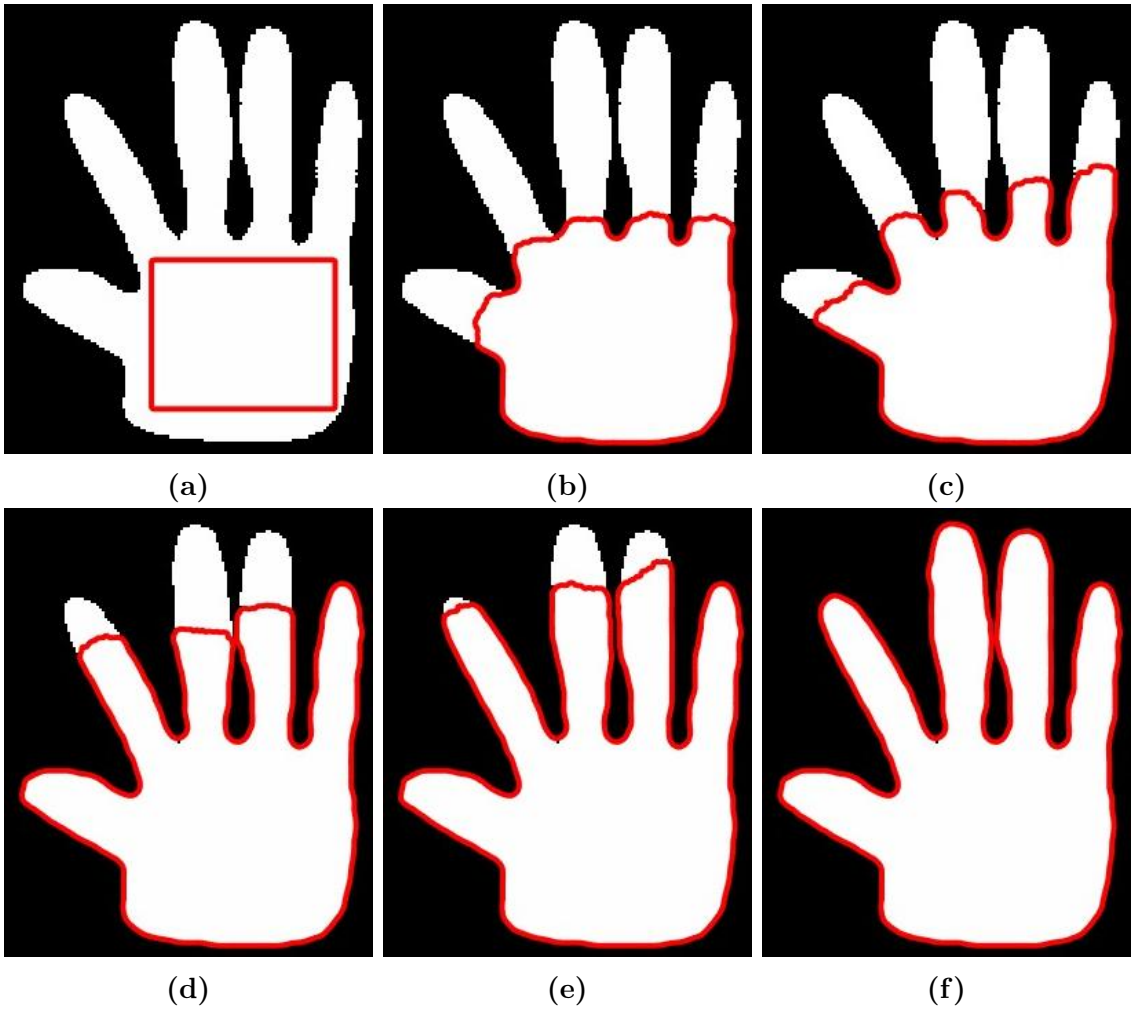

Fig. 5-2: Segmentation of synthetic hand with the split-Bregman algorithm, image taken from [8]. (a) is the initial contour, (b-f) show the evolution of the contour. $\alpha = 5$, $\gamma = 15$, $\beta = 0.5$, $\mu = 5$, $l = 1$, $d = 4$, $window = 7 \times 7$, $S = 5$, $\varepsilon = 1$, $t = .05$, $Tol = 10^{-6}$.

In Figure 5-2, contour merging is prevented as the fingers of the hand remain separate. In the basic GAC model [9], the proximity of the contours would cause them to merge despite there being a detected edge, because it reduces the total geodesic length. The SR model prevents contour merging through the additional repulsion term.

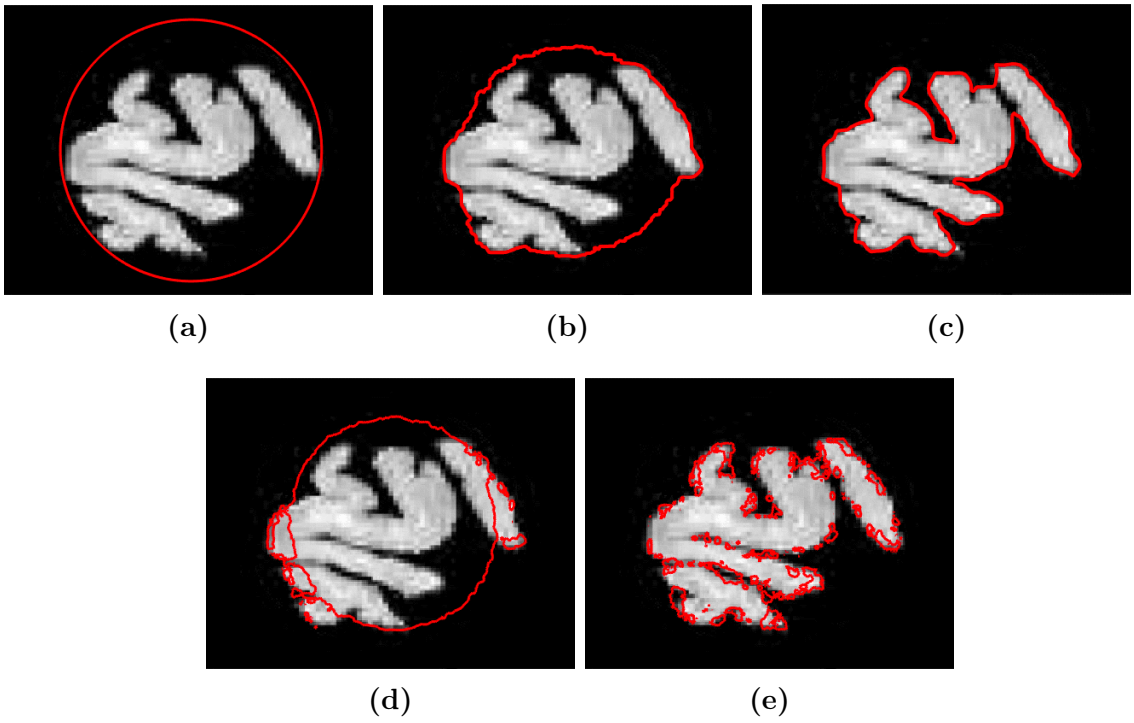

Fig. 5-3: Segmentation of a brain, image taken from [8]. (a) is the original image, (b-c) uses the new Heaviside function with $\alpha = 10$, $\gamma = 15$, $\beta = 2$, $\mu = 5$, $l = 1$, $d = 4$, $window = 7 \times 7$, $S = 5$, $\varepsilon = 1$, $t = .1$, $Tol = 10^{-6}$. (d-e) uses the original Heaviside function with the same parameters.

Figure 5-3 compares the effect of two different Heaviside functions. The advantage of the new Heaviside formulation lies in the stabilization of the repulsion term, which makes the algorithm more robust. In the two experiments in Figure 5-3, the amount of repulsion was set to very high through a large β value. However, it did not disturb the smoothness of the contour, cause the lose of necessary details, or alter the topology in the new algorithm, as shown in Figure 5-3 (b-c). Using the same set of parameters and the original Heaviside function in the old algorithm, the repulsive force of the contour is dissipated across the whole image and the segmentation failed, as shown in Figure 5-3 (d-e) where the topology and smoothness of the contour are no longer maintained. This shows that the new Heaviside function lowers the dependence of the algorithm on the choice of parameters and is therefore better at maintaining the stability of the SR model and increasing robustness.

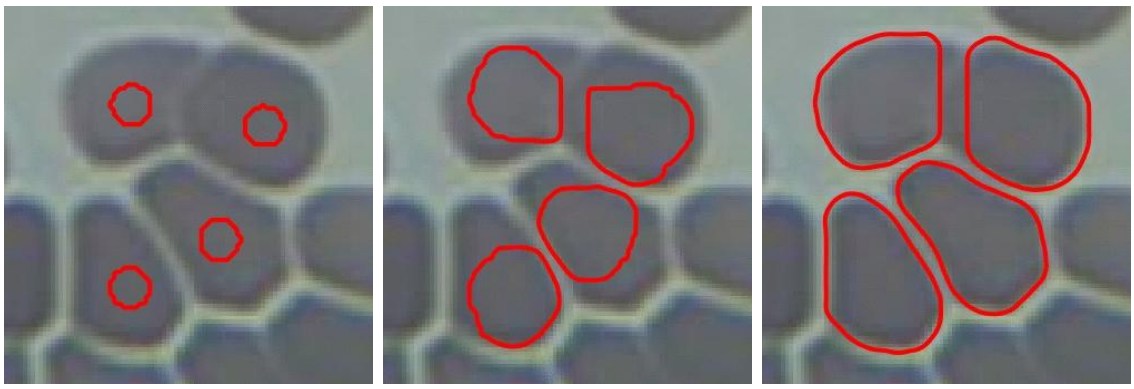

(a) **(b)** **(c)**

Fig. 5-4: Segmentation of cells (image taken from [10]). (a) is the initial contour, (b-c) show the process of contour evolution. $\alpha = 4$, $\gamma = 4$, $\beta = 0.2$, $\mu = 5$, $l = 1$, $d = 4$, $window = 7 \times 7$, $S = 5$ $\varepsilon = 1$, $t = .05$, $Tol = 10^{-6}$.

One example of a practical application of the algorithm is adhesive cell segmentation. The centers of cells can be detected via k-means clustering or detector filters such as the circle Hough Transform or the Laplacian of Gaussian [89]. Since the topology is maintained, the number of cells remains the same. In Figure 5-4, the repulsive force prevents cell contours from merging and separates the adhesive cells.

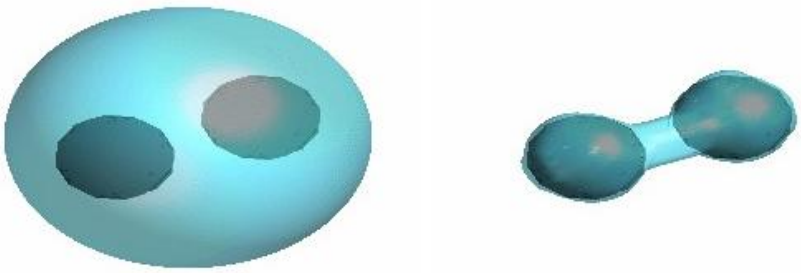

(a) **(b)**

Fig. 5-5: Segmentation of two orbs in 3D. The cyan surface is the zero level set and the black orbs are the objects. (a) is the initial contour, (b) is the final contour. $\alpha = 4$, $\gamma = 5$, $\beta = 0.2$, $\mu = 3$, $l = 1$, $d = 4$, $window = 5 \times 5$, $S = 5$ $\varepsilon = 1$, $t = .05$, $Tol = 10^{-6}$.

The algorithm can also be extended to 3D, where $\phi(x) : \Omega \subset \mathbb{R}^3 \rightarrow \mathbb{R}$. The segmentation contour then becomes a surface whose topology remains the same during segmentation. The segmentation of two orbs is presented in Figure 5-5, where contour

splitting is prevented and the two orbs are segmented as one instance.

5.4 Summary

Preserving the contour topology during image segmentation is useful in many practical scenarios. By keeping the contours isomorphic, it is possible to prevent over-segmentation and under-segmentation, as well as to make the segmentation contour adhere to given topologies. The self-repelling snakes model (SR) is a variational model that preserves contour topology by combining a non-local repulsion term with the geodesic active contour model (GAC). The SR is traditionally solved using the additive operator splitting (AOS) scheme. Although this solution is stable, the memory requirement grows quickly as the image size increases. In this chapter, we proposed an alternative solution to the SR using the split-Bregman method. The proposed algorithm breaks the problem down into simpler subproblems to use lower-order evolution equations and approximation schemes. There are several advantages to the new algorithm. 1) The memory usage is significantly reduced as the size of intermediate variables is one order smaller before. 2) The need for complex discretization schemes is circumvented. 3) The re-initionalization scheme is circumvented and calculations are simplified. 4) The stability of the algorithm is increased through restricting the repulsive force to strictly within the narrow bands around the contour. Experiments show that compared to the original algorithm, the new algorithm is equally effective while being less dependant on the parameters and requiring less memory.

Chapter 6

Conclusions and Future Works

6.1 Conclusions

The image segmentation problem, as the foundation of many high-level image analysis and computer vision tasks, remains actively researched up till this day. There are presently countless image segmentation methods, ranging from simple heuristics-based pipelines to data-driven neural networks with up to millions of internal parameters. Though the task of separating the disjoint regions in an image appears simple to the human, computer algorithms must set up and enforce many segmentation criteria based on both the image and prior knowledge. Variational models are a branch of mathematical models that dynamically solve problems through the minimization of an energy functional. Since the late 1980s, they have gained much momentum in areas of image analysis such as inpainting, denoising, segmentation, etc. With regards to image segmentation, in particular, the active contour variational models have been applied to mass-market commercial applications as well as in specialized solutions for domain problems, especially in medicine.

The variational models have three main advantages. One, they are reliable and interpretable. Each term inside the energy functional serves a specific, defined purpose. Once the model has been designed term by term, we can prove its theoretical solvability with mathematics and devise efficient numerical algorithms with modern optimization methods. Two, they are highly customizable. Given the specific sce-

nario, we can construct an energy functional that builds on terms that represent the specific segmentation criteria to suit our purpose. Three, they are light-weight and portable. There are no complex functions with many hyperparameters to store, yet the models still fulfil their functions well.

The main directions of research in the variational image segmentation area are designs of new model components, efficient numerical solutions, and variational models catering to real-world applications. In this thesis, we focused on designing and implementing models with prior constraints.

In Chapter 3, we proposed the Chan-Vese model with landmark constraints (CVL) model by combining a novel landmark constraint term with the Chan-Vese model, a two-phase image segmentation model based on the piecewise constant assumption. We proposed a numerical solution to the CVL using the split-Bregman method and proved the theoretical convergence of the new model. As demonstrated in the experiments on synthetic and real images, the CVL model improved both the overall segmentation accuracy and the accuracy within critical regions. The guidance from the landmarks successfully negated the effect of bad contour initialization by pushing the level set function out of the local energy minima. The same correction effect can be observed in noisy images when the contour is flawed. Critical regions also became better defined when guided by landmarks. With the CVL model, image segmentation based on homogeneous regions where the contour passes some pre-defined landmarks can be realized.

However, it is observed that landmarks too far from the object boundary could not be connected via the CVL. A new segmentation problem was defined in this case, where the task is interpolating or inpainting the segmentation contour between landmarks during segmentation. In Chapter 4, we proposed to incorporate the Euler's elatica into the CVL. The new model, the Chan-Vese model with landmark constraints and elastica (CVLE), specializes in the inpainting of long illusory contours. We proposed the numerical solution to the new model via the split-Bregman method a projection method, using more intermediate variables than previously to circumvent the calculation of curvature. Experimental comparison between the CV, CVE, CVL,

and CVLE show the advantage of the CVLE in producing smoother contour interpolations and preserving more details in the segmentation result. The CVLE model can address problems such as the segmentation of occluded and damaged objects with the guidance of landmarks.

In Chapter 5, we designed a more stable, concise, and memory-efficient solution for the self-repelling snakes (SR) model. The SR model initially uses the additive operator splitting scheme, which induces a memory requirement to the order of the square of the image size. The split-Bregman algorithm we proposed cuts down the memory size by one order, as well as simplifies calculations with the projection scheme. We also adopted a differently smoothed Heaviside function which increased the stability of contour evolution by restricting the effect of contour repulsion to be within narrow bands around the contour. Experiments compared the new algorithm to the original one as well as demonstrated some real-world applications in MRI image segmentation and cell segmentation. The algorithm has also been extended to segment 3D objects.

In summary, the works in this thesis addressed problems with regards to image segmentation with constraints under the variational level set paradigm. The purpose of enforcing constraints is to assist the segmentation process with more information. The landmark constraints allow the contour to connect to pre-defined landmarks. The term is useful in guiding the contour in the right direction and refining critical regions to increase the segmentation accuracy. The landmark constraints combined with the Euler's elastica enables the contour to connect to more distant landmarks to create long illusory contours. This is useful for reconstructing the contours of objects whose boundaries are lost in the image due to occlusion or damages. The topology preservation constraint prevents the segmentation contour from splitting or merging. It is effective in stopping under-segmentation and over-segmentation, as well as segmenting objects whose topologies are known in advance. Reducing the amount of calculations and the memory requirement of the algorithms makes them more applicable to practical scenarios, while lowering the dependence of the results on the parameters and initial conditions increases the robustness of the variational models.

6.2 Future works

The focus of this thesis is on designing new constraints for variational models and devising efficient numerical algorithms for their solution, as well as providing some basic theoretical discussions. The landmark constraints and landmark constraints combined with Euler's elastica have only been incorporated into the classical Chan-Vese model. Since the terms in a variational model are relatively customizable, it is also possible to include these new constraints in other region-based models, edge-based models, and models based on other image features. For example, the new constraints can be applied to multi-phase [36], texture [37, 54], noise [55], and motion [56] segmentation problems, even the 3D reconstruction of surfaces. Many existing variational image segmentation models can benefit from the guidance of landmarks.

On the other hand, the subjects of efficiency, stability, and accuracy have always been of vital importance to variational models. Compared to other popular approaches, PDE-based algorithms tend to suffer from elaborate calculations that reduce their practicality from an engineering perspective. This disadvantage can be countered by better algorithm design, parallelization, or priming the algorithms for the GPU or other powerful hardware. With further efforts made in this regard, the variational models proposed in this thesis can be utilized in many practical segmentation problems, particularly those where landmarks are easily obtainable or readily available.

A recent trend occasioned by the age of Big Data is the increasing importance of the role of data in image processing. Much information can be gleaned from the vast datasets online that may prove useful in segmentation problems. Landmarks and topologies are both prior constraints. In the experiments conducted in this thesis, they have been dictated by human. However, they can also be extracted automatically by a machine learning-based algorithm. While variational models afford much control to the human over the segmentation process, learning from prior information can help increase the level of automation and robustness of the algorithms. Obtaining landmarks and topological information automatically through neural networks and

feeding them into the proposed variational algorithms may be a viable approach.

Bibliography

[1] J. Canny, A computational approach to edge detection, IEEE Transactions on pattern analysis and machine intelligence (6) (1986) 679–698.

[2] N. Otsu, A threshold selection method from gray-level histograms, IEEE transactions on systems, man, and cybernetics 9 (1) (1979) 62–66.

[3] L. Vincent, P. Soille, Watersheds in digital spaces: an efficient algorithm based on immersion simulations, IEEE Transactions on Pattern Analysis & Machine Intelligence (6) (1991) 583–598.

[4] G. Cao, Z. Mao, X. Yang, D. Xia, Optical aerial image partitioning using level sets based on modified chan–vese model, Pattern Recognition Letters 29 (4) (2008) 457–464.

[5] C. Xu, J. L. Prince, Gradient vector flow deformable models, Handbook of Medical Imaging (2000) 159–169.

[6] T. Brox, M. Rousson, R. Deriche, J. Weickert, Colour, texture, and motion in level set based segmentation and tracking, Image and Vision Computing 28 (3) (2010) 376–390.

[7] T. Chan, W. Zhu, Level set based shape prior segmentation, in: 2005 IEEE Computer Society Conference on Computer Vision and Pattern Recognition (CVPR'05), Vol. 2, IEEE, 2005, pp. 1164–1170.

[8] C. Le Guyader, L. A. Vese, Self-repelling snakes for topology-preserving segmentation models, IEEE Transactions on Image Processing 17 (5) (2008) 767–779.

[9] V. Caselles, R. Kimmel, G. Sapiro, Geodesic active contours, International journal of computer vision 22 (1) (1997) 61–79.

[10] J. Duan, Variational and PDE-based methods for image processing, Ph.D. thesis, University of Nottingham (2018).

[11] R. Adams, L. Bischof, Seeded region growing, IEEE Transactions on pattern analysis and machine intelligence 16 (6) (1994) 641–647.

[12] Y. LeCun, Y. Bengio, G. Hinton, Deep learning, nature 521 (7553) (2015) 436–444.

[13] M. Kass, A. Witkin, D. Terzopoulos, Snakes: Active contour models, International journal of computer vision 1 (4) (1988) 321–331.

[14] T. F. Chan, L. A. Vese, Active contours without edges, IEEE Transactions on image processing 10 (2) (2001) 266–277.

[15] J. Shi, J. Malik, Normalized cuts and image segmentation, Departmental Papers (CIS) (2000) 107.

[16] S. Geman, D. Geman, Stochastic relaxation, gibbs distributions, and the bayesian restoration of images, IEEE Transactions on pattern analysis and machine intelligence (6) (1984) 721–741.

[17] L.-C. Chen, Y. Zhu, G. Papandreou, F. Schroff, H. Adam, Encoder-decoder with atrous separable convolution for semantic image segmentation, in: Proceedings of the European conference on computer vision (ECCV), 2018, pp. 801–818.

[18] G. Aubert, P. Kornprobst, Mathematical problems in image processing: partial differential equations and the calculus of variations (Second Edition), Vol. 147, Springer Science & Business Media, 2006.

[19] D. P. Kingma, M. Welling, Auto-encoding variational bayes, arXiv preprint arXiv:1312.6114.

[20] G. Wang, Z. Pan, Z. Zhang, Deep CNN denoiser prior for multiplicative noise removal, Multimedia Tools and Applications 78 (20) (2019) 29007–29019.

[21] J. Duan, J. Schlemper, W. Bai, T. J. Dawes, G. Bello, G. Doumou, A. De Marvao, D. P. O'Regan, D. Rueckert, Deep nested level sets: Fully automated segmentation of cardiac mr images in patients with pulmonary hypertension, in: International Conference on Medical Image Computing and Computer-Assisted Intervention, Springer, 2018, pp. 595–603.

[22] G. Sapiro, Geometric partial differential equations and image analysis, Cambridge university press, 2001.

[23] T. F. Chan, J. J. Shen, Image processing and analysis: variational, PDE, wavelet, and stochastic methods, Vol. 94, Siam, 2005.

[24] J. J. Koenderink, The structure of images, Biological cybernetics 50 (5) (1984) 363–370.

[25] A. Witkin, Scale-space filtering: A new approach to multi-scale description, in: ICASSP'84. IEEE International Conference on Acoustics, Speech, and Signal Processing, Vol. 9, IEEE, 1984, pp. 150–153.

[26] P. Perona, J. Malik, Scale-space and edge detection using anisotropic diffusion, IEEE Transactions on pattern analysis and machine intelligence 12 (7) (1990) 629–639.

[27] D. Mumford, J. Shah, Optimal approximations by piecewise smooth functions and associated variational problems, Communications on pure and applied mathematics 42 (5) (1989) 577–685.

[28] L. D. Cohen, On active contour models and balloons, CVGIP: Image understanding 53 (2) (1991) 211–218.

[29] C. Xu, J. L. Prince, Snakes, shapes, and gradient vector flow, IEEE Transactions on image processing 7 (3) (1998) 359–369.

[30] C. Xu, J. L. Prince, Generalized gradient vector flow external forces for active contours, Signal processing 71 (2) (1998) 131–139.

[31] V. Caselles, F. Catté, T. Coll, F. Dibos, A geometric model for active contours in image processing, Numerische mathematik 66 (1) (1993) 1–31.

[32] R. Malladi, J. A. Sethian, B. C. Vemuri, Shape modeling with front propagation: A level set approach, IEEE transactions on pattern analysis and machine intelligence 17 (2) (1995) 158–175.

[33] S. Osher, J. A. Sethian, Fronts propagating with curvature-dependent speed: algorithms based on hamilton-jacobi formulations, Journal of computational physics 79 (1) (1988) 12–49.

[34] L. Ambrosio, V. M. Tortorelli, Approximation of functional depending on jumps by elliptic functional via t-convergence, Communications on Pure and Applied Mathematics 43 (8) (1990) 999–1036.

[35] X. Bresson, S. Esedoḡlu, P. Vandergheynst, J.-P. Thiran, S. Osher, Fast global minimization of the active contour/snake model, Journal of Mathematical Imaging and vision 28 (2) (2007) 151–167.

[36] L. A. Vese, T. F. Chan, A multiphase level set framework for image segmentation using the mumford and shah model, International journal of computer vision 50 (3) (2002) 271–293.

[37] B. Sandberg, T. Chan, L. Vese, A level-set and gabor-based active contour algorithm for segmenting textured images, in: UCLA Department of Mathematics CAM report, Citeseer, 2002.

[38] T. Amiaz, N. Kiryati, Piecewise-smooth dense optical flow via level sets, International Journal of Computer Vision 68 (2) (2006) 111–124.

[39] A. Sarti, C. Corsi, E. Mazzini, C. Lamberti, Maximum likelihood segmentation of ultrasound images with rayleigh distribution, IEEE transactions on ultrasonics, ferroelectrics, and frequency control 52 (6) (2005) 947–960.

[40] Y. Chen, H. D. Tagare, S. Thiruvenkadam, F. Huang, D. Wilson, K. S. Gopinath, R. W. Briggs, E. A. Geiser, Using prior shapes in geometric active contours in a variational framework, International Journal of Computer Vision 50 (3) (2002) 315–328.

[41] M. Rousson, N. Paragios, Shape priors for level set representations, in: European Conference on Computer Vision, Springer, 2002, pp. 78–92.

[42] R. Kimmel, Fast edge integration, in: Geometric Level Set Methods in Imaging, Vision, and Graphics, Springer, 2003, pp. 59–77.

[43] T. Goldstein, S. Osher, The split Bregman method for l1-regularized problems, SIAM journal on imaging sciences 2 (2) (2009) 323–343.

[44] C. Wu, X.-C. Tai, Augmented Lagrangian method, dual methods, and split Bregman iteration for ROF, vectorial TV, and high order models, SIAM Journal on Imaging Sciences 3 (3) (2010) 300–339.

[45] T. Goldstein, B. O'Donoghue, S. Setzer, R. Baraniuk, Fast alternating direction optimization methods, SIAM Journal on Imaging Sciences 7 (3) (2014) 1588–1623.

[46] R. Valle, J. M. Buenaposada, A. Valdes, L. Baumela, A deeply-initialized coarse-to-fine ensemble of regression trees for face alignment, in: Proceedings of the European Conference on Computer Vision (ECCV), 2018, pp. 585–601.

[47] D. G. Lowe, Object recognition from local scale-invariant features, in: Proceedings of the seventh IEEE international conference on computer vision, Vol. 2, 1999, pp. 1150–1157.

[48] R. Funayama, H. Yanagihara, L. Van Gool, T. Tuytelaars, H. Bay, Robust interest point detector and descriptor, uS Patent 8,165,401 (Apr. 24 2012).

[49] J. Duan, G. Bello, J. Schlemper, W. Bai, T. J. Dawes, C. Biffi, A. de Marvao, G. Doumoud, D. P. O'Regan, D. Rueckert, Automatic 3D bi-ventricular segmentation of cardiac images by a shape-refined multi-task deep learning approach, IEEE transactions on medical imaging 38 (9) (2019) 2151–2164.

[50] L. I. Rudin, S. Osher, E. Fatemi, Nonlinear total variation based noise removal algorithms, Physica D: nonlinear phenomena 60 (1-4) (1992) 259–268.

[51] H. Pan, W. Liu, L. Li, G. Zhou, A novel level set approach for image segmentation with landmark constraints, Optik 182 (2019) 257–268.

[52] H.-K. Zhao, T. Chan, B. Merriman, S. Osher, A variational level set approach to multiphase motion, Journal of computational physics 127 (1) (1996) 179–195.

[53] T. F. Chan, B. Y. Sandberg, L. A. Vese, Active contours without edges for vector-valued images, Journal of Visual Communication and Image Representation 11 (2) (2000) 130–141.

[54] C. Sagiv, N. A. Sochen, Y. Y. Zeevi, Integrated active contours for texture segmentation, IEEE transactions on image processing 15 (6) (2006) 1633–1646.

[55] C. Samson, L. Blanc-Féraud, G. Aubert, J. Zerubia, A variational model for image classification and restoration, IEEE Transactions on Pattern Analysis and Machine Intelligence 22 (5) (2000) 460–472.

[56] D. Cremers, S. Soatto, Motion competition: A variational approach to piecewise parametric motion segmentation, International Journal of Computer Vision 62 (3) (2005) 249–265.

[57] C. Li, C. Xu, C. Gui, M. D. Fox, Level set evolution without re-initialization: a new variational formulation, in: Computer Vision and Pattern Recognition, 2005. CVPR 2005. IEEE Computer Society Conference on, Vol. 1, IEEE, 2005, pp. 430–436.

[58] J. Duan, Z. Pan, X. Yin, W. Wei, G. Wang, Some fast projection methods based on chan-vese model for image segmentation, EURASIP Journal on Image and Video Processing 2014 (1) (2014) 7.

[59] A. Chambolle, An algorithm for total variation minimization and applications, Journal of Mathematical imaging and vision 20 (1-2) (2004) 89–97.

[60] K. Rohr, Landmark-based image analysis: using geometric and intensity models, Vol. 21, Springer, 2001.

[61] J. Modersitzki, Numerical methods for image registration, Oxford University Press, 2004.

[62] W.-H. Liao, A. Khuu, M. Bergsneider, L. Vese, S.-C. Huang, S. Osher, From landmark matching to shape and open curve matching: a level set approach, UCLA CAM Report 2 (59).

[63] K. C. Lam, L. M. Lui, Landmark-and intensity-based registration with large deformations via quasi-conformal maps, SIAM Journal on Imaging Sciences 7 (4) (2014) 2364–2392.

[64] F. Brunet, V. Gay-Bellile, A. Bartoli, N. Navab, R. Malgouyres, Feature-driven direct non-rigid image registration, International journal of computer vision 93 (1) (2011) 33–52.

[65] H. Huang, X. Zuo, C. Huang, Arbitrary initialization for chan–vese model, Optik-International Journal for Light and Electron Optics 125 (18) (2014) 5257–5263.

[66] J. Nocedal, S. J. Wright, Nonlinear Equations, Springer, 2006.

[67] J. Song, H. Pan, W. Liu, Z. Pan, The chan-vese model with elastica and landmark constraints for image segmentation, arXiv preprint arXiv:1905.11192.

[68] D. Mumford, Elastica and computer vision, in: Algebraic geometry and its applications, Springer, 1994, pp. 491–506.

[69] J. Shen, S. H. Kang, T. F. Chan, Euler's elastica and curvature-based inpainting, SIAM journal on Applied Mathematics 63 (2) (2003) 564–592.

[70] W. Zhu, T. Chan, Image denoising using mean curvature of image surface, SIAM Journal on Imaging Sciences 5 (1) (2012) 1–32.

[71] W. Zhu, X.-C. Tai, T. Chan, Augmented lagrangian method for a mean curvature based image denoising model, Inverse Probl. Imaging 7 (4) (2013) 1409–1432.

[72] W. Zhu, X.-C. Tai, T. Chan, Image segmentation using euler's elastica as the regularization, Journal of scientific computing 57 (2) (2013) 414–438.

[73] W. Zhu, T. Chan, S. Esedo g^{-} lu, Segmentation with depth: A level set approach, SIAM journal on scientific computing 28 (5) (2006) 1957–1973.

[74] L. Tan, Z. Pan, W. Liu, J. Duan, W. Wei, G. Wang, Image segmentation with depth information via simplified variational level set formulation, Journal of Mathematical Imaging and Vision 60 (1) (2018) 1–17.

[75] L. Euler, Methodus inveniendi lineas curvas maximi minimive proprietate gaudentes, apud Marcum-Michaelem Bousquet, 1744.

[76] M. Nitzberg, D. Mumford, T. Shiota, Filtering, segmentation and depth, Vol. 662, Springer, 1993.

[77] W. Zhu, T. Chan, Capture illusory contours: A level set based approach, UCLA CAM Report (2003) 03–65.

[78] J. Duan, W. O. Ward, L. Sibbett, Z. Pan, L. Bai, Introducing diffusion tensor to high order variational model for image reconstruction, Digital Signal Processing 69 (2017) 323–336.

[79] X. Han, C. Xu, J. L. Prince, A topology preserving level set method for geometric deformable models, IEEE Transactions on Pattern Analysis and Machine Intelligence 25 (6) (2003) 755–768.

[80] T. C. Cecil, Numerical methods for partial differential equations involving discontinuities, Ph.D. thesis, University of California, Los Angeles (2003).

[81] O. Alexandrov, F. Santosa, A topology-preserving level set method for shape optimization, Journal of Computational Physics 204 (1) (2005) 121–130.

[82] G. Sundaramoorthi, A. Yezzi, Global regularizing flows with topology preservation for active contours and polygons, IEEE Transactions on Image Processing 16 (3) (2007) 803–812.

[83] M. Rochery, I. H. Jermyn, J. Zerubia, Higher order active contours, International Journal of Computer Vision 69 (1) (2006) 27–42.

[84] N. Forcadel, C. Le Guyader, A short time existence/uniqueness result for a non-local topology-preserving segmentation model, Journal of Differential Equations 253 (3) (2012) 977–995.

[85] N. Debroux, S. Ozeré, C. Le Guyader, A non-local topology-preserving segmentation-guided registration model, Journal of Mathematical Imaging and Vision 59 (3) (2017) 432–455.

[86] J. A. Geiping, Comparison of topology-preserving segmentation methods and application to mitotic cell tracking, B.S. thesis, Dept. Math. Comput. Sci., Westfälische Wilhelms-Universität at Münster, Münster, Germany (2014).

[87] J. Weickert, B. T. H. Romeny, M. A. Viergever, Efficient and reliable schemes for nonlinear diffusion filtering, IEEE transactions on image processing 7 (3) (1998) 398–410.

[88] S. Osher, R. Fedkiw, Level set methods and dynamic implicit surfaces, Vol. 153, Springer Science & Business Media, 2003.

[89] H. Kong, H. C. Akakin, S. E. Sarma, A generalized Laplacian of Gaussian filter for blob detection and its applications, IEEE transactions on cybernetics 43 (6) (2013) 1719–1733.